Contribution of α3(IV)α4(IV)α5(IV) Collagen IV to the Mechanical Properties of the Glomerular Basement Membrane

A DISSERTATION
SUBMITTED TO THE FACULTY OF
UNIVERSITY OF MINNESOTA
BY

Lazarina Gyoneva

IN PARTIAL FULFILLMENT OF THE REQUIREMENTS
FOR THE DEGREE OF
DOCTOR OF PHILOSOPHY

Victor H. Barocas, Advisor

May 2016

Acknowledgements

All of my friends, family, and colleagues have provided me with invaluable moral support, technical advice, and motivation needed for the completion of this project so there are many people I want to thank for their help throughout the past six years.

Starting with my advisor, Victor Barocas, who is an exceptionally smart and thoughtful person, and who I know always had my best interests in mind. It was a great pleasure to work with him and I am saddened by the prospect of leaving his lab; I feel very lucky to have had such a rewarding experience as a graduate student. In addition to Victor, I also need to thank my other unofficial advisers, Yoav Segal and Kevin D. Dorfman, who took time out of their busy schedules almost every week to meet with us, provide valuable advice, and ask important questions, and who have been so important for the successful completion of my projects. And another committee member, Patrick Alford, who I really enjoyed having as a teacher and who showed great patience over all the homework questions I had. And of course, our Department Chair, Bob Tranquillo, to whom I am very grateful for giving me the opportunity to teach the programming class.

I had the great luck to work with three wonderful and very smart undergraduate students: Daniel (Danny) Goodman, Ryan Pewowaruk, and Samuel Rothstein. Danny has been working with me for 3 years in which time has proven himself as a patient, careful, and dedicated experimenter and programmer. And Ryan and Sam were also very productive and smart students that were very easy to work with. I'm sure that all of them have a great future ahead and I wish them all the best.

The other students in the department have been incredibly nice and welcoming people, and I am happy to count them as friends. There is Sarah Hunt, who I worked with on the kidney project, and roomed with for many years. I am glad that she convinced me to do "crazy" things like taking skiing lessons, and going camping in North Dakota. There are many other senior students in the lab who welcomed me into the group: Tina Nagel, Colleen Witzenburg, Sarah Jouzdani, Faisal Hadi, Victor Lai, and Spencer Lake. And besides Sarah and me, Amy Claeson joined the lab at the same time, who always had the best presentations which were a pleasure to watch. And in turn, I was then happy to meet other great incoming students and post-docs who have already done so much and have helped me as well: Hallie Wagner, Julia Quindlen, Vahhab Zarei, Rohit Dhume, Chris Korenczuk, Sarah Vanderheiden, David Nederlow and the newest babies: Ryan, Shannon, and Emily. I would also like to thank other people at the University who were always fun to spend time with: Shailabh Kumar, Anh La, Ghaidan Shamsan, Steven Lee, and Raghu Venkataraman.

My parents, Ivan and Elisaveta, have supported me for most of my life, always believed in my abilities, and encouraged me to pursue a path of education. When I was in college, I used to go home every weekend and bring back a big box of home cooked food, which always makes studying easier. I know that they are very excited about my graduation and I hope that I can keep making them proud. My sister, Stefka, has really been my inspiration. Since I can remember, she has been an exceptional student, scholar, and researcher, and I always try to keep up with her. And finally, my two best friends

Aileen and Alice, who I can always count on. We all live in different places now but I am very happy that we will always remain friends.

Abstract

The glomerular basement membrane (GBM) is a vital part of the blood-urine filtration barrier in the kidneys. In healthy GBMs, the main tension-resisting component is α3(IV)α4(IV)α5(IV) type IV collagen, but in some diseases it is replaced by other collagen IV isoforms. As a result, the GBM becomes leaky and disorganized, ultimately resulting in kidney failure. Our goal is to understanding the biomechanical aspects of the α3(IV)α4(IV)α5(IV) chains and how their absence could be responsible for (1) the initial injury to the GBM and (2) progression to kidney failure. A combination of experiments and computational models were designed for that purpose. A model basement membrane was used to compare experimentally the distensibility of tissues with the α3(IV)α4(IV)α5(IV) chains present and missing. The experiments showed basement membranes containing α3(IV)α4(IV)α5(IV) chains were less distensible. It has been postulated that the higher level of lateral cross-linking (supercoiling) in the α3(IV)α4(IV)α5(IV) networks contributes additional strength/stability to basement membranes. In a computational model of supercoiled networks, we found that supercoiling greatly increased the stiffness of collagen IV networks but only minimally decreased the permeability, which is well suited for the needs of the GBM. It is also known that the α3(IV)α4(IV)α5(IV) networks are more protected from enzymatic degradation, and we explored their significance in GBM remodeling. Our simulations showed that the more protected network was needed to prevent the system from entering a dangerous feedback cycle due to autoregulation mechanisms in the kidneys. Overall, the work adds to the evidence of biomechanical differences between the

α3(IV)α4(IV)α5(IV) networks and other collagen IV networks, points to supercoiling as the main source of biomechanical differences, discusses the suitability of α3(IV)α4(IV)α5(IV) networks to meet the mechanics and permeability needs of the GBM, and explores the role of biomechanics and enzymatic digestion in GBM remodeling.

Table of Contents

List of Tables

List of Figures

Figure 2.2: Relationship between equatorial diameter and lens thickness. Equatorial diameter was larger than lens thickness in both Alport (□) and wild-type (WT) (●) lenses. The distributions of dimensions for Alport lenses were visibly wider than those for wild-type lenses.

Figure 2.3. Linear strains. (a) Equatorial strain. Defined as in Equation 2.1a and calculated at seven different time points. The wild-type (WT) (●) and Alport (□) curves trended toward significance ($p<0.1$). **(b)** Thickness strain (Equation 2.1b). Alport strain was significantly larger than wild-type (WT) strain at the two- and three-hour time points (indicated with an asterisk, $p<0.05$). **(c)** Surface area strain (Equation 2.1c). There was no statistically significant difference between the wild-type (WT) and Alport strain curves ($p>0.05$).

Figure 2.4: Lens anisotropy over time. Anisotropy was defined as the ratio of equatorial/lens thickness strain (SR). SR was calculated at different time points to investigate the relationship between the directional strains. There was no statistically significant difference between the wild-type (WT) (●) and Alport (□) curves ($p>0.05$).

Figure 3.1. Structure and function of the kidneys at different scales. **(a)** The outer section of the kidneys contains millions of filtration centers. **(b)** In the filtration centers, called glomeruli, pre-filtered blood enters through the afferent arteriole, travels through the glomerular capillaries where water and small solutes can escape to the urinary space,

and the filtered blood continues to the efferent arteriole. The walls of the glomerular capillaries are composed of the glomerular basement membrane (GBM). **(c)** Schematic of collagen IV networks in the GBM with the $[\alpha1(IV)]_2\alpha2(IV)$ (blue) and $\alpha3(IV)\alpha4(IV)\alpha5(IV)$ (red) networks occupying separate sides. Drawings of kidney and glomeruli were reproduced from Gray's anatomy public domain graphic plates.

Figure 3.2. Schematic of original networks and how supercoils were formed. (a) Voronoi networks (in black) were used to represent native collagen IV networks. Each Voronoi edge is a segment of a collagen IV protomer (in red). The protomers in the original network are laterally connected and already have some supercoils (arrow). **(b)** New supercoils are created along the midline of the two segments at each node n_i with the smallest angle α_s; the length of the supercoil was varied as a percent (p_m) of the length of the midline (M). At the end of the supercoil, the combined segments branch off and return to their original nodes. The value of p_m was varied to generate different levels of supercoiling. In this example, p_m = 50% of the midline length.

Figure 3.3. Example of a generated collagen IV network. **(a)** Before deformation, the network has dimensions of 560x560x175 nm. **(b)** The same network at the final step of deformation, 36% stretch. Networks were stretched equibiaxially and treated as incompressible.

Figure 3.4. **Distribution of collagen IV segment lengths. (a)** In the Voronoi collagen IV network model, very short segments were common and there was also a small number of very long segments. **(b)** In a reconstituted collagen IV network, average segment length was 44 nm and there was only a small number of very short segments and no long segments.

Figure 3.5. An example network at different levels of super-coiling. From top to bottom: original network, p_m = 10%, p_m = 30%, and p_m = 50%, where p_m is the percent of the midline length that was super-coiled (see Fig 2). Networks were projected into two dimensions for easier visualization.

Figure 3.6. Effect of supercoiling on stress-stretch response of collagen IV networks. (a) Average stress-stretch response with 95% confidence interval of the original collagen IV networks (N=10), before new supercoils are introduced. **(b)** and **(c)** Difference in stress of supercoiled networks from original networks when the spring constant of supercoils is **(b)** E_{sc} = 0.5 GPa and **(c)** when E_{sc} = 1.0 GPa. Arrow indicates increasing value for the supercoil ratio p_m so the five curves go from p_m = 10% to p_m = 50%.

Figure 3.7. Percent increase of final stress and tangent modulus. **(a)** The increase in stress due to supercoiling for each stretched network at 36% stretch. Two cases are shown: when E_{sc} = 0.5 GPa (circles) and when E_{sc} = 1 GPa (triangles). **(b)** and **(c)** The increase in network tangent modulus due to supercoiling at **(b)** small deformation and **(c)**

large deformation. The tangent modulus of the original network was 4.9 MPa at small deformation and 39.0 MPa at large deformation.

Figure 3.8. Darcy permeability and total permeability of model collagen IV networks. **(a)** As the network is stretched, there is a slight, supercoiling independent drop in permeability due to densification. **(b)** Total permeability is defined as permeability in which the changing cross-sectional area and thickness of the stretched network are accounted for. **(c)** Effect of supercoiling on the total permeability when a network is stretched at a given stress. Arrow indicates increasing value for the supercoil ratio p_m so the five solid black curves go from p_m = 10% to p_m = 50%. The red dashed line is the permeability of the original network, before supercoiling.

Figure 4.1. Model of Cell and Network System. In this parallel configuration, the cell and network experience the same strain, ε_{Tot}, and the total stress of the system, σ_{Tot}, is the sum of the cell and network stresses.

Figure 4.2. Schematic of Remodeling Model. (a) A network is generated as described in Section 4.2.1. **(b)** Before remodeling starts, the system of cell + collagen network is deformed to some strain ε and its concomitant stress σ. **(c)** The final stress in the system ($\sigma_{applied}$) is maintained during remodeling **(d)**, which causes the strain to change by either increasing or decreasing over time depending on the net rate of collagen deposition and

removal. In this example, the net amount of collagen in the network increases, causing the system to contract to maintain the same level of applied stress.

Figure 4.3. Cellular Contribution to the System Stress. (a) Once the remodeling system reached equilibrium at different applied stresses (stress A and stress B in the schematic below), the equilibrium cellular contribution to the system stress (C_A and C_B) were determined. **(b)** An aggregate plot was produced of the equilibrium cell stress vs. applied stress, with each part representing one of the plots from panel (a). A cell in perfect tensional homeostasis would see the cellular stress plateau – the equilibrium cell stress becomes independent from the applied system stress.

Figure 4.4. Choosing values for parameter *α*. The values selected for alpha ensured that the collagen network had overall higher rates of addition than removal and that the network was able to reach equilibrium. **(a)** For a low value of $\alpha = 0.8$, the amount of collagen in the network decreases, especially at low stretches. **(b)** For a high value of $\alpha = 1.0$, the network is not able to equilibrate because the rate of addition is substantially larger than the rate of removal.

Figure 4.5. Typical Remodeling Results. The results are for Case 1 (constant addition, $k_4 = \kappa = 0$), at 20% initial strain, $\alpha = 0.9$, and a cell with stiffness equal to the network stiffness, but are representative of other cases and parameters. **(a)** The system was perturbed to a new stress (171 kPa), and the collagen network remodeled at constant

system stress until both the cell and network reached equilibrium. **(b)** The rate of collagen addition was larger than the rate of collagen removal, causing the collagen volume fraction to increase as remodeling proceeded. **(c)** As more collagen was added, the system had to contract from the initial strain of 20% to maintain the total system stress constant. **(d)** The effect of remodeling on the network can be easily seen by plotting the collagen fibers to scale. Before remodeling, each fiber had radius of 50 nm and the volume fraction of the matrix was 1.2%. At the end of remodeling, the volume fraction had increased to 2.7% and the radius of fibers in the network had visibly increased.

Figure 4.6. Changes to fiber radius distribution during remodeling. The results are for Case 1 (constant addition, $k_4 = \kappa = 0$), at 20% initial strain, $\alpha = 0.9$, and a cell with stiffness equal to the network stiffness, but are representative of other cases and parameters**. (a)** The mean collagen fiber radius increased with remodeling before reaching equilibrium. **(b)** Before remodeling, all fibers (721 for this network) had a fiber radius of 50 nm. During remodeling, some fibers saw an increase in radius. The increase was not the same for all fibers because even though the addition rate was constant in Case 1, the removal rate was not.

Figure 4.7. Varying the rate of addition in Case 1. (a) For all α values, the rate of addition was larger than the rate of removal, leading to net deposition of collagen and increase in the collagen volume fraction with remodeling. **(b)** Increase in α resulted in

decrease in the cellular contribution to the equilibrium stress. For all α values, the cell stress appears to be approaching a plateau but does not reach it. **(c)** Representative remodeled network for Case 1 at 20% initial stretch.

Figure 4.8. Effect of cell stiffness. Representative results for Case 1, $\alpha = 0.9$. As the cell stiffness increased, the cell stress increased but the qualitative results were unchanged.

Figure 4.9. Remodeling with Case 2 – addition dependent on cell stretch. All plots are with $\alpha = 0.9$ and a cell with stiffness equal to that of the network. **(a)** As in Case 1, network stress went up with remodeling and cell stress decreased. **(b)** For all initial stretches, the system returned to almost its initial configuration. Only 500 remodeling steps shown for clarity. **(c)** The cell stress was only about 10% of total system stress. Cell stress increased with network stress and did not become homeostatic.

Figure 4.10. Remodeling with Case 3. (a) Representative data with $\alpha = 0.9$, 20% initial stretch, cell stiffness equal to network stiffness, and $\kappa = 0.02$. Parameters are the same for (b)-(d) but κ is varied. **(b)** The amount of deposited collagen increased with an increase in κ. **(c)** The system returned to a smaller strain and a higher value of κ resulted in a larger system contraction. **(d)** Increasing κ resulted in a decrease in the cell stress fraction from the total stress.

Figure 4.11. Remodeled networks in Case 3 – preferential deposition of fibers in direction of stretch (1-direction). Representative results with $\alpha = 0.9$ and 20% initial stretch. At $\kappa = 0$, collagen addition was constant for all fibers and not affected by fiber orientation. At even small increases of κ, a preferential deposition was observed - the fibers oriented in the 1-direction had a much larger radius.

Figure 4.12. Remodeling with Case 4. (a) Representative data with $\alpha = 0.9$, 20% initial stretch, cell stiffness equal to network stiffness, and $\kappa = 0.02$. Parameters are the same for (b)-(d) but κ is varied between 0.02 and 0.08. **(b)** The amount of deposited collagen increased with an increase in κ. **(c)** The system returned to a smaller strain and a higher value of κ resulted in a larger system contraction. **(d)** Increasing κ resulted in a decrease in the cell stress fraction from the total stress.

Figure 4.13. Remodeled networks in Case 4 - combining effects of cell stretch and preferential fiber deposition. At low 5% strain, Cases 2 and 4 are very similar, when the network has not rearranged much, and they both have larger collagen fibers than Case 3. At high strain, the collagen fibers in Case 4 have a visibly larger radius that those in Cases 2 and 3. Case 3 has the clearest difference in fiber radius between fibers aligned in the 1-direction and those perpendicular to it. In Case 4, the presence of the term which increases collagen deposition with cell stretch ensures that fibers in the other directions also see an increase in radius.

Figure 4.14. Comparing cellular contribution between cases. All cases produced similar results, though for some, the fraction of cell stress out of total stress was reduced. Data is with $\alpha = 0.9$ for all cases and $\kappa = 0.02$ for Cases 3 and 4

Figure 5.1 Structure of the glomerular filtration barrier. (a) Primary blood filtration happens in the part of kidneys called glomerulus. Unfiltered blood enters the glomerulus through the afferent arteriole, passes through a network of capillaries through the walls of which water and small molecules are filtered into urinary space, and the remaining blood exits the glomerulus through the efferent arteriole. **(b)** The walls of the glomerular capillaries are a 3-layered filter: starting from inside the capillary lumen, filtrate must pass through the pores of endothelial cells, the glomerular basement membrane, and channels in the epithelial cell layer.

Figure 5.2. Capillary geometry. The capillary was modeled as a two layered quarter section of a short cylinder; the inner layer represents the glomerular basement membrane (GBM) and the outer layer represent the podocytes. Initially, the capillary has a radius of 4 μm and thickness of 600 nm. Different representative networks were used in each layer but all networks were aligned to match the orientation of the finite elements. Pressure was applied to the elements of the inner layer to inflate the capillary before remodeling was initiated.

Figure 5.3. Constant fluid flow rate through the capillary wall was maintained throughout the remodeling time steps. These results are with the supercoiled α3(IV)α4(IV)α5(IV) network but the same is also true for the $[\alpha1(IV)]_2\alpha2(IV)$ networks. In contrast to the constant fluid flow rate, the pressure gradually lowered and Darcy permeability of the GBM increased.

Figure 5.4. Changes to average collagen IV radius due to remodeling. (a) With supercoiled networks, there is net addition of material. **(b)** With non-supercoiled networks, there is net removal of material.

Figure 5.5. Changes in stress, strain, and thickness of GBM and podocytes during remodeling. (a) When the GBM contains the supercoiled networks, stresses are reduced, the capillary diameter decreases, and the thickness of the system increases. **(b)** When the GBM contains the non-supercoiled networks, stresses increase, the capillary expands further, and the capillary wall becomes thinner.

Figure 5.6. Visualizing changes in capillaries dues to remodeling. (a) With the supercoiled networks, stresses in capillary are reduced and strains are lowered. **(b)** With the non-supercoiled networks, the capillary remains highly strained and stresses become even higher.

.

Chapter 1: Introduction

Chapter 1 covers the broad elements and background information needed to ease the reader into the next chapters. The background information includes a summary of the anatomy and physiology of the kidneys, with greater focus on the glomerulus and the components of the glomerular capillaries.

Chapter 2 presents a set of experiments in which the distensibility of a model basement membrane with and without α3(IV)α4(IV)α5(IV) collagen IV was compared. We showed that in the absence of the α3(IV)α4(IV)α5(IV) collagen IV network, basement membrane distensibility increases. The experiments provided proof for the importance of α3(IV)α4(IV)α5(IV) collagen IV networks, which are highly cross-linked, in the mechanical properties of select basement membranes.

Chapter 3 investigates the effects of cross-linking, in the form of supercoiling, on the mechanical and permeability properties of collagen IV networks. We generated computational models of collagen IV networks in the glomerular basement membrane and reconnected them to create different levels of supercoiling. We found that supercoiling greatly increases the stiffness of collagen IV networks but only minimally decreases the permeability, which is a very important ability for the proper function of the kidneys.

Chapter 4 is moving things in a new direction, as it covers topics of remodeling and tensional homeostasis in a generalized cell-matrix system. The remodeling insights from Chapter 4 are then used in Chapter 5 in a computational model of the glomerular

basement membrane and the cells which remodel it. The work in Chapter 5 also uses the supercoiled networks generated in Chapter 3.

1.1 Kidney anatomy and physiology

The kidneys perform a number of vital functions: they maintain water and solute balance in the body, clear the blood of toxins and metabolic byproducts, and secrete hormones and enzymes. Water and waste products filtered out in the kidneys follow the urinary tract until they leave the body. Blood filtration happens in specialized structures in the kidneys called nephrons (Figure 1.1). Each kidney has approximately a million nephrons; each nephron has two primary parts - glomerulus and tubules. We will focus on the glomerulus, which is the primary filtration site [1,2].

1.1.1 Glomerulus

The glomerulus (seen in detail in Figure 2.1) has two main components: Bowman's capsule and the glomerular capillary tuft [3]. Blood enters the glomerulus through the afferent arteriole, goes through the convoluted mass of capillaries in the tuft, called glomerular capillaries, and exits through the efferent arteriole. The capillary tuft is held together by a fibrous mesangial matrix and is suspended in urinary fluid enclosed by Bowman's capsule [1]. The blood pressure inside the glomerular capillaries is approximately 45 mmHg while the fluid pressure in Bowman's capsule is much lower at 10 mmHg; the difference in transcapillary hydrostatic pressure is 35 mmHg pointing

outwards from the capillary lumen. This transcapillary pressure difference is countered by the inner-pointing osmotic pressure difference. The net pressure difference forcing fluid and small molecules outwards from the glomerular capillaries is thus between 15 mmHg and 0 mmHg along the length of the glomerular capillaries (blood osmolarity increases from the afferent to the efferent ends of the glomerular capillaries). The above values come from experiments on Minich-Wister rats, but have been shown to be very similar to values form other animals, such as the squirrel monkeys and dogs which have similar glomerular size to humans [4,5].

Fluid and small molecules escaping the blood circulation must pass through the glomerular capillary wall, which is composed of 3 layers: endothelial cells lining the capillary lumen, glomerular basement membrane, and podocytes attached to the outer side of the capillaries [6,7]. The endothelial cells have a characteristic fenestrated structure - pores of ~50-80nm size span through the cytoplasm of the cells. On their luminal side (side not attached to the basement membrane) they are also covered in a layer of charged glycoproteins called the glycocalyx. While this layer and the fenestrated endothelial cells have been shown to contribute to the filtration of some macromolecules, it is still believed that endothelial cells do not play a significant role in the mechanical or hydraulic permeability properties of the glomerular capillaries [8]; these cells will not be discussed in detail below.

1.1.1.1 Glomerular basement membrane (GBM)

The glomerular basement membrane of the glomerular capillaries lies between the two cellular layers of epithelial and endothelial cells. It is similar to other basement membranes in the body as it is primarily composed of type IV collagen (discussed in detail below), laminin, nidogen, and proteoglycans; it provides support for cells and retains chemokines and growth factors. In addition to its normal basement membrane functions, the GBM is also responsible for providing tensile resistance to the high hydrostatic pressure of the glomerular capillaries and is an important component of the filtration barrier between blood and urinary space that limits the flow of water and solutes [9]. The mature GBM is actually two separate basement membranes synthesized independently by the epithelial and endothelial cells, which become fused together in later stages of glomerular development [10].

Type IV collagen is a member of the collagen family, together with 28 other currently known collagen types. It is found exclusively in basement membranes, where it forms regular, sheet-like, networks. The collagen IV molecule is a helix of 3 α chains that coil around each other. There are six known type IV collagen α chains which have been named α1 to α6, produced by separate genes, COL4A1 to COL4A6. Even though they are genetically distinct, the six α chains are highly homologous and are preserved across vertebrates [11]. They all have similar architecture: an amino terminal, referred to as the 7S domain; a carboxy terminal, the NC1 domain; and a collagenous Gly-X-Y repeated amino acid sequence with a number of non-collagenous interruptions. A typical collagen IV molecule is 400 nm long [12]. The process of three α chains coiling around each other to form a protomer is extremely selective. While in theory there are 56 possible

combinations of the six chains, in nature there are only three combinations discovered so far: [α1(IV)]2 α2(IV) - known as the major chain protomers, α3(IV)α4(IV)α5(IV) - known as the minor chain protomers, and [α5(IV)]2 α6(IV) [13]. The [α5(IV)]2 α6(IV) protomer will not be considered further in this study because it is found only at very small concentrations in a limited number of basement membranes [14]. The major chains are expressed in all basement membranes while the distribution of the minor chains is more limited. The minor chains are found only in the basement membranes of the glomerular capillaries, ocular lens, lung alveoli, and testes.

Protomers are secreted from cells in the extracellular space where they organize into networks, possibly with the guidance of laminin, though they are capable of self-assembly [15]. In network assembly, the NC1 end of one protomer is bound to the NC1 end of another protomer, forming a large globular domain in the middle of a dimer. The 7S ends are usually found as tetramers - bound to three other 7S ends. Networks organized in such a way would be highly regular, but protomers also interact with each other by forming lateral bonds and aligning (twisting) laterally to each other forming a structure called a supercoil. Evidence suggests that the major and minor protomers organize into separate networks when present in the same basement membrane [16]. Based on their molecular differences, it is theorized that the major and minor chain networks have different mechanical properties and topologies.

Laminin is a cross-shaped molecule with binding sites for integrins, nidogen, and other laminins, and is vital for the proper assembly of the GBM [17,18]. Nidogen is a small dumbbell-shaped molecule that facilitates the interaction between laminin and

collagen IV. There are many different types of proteoglycans in different tissue types; in the GBM, the most common type is agrin which has glycosaminoglycan side chains with a high negative charge which may be important for the filtration of ions [19, 20].

1.1.1.2 Podocytes

Podocytes are highly differentiated epithelial cells attached to the outer side of the glomerular basement membrane of the glomerular capillaries (Figure 1.2). They are a vital part of the glomerular filtration barrier and are also responsible for the production of components of the glomerular basement membrane [21]. Podocytes have a very recognizable structure: a rounded cell body (containing the nucleus) is suspended into the urinary space; from the cell body protrude feet-like processes that wrap around the circumference of the glomerular capillaries, giving the podocyte the appearance of an octopus wrapped around a tube. From each primary process there are secondary finger-like processes that are interdigitated and cover most of the GBM surface. The interdigitating secondary processes are separated by a distance of ~ 30-40nm and are connected by a zipper-like structure called the slit diaphragm through which passes the fluid filtered from the blood plasma [22].

The cytoskeleton of the podocytes is linked to molecules in the GBM through transmembrane receptors. The GBM-podocyte interaction is essential for the proper functioning of the filtration barrier. At different stages in maturation, podocytes secrete different isoforms of products found in the GBM. For example, in mature glomerular capillaries production of laminin-1 is replaced with production of laminin-11 and

[α1(IV)]2 α2(IV) collagen IV is replaced with α3(IV)α4(IV)α5(IV) collagen IV [23]. The cytoskeleton of podocytes is primarily composed of actin, microtubules, and intermediate filaments. In the foot processes, these cytoskeleton elements are aligned with the longitudinal axis of the processes. Podocytes cultured in vitro have been shown to respond to mechanical stresses by reorganizing their cytoskeleton: the cell body shrinks and the foot processes become longer and thinner [24]. Like the GBM, podocytes are covered in negatively-charged proteoglycans.

1.1.2 Tubuloglomerular feedback

The filtrate collected into the urinary space of Bowman's capsule enters a long tubular region that takes it to the urinary collecting ducts. The renal tubules have several characteristic sections and are able to reabsorb some of the primary filtrate based on the needs of the body (water, ion, and pH balance). Control over the glomerular filtration rate (GFR, amount of filtrate leaving the glomerular capillaries per unit time) is highly important for the maintenance of water and solute balance in the blood. Communication between tubules and glomerulus, as part of the tubuloglomerular feedback, allows the system to respond to changes and disturbances and maintain a set GFR [25].

Some of the important components in tubuloglomerular feedback are as follows: macula densa cells, granular cells, and extraglomerular mesangial cells. For each nephron, the tubule loops back and passes close to the glomerulus between the afferent and efferent arterioles (Figures 1.1 and 1.2). The epithelial cells lining the insides of the tubules in that section are called macula densa - they detect the flow and salt content

passing through the tubules at that point. The sensory properties of the cells come from cilia projections and uptake of sodium that changes the ion balance in the cells and initiates signaling in the cells. Granular cells are specialized smooth muscle cells in the afferent arteriole that secrete the enzyme renin. Renin is needed for the production of the protein angiotensin I, which is subsequently converted to angiotensin II, a known vasoconstricter that can act on the afferent and efferent arterioles. Therefore, the tubuloglomerualr feedback system has the ability to change the amount of blood flow into the glomerular capillaries, changing the hydrostatic pressure, and affecting the GFR [6].

1.2 References

1. Widmaier, E. P., Raff, H. & Strang, K. T. 2008 Vander's Human Physiology. 11th edn. New York, NY: McGraw-Hill.

2. Sgouralis, I. & Layton, A. T. 2015 Mathematical modeling of renal hemodynamics in physiology and pathophysiology. Math. Biosci. 264, 8–20. (doi:10.1016/j.mbs.2015.02.016)

3. Kriz, W., Gretz, N. & Lemley, K. V 1998 Progression of glomerular diseases: is the podocyte the culprit? Kidney Int. 54, 687–97. (doi:10.1046/j.1523-1755.1998.00044.x)

4. Brenner, B. M., Baylis, C. & Deen, W. M. 1976 Transport of molecules across renal glomerular capillaries. Physiol. Rev. 56, 502–34.

5. Lenihan, C. R., Busque, S., Derby, G., Blouch, K., Myers, B. D. & Tan, J. C. 2015 Longitudinal study of living kidney donor glomerular dynamics after nephrectomy. J. Clin. Invest. 125, 1311–1318. (doi:10.1172/JCI78885.Response)

6. Vander, A. J. 1995 Vander's Renal Physiology. 5th edn. New York, NY.

7. Kriz, W., Elger, M., Lemley, K. & Sakai, T. 1990 Structure of the glomerular mesangium: A biomechanical interpretation. Kidney Int. Suppl. 30, S2.

8. Jeansson, M. & Haraldsson, B. 2006 Morphological and functional evidence for an important role of the endothelial cell glycocalyx in the glomerular barrier. Am. J. Physiol. Renal Physiol. 290, F111–6. (doi:10.1152/ajprenal.00173.2005)

9. Drumond, M. C. & Deen, W. M. 1994 Structural determinants of glomerular hydraulic permeability. Am. J. Physiol. 266, F1–12.

10. Abrahamson, D. R. 1985 Origin of the Glomerular Basement Membrane Visualized after In Vivo Labeling of Laminin in Newborn Rat Kidneys. J. Cell Biol. 100, 1988–2000.

11. Khoshnoodi, J., Pedchenko, V. & Hudson, B. G. 2008 Mammalian collagen IV. Microsc. Res. Tech. 71, 357–70. (doi:10.1002/jemt.20564)

12. Yurchenco, P. D. & Ruben, G. C. 1988 Type IV collagen lateral associations in the EHS tumor matrix. Comparison with amniotic and in vitro networks. Am. J. Pathol. 132, 278–91.

13. Khoshnoodi, J., Cartailler, J.-P., Alvares, K., Veis, A. & Hudson, B. G. 2006 Molecular recognition in the assembly of collagens: terminal noncollagenous domains are key recognition modules in the formation of triple helical protomers. J. Biol. Chem. 281, 38117–21. (doi:10.1074/jbc.R600025200)

14. Borza, D. B., Bondar, O., Ninomiya, Y., Sado, Y., Naito, I., Todd, P. & Hudson, B. G. 2001 The NC1 domain of collagen IV encodes a novel network composed of the alpha 1, alpha 2, alpha 5, and alpha 6 chains in smooth muscle basement membranes. J. Biol. Chem. 276, 28532–40. (doi:10.1074/jbc.M103690200)

15. Yurchenco, P. D. 2011 Basement membranes: cell scaffoldings and signaling platforms. Cold Spring Harb. Perspect. Biol. 3. (doi:10.1101/cshperspect.a004911)

16. Kleppel, M. M., Fan, W., Cheong, H. I. & Michael, A. F. 1992 Evidence for Separate Networks of Classical and Novel Basement Membrane Collagen. J. Biol. Chem. 267, 4137–4142.

17. Miner, J. H. 2012 The glomerular basement membrane. Exp. Cell Res. 318, 973–978. (doi:10.1016/j.yexcr.2012.02.031.The)

18. Hohenester, E. & Yurchenco, P. D. 2016 Laminins in basement membrane assembly. Cell Adh. Migr. 7, 56–63. (doi:10.4161/cam.21831)

19. Bohrer, M. P., Baylis, C., Humes, H. D., Glassock, R. J., Robertson, C. R. & Brenner, B. M. 1978 Permselectivity of the Glomerular Capillary Wall. 61, 72–78.

20. Axelsson, J., Sverrisson, K., Rippe, A., Fissell, W. & Rippe, B. 2011 Reduced diffusion of charge-modified, conformationally intact anionic Ficoll relative to neutral Ficoll across the rat glomerular filtration barrier in vivo. Am. J. Physiol. Renal Physiol. 301, F708–12. (doi:10.1152/ajprenal.00183.2011)

21. Cellesi, F., Li, M. & Rastaldi, M. P. 2015 Podocyte injury and repair mechanisms. Curr. Opin. Nephrol. Hypertens. 24, 239–244. (doi:10.1097/MNH.0000000000000124)

22. Furukawa, T., Ohno, S., Oguchi, H., Hora, K., Tokunaga, S. & Furuta, S. 1991 Morphometric study of glomerular slit diaphragms fixed by rapid-freezing and freeze-substitution. Kidney Int. 40, 621–624. (doi:10.1038/ki.1991.253)

23. Miner, J. H. & Sanes, J. R. 1994 Collagen IV alpha 3, alpha 4, and alpha 5 chains in rodent basal laminae: sequence, distribution, association with laminins, and developmental switches. J. Cell Biol. 127, 879–91.

24. Endlich, N., Kress, K. R., Reiser, J., Uttenweiler, D., Kriz, W., Mundel, P. & Endlich, K. 2001 Podocytes respond to mechanical stress in vitro. J. Am. Soc. Nephrol. 12, 413–22.

25. Carlstrom, M., Wilcox, C. S. & Arendshorst, W. J. 2015 Renal Autoregulation in Health and Disease. Physiol. Rev. 95, 405–511. (doi:10.1152/physrev.00042.2012)

1.3 Figures

Figure 1.1. Structure of nephrons - the sites of filtration from blood to urinary space in the kidnesy. Nephrons have two main components - glomerulus (spherical enclosure of a clump of capillaries suspended in urinary space where primary filtration occurs) and tubules (long specilized reanal vessels that allow the kidneys to reabsorbe some of the filtered water and ions). Filtrate traveles through the tubules until it reaches the collecting duct and is later exreted from the body as urine. Figure reused with permission from [2]

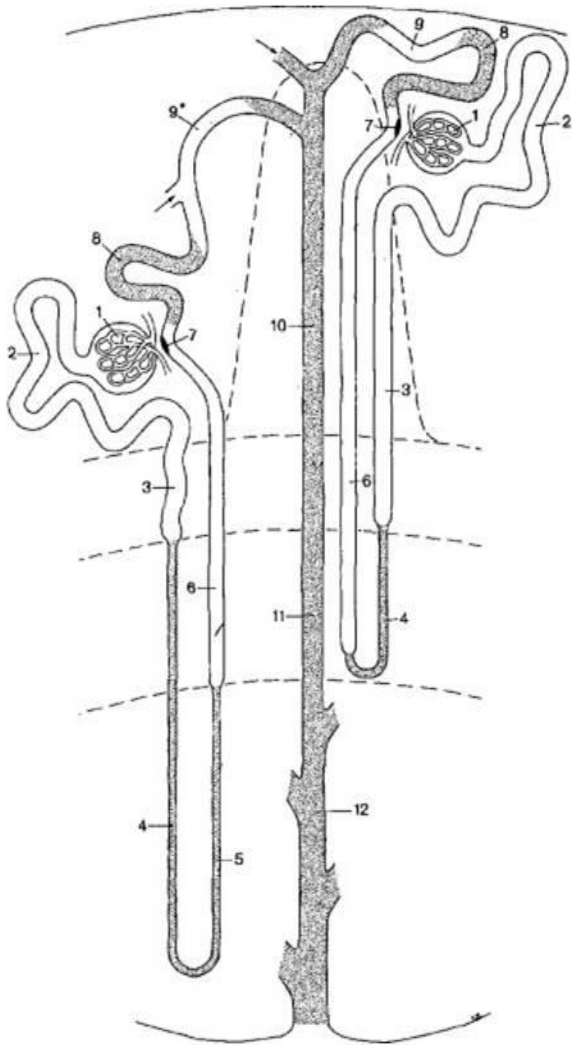

Figure 1.2. Anatomy of the glomerulus, seen in cross-section. Blood enters the glomerulus through the afferent arteriole (AA) goes through the long curved glomerular capillaries where some of the water and small molecules leave blood circulation and enter urinary space surrounded by a capsule (BC). Blood then exits the glomerulus through the efferent arteriole (EA). Glomerular capillaries are connected by a messangeal matrix and cells (M). The glomerualr capillaries (GC) are composed of three layers: endothelial cells lining the inner lumen, a basement membrane supporting those cells, and specylized epithelial cells, called podocytes, wrapped around the outer surface of the capillaries. Figure reused with permission from [3].

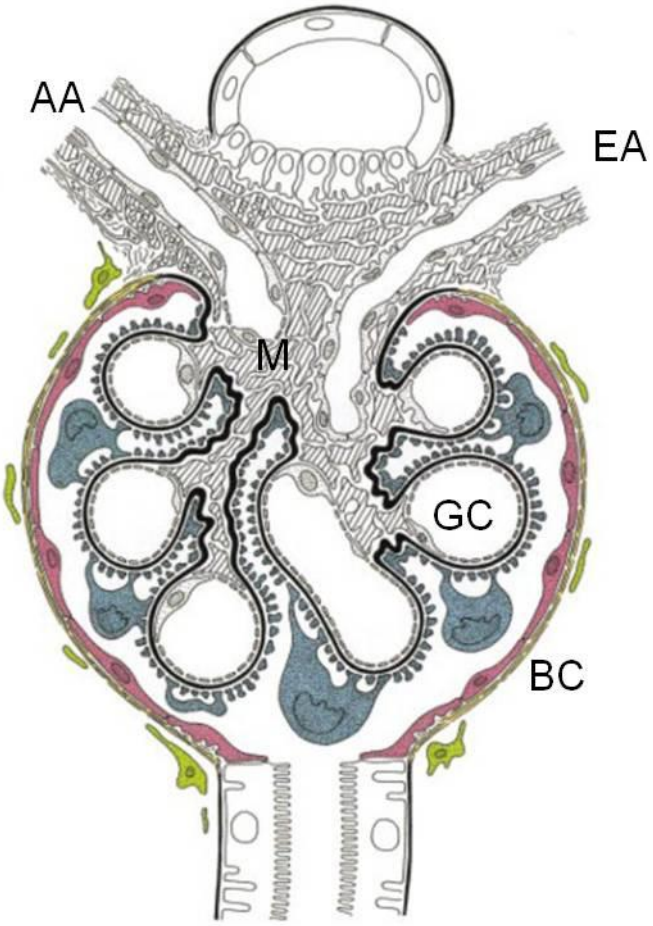

Chapter 2: Mechanical Response of Wild-Type and Alport Murine Lens Capsules During Osmotic Swelling

This chapter is part of the manuscript:

Gyoneva, L., Segal, Y., Dorfman, K. D., & Barocas, V. H. (2013). Mechanical response of wild-type and Alport murine lens capsules during osmotic swelling. *Experimental Eye Research*, *113*, 87-91.

2.1 Summary

The mechanical support of basement membranes, such as the lens capsule, is believed to arise from one of their main constituents – collagen IV. The basement membranes of the lens, kidney, and ear normally contain two different types of collagen IV networks, referred to as the major and minor chain networks. In Alport syndrome, a mutation in one of the minor chain *COL4* genes leads to the absence of the minor chain network, causing life-threatening disturbances. We hypothesized that the absence of the minor chain network increases basement membrane distensibility, as measured in wild-type (n=25) and Alport syndrome (n=21) mice using the lens capsule as a model. Osmotic swelling experiments revealed direction-dependent changes. As a reflection of lens capsule properties, Alport lenses strained significantly more than wild-type lenses in the anterior-posterior direction, i.e. along their thickness, but not in the equatorial

direction ($p=0.03$ and $p=0.08$, respectively). This is consistent with clinical data: Alport patients develop conical protrusions on the anterior and posterior lenticular poles. There was no evidence of significant change in total amount of collagen between Alport and wild-type lenses ($p=0.6$). The observed differences in distensibility could indicate that the major chain network alone cannot fully compensate for the absence of the more highly cross-linked minor chain network, which is believed to be stronger, more stable, and resistant to deformation. The addition of mechanical information on Alport syndrome to the currently available biological data provides a fuller picture into the progression of the disease.

2.2 Introduction

Basement membranes are ubiquitous structures that serve as cell attachment surfaces and also play a variety of other tissue-specific roles, including mechanical functions [27,40,43]. Basement membranes are primarily composed of type IV collagen, laminin, nidogen, and proteoglycans, but most of the mechanical support is thought to arise from covalently bonded type IV collagen [21,25,35,41]. Six α chains of type IV collagen, named α1(IV) to α6(IV) and encoded by genes COL4A1 to COL4A6, respectively, interact in a highly selective manner to form triple-helical protomers, which organize into a stable and flexible mesh. Among three known chain combinations, [α1(IV)]2α2(IV) protomers form the major chain network found in all basement membranes, α3(IV)α4(IV)α5(IV) protomers form the minor chain network present in

select basement membranes such as those of the kidney, eye, lung, testes, and ear, and [α5(IV)]2α6(IV) protomers are found in a further select subset of basement membranes including those in smooth muscle and developing lens [22,23,29].

The importance of type IV collagen is illustrated in several human diseases[18,23]. Notable among them, Alport syndrome is a hereditary disease of eye, kidney, and ear basement membranes caused by mutations in genes encoding minor chain constituents [20]. An estimated 85% of mutations occur in the COL4A5 gene encoding the α5(IV) chain and located on the X chromosome, such that males are affected more severely than females [6]. Mutations prevent the formation of the α3(IV)α4(IV)α5(IV) protomer, leading to loss or disruption of the minor chain network. Eye manifestations are manifold. In particular, anterior lenticonus is a characteristic defect of the anterior lens capsule (LC) affecting an estimated 25% of X-linked Alport patients and associated with central thinning of the LC, vertical crack formation, protrusion of the lens, and risk of spontaneous rupture [6,20]. Kidneys are the site of life-threatening disturbances. Progressive kidney disease is associated with changes of the glomerular basement membrane (GBM), a primary element within the kidney's filtration apparatus, characterized by localized thinning and thickening, delamination and splitting, and evidence of injury to adjacent glomerular cells [19, 20].

Changes to the structure of Alport basement membranes suggest decreased durability in the face of continuous mechanical demands that arise during lens accommodation, in the case of the LC, and glomerular filtration, in the case of the GBM. Such changes could have wide underpinnings including incorrect assembly of the

basement membrane in the absence of key components, secondary changes in composition (for example in laminins), increased susceptibility to proteolysis, injury to adjacent cells, and/or others. We hypothesized that basement membrane distensibility is increased in the absence of the minor chain network. Distensibility was measured in wild-type and X-linked Alport syndrome mice using the LC as a model basement membrane.

2.3 Methods

2.3.1 Lens swelling

Animal protocols were approved by the Institutional Animal Care and Use Committee at the University of Minnesota.

X-linked Alport syndrome mice transmitting a hemi/heterozygous Col4a5 nonsense mutation G5X were maintained on a C57BL/6 background [33]. Male mice between the ages of 7 and 8 weeks were euthanized in a CO_2 chamber and their tails snipped for post-hoc PCR genotyping. We adapted a recently described method for mechanical testing of the LC by osmotic swelling [32]. For each mouse, one lens was quickly removed, bathed in isotonic saline solution (0.9% w/v NaCl, 1 mM HEPES, pH 7.0) for 10 minutes, then transferred and bathed in hypotonic saline solution (0.3% w/v NaCl, 1 mM HEPES, pH 7.0) for 3 hours. Once the lens was transferred to the hypotonic bath, it was quickly positioned on its equatorial edge and imaged from above using a dissection microscope equipped with a CCD camera (Moticam 1000 1.3M pixel), fiber

optic light source, and calibration scale. Such positioning provided side views of the lens enabling determination of equatorial diameter and anterior-posterior lens thickness (Fig. 1). Images of the swelling lens were taken automatically at 1-minute intervals and used in the strain measurements as described below.

2.3.2 Strain Determination

Equatorial diameter (D) and lens thickness (T) were measured at 0, 0.25, 0.5, 0.75, 1, 2, and 3 hours using the Motic Image Plus software. To compare the distensibility of wild-type and Alport LCs, we calculated the equatorial (ε_{eq}), anterior-posterior thickness (ε_{apt}), and surface area linear strains (ε_{sa}) at each specified time point using the equations

$$\varepsilon_{eq}=(D^t-D^0)/\ D^0 \tag{2.1a}$$

$$\varepsilon_{apt}=(T^t-T^0)/\ T^0 \tag{2.1b}$$

$$\varepsilon_{sa}=(SA^t-SA^0)/\ SA^0 \tag{2.1c}$$

where the superscript 0 refers to the initial condition and the superscript t refers to the values at a given time. Surface area (SA) was calculated in MATLAB, treating the lens as an oblate ellipsoid, as judged on the basis of preliminary morphometric studies. To describe the anisotropy of the tissue response, a strain ratio (SR) was calculated defined as $SR=\varepsilon_{eq}\ /\varepsilon_{apt}$.

2.3.3 Collagen assay

Lens collagen content was determined by hydroxyproline-based methods [38] using a separate group of mice. For each mouse, both lenses were removed and cleaned of excess material by gently shaking in phosphate-buffered saline. Lenses were imaged for determination of equatorial diameter and lens thickness and calculation of surface area, as described above. Collagen content was determined from the measured amounts of hydroxyproline using the conversion factor 7.2µg collagen IV/µg hydroxyproline [2] and was normalized by the additive surface area of the two lenses.

2.3.4 Statistical analysis

All data are reported as means ± 95% confidence interval, except for the initial dimensions data which are presented as means ± standard deviation. Data with repeated measurements over time (e.g. strain, strain ratio) were modeled with a mixed effects linear model in R (http://www.r-project.org/) using the *lme4* package, and in SAS (SAS Institute, Cary NC, 2009) Proc Mixed. For each experiment, the fixed effects were genotype, time, and the time-genotype interaction; a random intercept for each lens was used to model the correlation between repeated measurements. When the time-genotype interaction was significant ($p<0.05$), p-values for comparisons were adjusted using the

Bonferroni method. A two-tailed t-test was used to check for significant difference between all other data sets. An F test was performed to check for differences in variance.

2.4 Results

2.4.1 Initial dimensions

Initial equatorial diameter and lens thickness for wild-type (n=25) and Alport (n=21) lenses are plotted in Fig. 2. The variances of the wild-type and Alport groups were different both for the equatorial diameter ($p<0.01$) and lens thickness ($p=0.02$). There were no significant differences in the initial dimensions between wild-type and Alport lenses (Table 1). The equatorial diameter was significantly higher ($p<<0.01$) than the lens thickness for both wild-type and Alport lenses. The aspect ratio (equatorial diameter/lens thickness) did not differ between wild-type (1.17 ± 0.02) and Alport (1.18 ± 0.02) lenses ($p=0.26$).

2.4.2 Strain

Equatorial and thickness strains elicited by osmotic swelling increased sharply during the first hour and then leveled off (Fig. 3). The plateau reached after 3 hours of swelling is very close to steady state: In preliminary experiments the strain at 6 hours of swelling differed by only 0.6% from the strain at 3 hours of swelling. The thickness strain

curves differed significantly between wild-type and Alport lenses (p=0.03), with post-hoc analysis identifying higher strains for Alport at the 2-hour (7.8±1.1% versus 6.5±0.8; p=0.02) and 3-hour (8.2±1.1% versus 6.7±1.0%; p<0.01) time points. The equatorial strain curves trended towards a significant difference (p=0.08). Surface area strain curves (Fig. 3) did not differ between wild-type and Alport lenses (p=0.49). None of the LCs ruptured under our experimental conditions.

As seen from the ratio of equatorial to thickness strain (Fig. 4), the tissue behaved anisotropically, that is exhibiting spatial inhomogeneities. Thickness strain was larger than equatorial strain at all time points and the strain ratio slightly decreased over time. There was no statistically significant difference between the wild-type and Alport curves (p=0.23).

2.4.3 Collagen assay

There was no statistically significant difference (p=0.60) between the total collagen content of wild-type (0.28±0.06 μg/mm^2, n=5) and Alport (0.29±0.03 μg/mm^2, n=6) lenses.

2.5 Discussion

We hypothesized that primary changes in Alport basement membranes would be evident as differences in mechanical properties relative to wild-type. Using the LC as a

model basement membrane, osmotic swelling experiments revealed a direction-dependent difference in distensibility between wild-type and Alport LCs: Alport thickness strain, as determined from the change in lens thickness elicited by osmotic swelling, was significantly greater than wild-type thickness strain but no such difference was found in the equatorial direction or in the overall expansion of the membrane. Thickness strain was greater than equatorial strain for both groups. The variance in initial Alport lens dimensions was significantly larger than that of the wild-type lenses. There was no evidence of differences in total collagen amounts between wild-type and Alport lenses.

The LC deforms in response to applied forces, as governed by microstructural adaptations within the type IV collagen network [3,4,12]. Under our experimental conditions, Alport LCs showed signs of increased distensibility at a young age. The difference in mechanical properties is consistent with the formation of lenticonus in some Alport patients, which is believed to occur when the LC is not stiff enough to support proper lens shape at the anterior or posterior poles of the lens [37,39]. Increase in equatorial strain was not statistically significant. The differences between equatorial and thickness strains in our study could have been related to regional inhomogeneities in ultrastructure and material properties [7,8,24] and/or the inherent tendency of ellipsoidal pressure vessels to expand more in short than long axes [5].

To investigate the possibility that the increase in distensibility of Alport LCs was caused by changes in total collagen amounts, not just the loss of the minor chain, a collagen assay measured the collagen content in the whole lens. The assay revealed that

total collagen amounts in Alport lenses were not statistically different though it is possible that the assay was not sensitive enough to detect small or localized losses. Previous studies have shown that the loss of the minor collagen IV chains results in overproduction of the major collagen IV chains[19] and introduction of other collagen types into the basement membrane [36]. However, as indicated by the distensibility data, the alternate collagens cannot replace the mechanical contribution of the minor chains.

The importance of the minor chain network for the structure of basement membranes was investigated in a seminal study of the bovine GBM [16]. The study found the minor chain type IV collagen network to be distinct from the major chain network in that the former is marked by protomeric supercoils stabilized by disulfide cross-links. The significance of network cross-linking for the stability and resistance to deformation of synthetic polymer networks is well known in materials science [13,17]. Collagen IV networks, though they are biological structures, follow the same rules, leading some [1,23,44] to postulate that the higher level of cross-linking in the minor chain network contributes additional strength/stability to basement membranes. Thus, Alport basement membranes would be expected to strain further than wild-type basement membranes.

There are no experimental studies on the mechanics of other Alport basement membranes, but an investigation on whole glomeruli from Alport mice [42] presented results comparable to our own. The capillary tuft of renal glomeruli is supported by the GBM; therefore the properties of the glomeruli indirectly reflect the properties of the GBM. Using atomic force microscopy measurements of isolated mouse X-linked Alport

glomeruli, Wyss et al. [42] found that at 4 months, the nominal Young's modulus (slope of the stress-strain curve, indicative of stiffness) of Alport glomeruli was 28% lower than that of wild-type, meaning that glomeruli were significantly less stiff in the absence of the minor chain collagen IV network. The LC may be a useful model for mechanical changes occurring in the GBM, where serious consequences of Alport syndrome occur but which is not amenable to mechanical testing. However, the exact relationship between minor chain collagen IV concentration and basement membrane mechanics would require further investigation.

The minor chains constitute only 6% of total collagen IV amount in the LC [26]. In our experiments we saw a 21% increase in thickness strain in Alport LCs but considering the small minor chain concentration, how they exert a significant effect on LC mechanics is still unclear. In the GBM, the minor chains constitute 30% of total collagen IV amount [26], so one could expect a larger decrease in stiffness than the observed 28% by Wyss et al. (2011) [42] in the whole glomerulus. However, their study was performed on 4-month old mice, at a stage when significant scarring of the kidneys is usually observed [36]. The absence of the highly cross-linked minor chain network may change the distensibility of the Alport LC by other mechanisms, for example by generalized or localized thinning. We cannot exclude the possibility of such thinning, especially if localized, more pronounced with age, and/or occurring in patterns uncorrelated with and thus undetectable by our collagen assays.

The inherent assumptions of our passive osmotic swelling method are that the osmotic driving force and hydraulic permeability of lenses are not altered by the Alport

mutation, such that differences in distensibility are determined by the LC alone, the major expansion-resisting element of the lens [9]. In our experiments, we investigated the defining properties of the Alport LC at a point where assumptions regarding the lack of mutation effect on osmotic driving force and hydraulic permeability were most likely to be valid. It is important to emphasize that the mice were at an early stage of the disease. Ocular manifestations, and in particular anterior lenticonus, represent a late complication and final step in a cumulative injury pathway in which the mechanical properties of the LC play continuing, changing and non-exclusive roles [14]. We cannot exclude the possibility that changes in these parameters also contributed to passive osmotic swelling behavior in our mouse model or that such changes become increasingly important during the progression of Alport eye disease in humans.

The coupling of mechanical and biological factors in the progression of Alport syndrome has received more recent attention [1,28]. Reports on lens epithelial cells show that loss of mechanical homoeostasis results in abnormal differentiation and deposition of fibrous material in the LC [31,34]. Glomerular cells respond to mechanical strain by altering production of matrix metalloproteinases [28], initiation of sclerosis through SPARC [10], and adaptations of the actin cytoskeleton [11]. Thus, it is becoming clearer that biological responses may be initiated, at least in part, by an increase in strain due to the loss of the minor chain collagen IV network, which is further supported by our results. Most proposed treatments for Alport syndrome have targeted secondary pathways of tissue injury and inflammation. There have been reports of successful treatment strategies although none yet translating to the human disease [15, 30]. An increased focus

on the mechanics of basement membranes could be illuminating for the development of new treatment targets.

In summary, changes in the mechanical properties of LCs are evident at early stages of mouse Alport syndrome. The results from the LC offer insight into the mechanical changes of the GBM, which is also significantly affected in Alport syndrome. The increased distensibility of Alport basement membranes is likely an important initiator of the pathological cellular responses contributing to the progression of the disease. Understanding the root of these pathological changes is vital for development of treatments.

2.6 References

1. Barocas, V.H., Dorfman, K.D., Segal, Y., 2012. A model of strain-dependent glomerular basement membrane maintenance and its potential ramifications in health and disease. J. Biomech. Eng. 134, 081006.

2. Bejarano, P.A., Langeveld, J.P., Hudson, B.G., Noelken, M.E., 1989. Degradation of basement membranes by Pseudomonas aeruginosa elastase. Infect. Immun. 57, 3783-3787.

3. Burd, H.J., 2009. A structural constitutive model for the human lens capsule. Biomech. Model Mechanobiol. 8, 217-231.

4. Burd, H.J., Judge, S.J., Cross, J.A., 2002. Numerical modelling of the accommodating lens. Vision Res. 42, 2235-2251.

5. Charrier, J.M., Shrivastava, S., Wu, R., 1989. Free and constrained inflation of elastic membranes in relation to thermoforming - non-axisymmetric problems. J. Strain Anal. Eng. 24, 55-74.

6. Colville, D.J., Savige, J., 1997. Alport syndrome. A review of the ocular manifestations. Ophthalmic Genet. 18, 161-173.

7. Danysh, B.P., Czymmek, K.J., Olurin, P.T., Sivak, J.G., Duncan, M.K., 2008. Contributions of mouse genetic background and age on anterior lens capsule thickness. Anat. Rec. (Hoboken) 291, 1619-1627.

8. David, G., Pedrigi, R.M., Heistand, M.R., Humphrey, J.D., 2007. Regional multiaxial mechanical properties of the porcine anterior lens capsule. J. Biomech. Eng. 129, 97-104.

9. Duncan, G., 1970. Permeability of amphibian lens membranes to water. Exp. Eye Res. 9, 188-197.

10. Durvasula, R.V., Shankland, S.J., 2005. Mechanical strain increases SPARC levels in podocytes: implications for glomerulosclerosis. Am. J. Physiol. Renal Physiol. 289, F577-584.

11. Endlich, N., Kress, K.R., Reiser, J., Uttenweiler, D., Kriz, W., Mundel, P., Endlich, K., 2001. Podocytes respond to mechanical stress in vitro. J. Am. Soc. Nephrol. 12, 413-422.

12. Fisher, R.F., Wakely, J., 1976. The elastic constants and ultrastructural organization of a basement membrane (lens capsule). Proc. R. Soc. Lond. B. Biol. Sci. 193, 335-358.

13. Fried, J.R., 2003. Polymer Science and Technology. Prentice Hall, Upper Saddle River, NJ.

14. Govan, J.A., 1983. Ocular manifestations of Alport's syndrome: a hereditary disorder of basement membranes? Br. J. Ophthalmol. 67, 493-503.

15. Gross, O., Kashtan, C.E., 2009. Treatment of Alport syndrome: beyond animal models. Kidney Int. 76, 599-603.

16. Gunwar, S., Ballester, F., Noelken, M.E., Sado, Y., Ninomiya, Y., Hudson, B.G., 1998. Glomerular basement membrane. Identification of a novel disulfide-cross-linked network of alpha3, alpha4, and alpha5 chains of type IV collagen and its implications for the pathogenesis of Alport syndrome. J. Biol. Chem. 273, 8767-8775.

17. Hiemenz, P.C., Lodge, T.P., 2007. Polymer Chemistry. CRC Press, Boca Raton, FL.

18. Hudson, B.G., Reeders, S.T., Tryggvason, K., 1993. Type IV collagen: structure, gene organization, and role in human diseases. Molecular basis of Goodpasture and Alport syndromes and diffuse leiomyomatosis. J. Biol. Chem. 268, 26033-26036.

19. Kalluri, R., Shield, C.F., Todd, P., Hudson, B.G., Neilson, E.G., 1997. Isoform switching of type IV collagen is developmentally arrested in X-linked Alport syndrome leading to increased susceptibility of renal basement membranes to endoproteolysis. J. Clin. Invest. 99, 2470-2478.

20. Kashtan, C.E., 1999. Alport syndrome. An inherited disorder of renal, ocular, and cochlear basement membranes. Medicine (Baltimore) 78, 338-360.

21. Kefalides, N.A., 1981. Basement membrane: structure function relationships. Ren. Physiol. 4, 57-66.

22. Kelley, P.B., Sado, Y., Duncan, M.K., 2002. Collagen IV in the developing lens capsule. Matrix Biol. 21, 415-423.

23. Khoshnoodi, J., Pedchenko, V., Hudson, B.G., 2008. Mammalian collagen IV. Microsc. Res. Tech. 71, 357-370.

24. Krag, S., Andreassen, T.T., 2003. Mechanical properties of the human lens capsule. Prog. Retin. Eye Res. 22, 749-767.

25. Krag, S., Olsen, T., Andreassen, T.T., 1997. Biomechanical characteristics of the human anterior lens capsule in relation to age. Invest. Ophthalmol. Vis. Sci. 38, 357-363.

26. Langeveld, J.P., Wieslander, J., Timoneda, J., McKinney, P., Butkowski, R.J., Wisdom, B.J., Jr., Hudson, B.G., 1988. Structural heterogeneity of the noncollagenous domain of basement membrane collagen. J. Biol. Chem. 263, 10481-10488.

27. LeBleu, V.S., Macdonald, B., Kalluri, R., 2007. Structure and function of basement membranes. Exp. Biol. Med. (Maywood) 232, 1121-1129.

28. Meehan, D.T., Delimont, D., Cheung, L., Zallocchi, M., Sansom, S.C., Holzclaw, J.D., Rao, V., Cosgrove, D., 2009. Biomechanical strain causes maladaptive gene regulation, contributing to Alport glomerular disease. Kidney Int. 76, 968-976.

29. Miner, J.H., Sanes, J.R., 1994. Collagen IV alpha 3, alpha 4, and alpha 5 chains in rodent basal laminae: sequence, distribution, association with laminins, and developmental switches. J. Cell. Biol. 127, 879-891.

30. Noone, D., Licht, C., 2012. An update on the pathomechanisms and future therapies of Alport syndrome. Pediatr. Nephrol.

31. Pedrigi, R.M., Dziezyc, J., Humphrey, J.D., 2009. Altered mechanical behavior and properties of the human anterior lens capsule after cataract surgery. Exp. Eye. Res. 89, 575-580.

32. Powell, T.A., Amini, R., Oltean, A., Barnett, V.A., Dorfman, K.D., Segal, Y., Barocas, V.H., 2010. Elasticity of the porcine lens capsule as measured by osmotic swelling. J. Biomech. Eng. 132, 091008.

33. Rheault, M.N., Kren, S.M., Thielen, B.K., Mesa, H.A., Crosson, J.T., Thomas, W., Sado, Y., Kashtan, C.E., Segal, Y., 2004. Mouse model of X-linked Alport syndrome. J. Am. Soc. Nephrol. 15, 1466-1474.

34. Saika, S., Kawashima, Y., Miyamoto, T., Okada, Y., Tanaka, S.-I., Ohmi, S., Minamide, A., Yamanaka, O., Ohnishi, Y., Ooshima, A., Yamanaka, A., 1998. Immunolocalization of prolyl 4-hydroxylase subunits, alpha-smooth muscle actin, and extracellular matrix components in human lens capsules with lens implants. Exp. Eye. Res. 66, 283-294.

35. Sakai, T., Kriz, W., 1987. The structural relationship between mesangial cells and basement membrane of the renal glomerulus. Anat. Embryol. (Berl) 176, 373-386.

36. Sayers, R., Kalluri, R., Rodgers, K.D., Shield, C.F., Meehan, D.T., Cosgrove, D., 1999. Role for transforming growth factor-beta1 in alport renal disease progression. Kidney Int. 56, 1662-1673.

37. Seymenoglu, G., Baser, E.F., 2009. Ocular manifestations and surgical results in patients with Alport syndrome. J. Cataract Refract. Surg. 35, 1302-1306.

38. Stegemann, H., Stalder, K., 1967. Determination of hydroxyproline. Clin. Chim. Acta 18, 267-273.

39. Streeten, B.W., Robinson, M.R., Wallace, R., Jones, D.B., 1987. Lens capsule abnormalities in Alport's syndrome. Arch. Ophthalmol. 105, 1693-1697.

40. Timpl, R., Brown, J.C., 1996. Supramolecular assembly of basement membranes. Bioessays 18, 123-132.

41. West, J.B., Tsukimoto, K., Mathieu-Costello, O., Prediletto, R., 1991. Stress failure in pulmonary capillaries. J. Appl. Physiol. 70, 1731-1742.

42. Wyss, H.M., Henderson, J.M., Byfield, F.J., Bruggeman, L.A., Ding, Y., Huang, C., Suh, J.H., Franke, T., Mele, E., Pollak, M.R., Miner, J.H., Janmey, P.A., Weitz, D.A., Miller, R.T., 2011. Biophysical properties of normal and diseased renal glomeruli. Am. J. Physiol. Cell Physiol. 300, C397-405.

43. Yurchenco, P.D., 2010. Basement Membranes: Cell Scaffoldings and Signaling Platforms. Cold Spring Harbor Perspectives in Biology.

44. Yurchenco, P.D., Amenta, P.S., Patton, B.L., 2004. Basement membrane assembly, stability and activities observed through a developmental lens. Matrix Biol. 22, 521-538.

2.7 Tables

Table 2.1: Initial wild-type (WT) and Alport lens dimensions. Results are presented as mean ± standard deviation. Initial equatorial diameter and lens thickness were defined as the measurements after 3 minutes in hypotonic saline solution. There was no difference between the wild-type (WT, n=25) and Alport (n=21) dimensions (p-values presented in the last row). Equatorial diameter was greater than lens thickness in both groups (p-values presented in the last column).

	Equatorial	Thickness	p-value
WT	2399±42μm	2052±35μm	<<0.01
Alport	2401±74μm	2042±59μm	<<0.01
p-value	0.89	0.49	

2.8 Figures

Figure 2.1: Lens imaging. For the swelling experiments, lenses were positioned on their equatorial edge, providing a side view for determination of equatorial diameter (D) and anterior-posterior lens thickness (T).

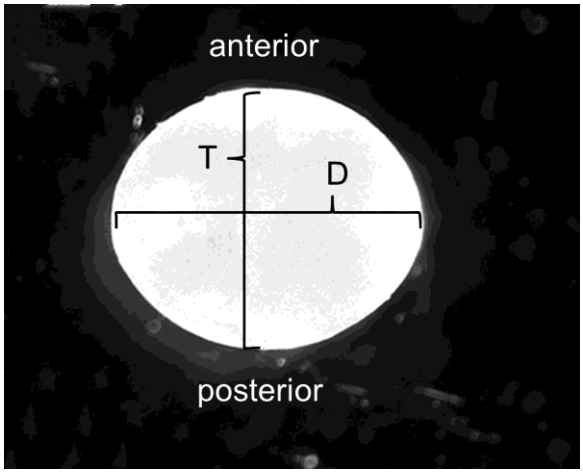

Figure 2.2: Relationship between equatorial diameter and lens thickness. Equatorial diameter was larger than lens thickness in both Alport (□) and wild-type (WT) (●) lenses. The distributions of dimensions for Alport lenses were visibly wider than those for wild-type lenses.

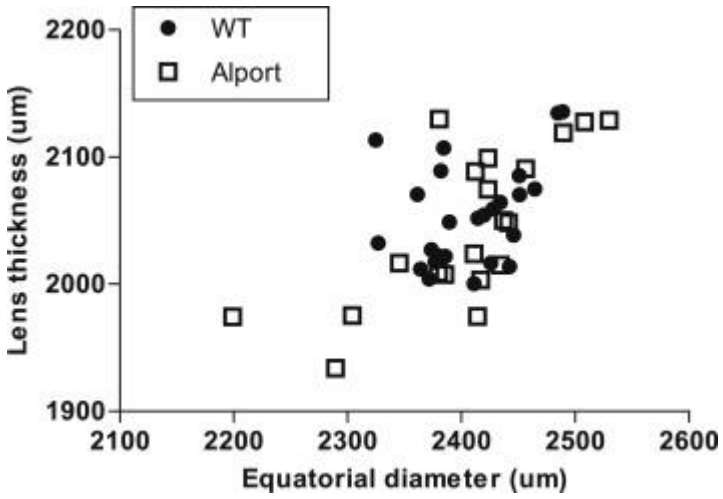

Figure 2.3. Linear strains. (A) Equatorial strain. Defined as in Equation 2.1a and calculated at seven different time points. The wild-type (WT) (●) and Alport (□) curves trended toward significance ($p<0.1$). **(B)** Thickness strain (Equation 2.1b). Alport strain was significantly larger than wild-type (WT) strain at the two- and three-hour time points (indicated with an asterisk, $p<0.05$). **(C)** Surface area strain (Equation 2.1c). There was no statistically significant difference between the wild-type (WT) and Alport strain curves ($p>0.05$).

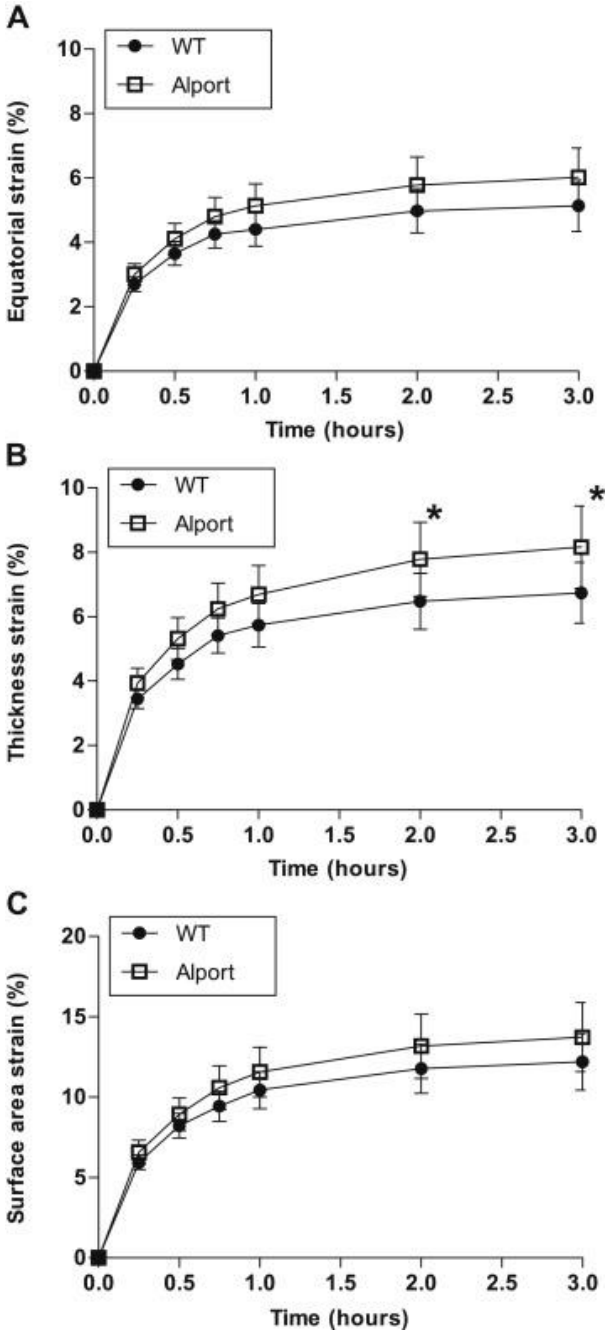

Figure 2.4: Lens anisotropy over time. Anisotropy was defined as the ratio of equatorial/lens thickness strain (SR). SR was calculated at different time points to investigate the relationship between the directional strains. There was no statistically significant difference between the wild-type (WT) (●) and Alport (□) curves ($p>0.05$).

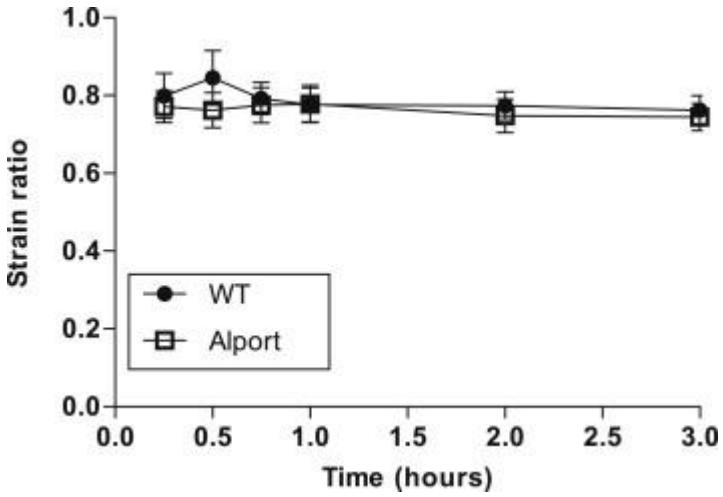

Chapter 3: Effect of supercoiling on the mechanical and permeability properties of model collagen IV networks

This chapter is part of the manuscript:

Gyoneva, L., Segal, Y., Dorfman, K. D., & Barocas, V. H. (2015). Effect of Supercoiling on the Mechanical and Permeability Properties of Model Collagen IV Networks. *Annals of biomedical engineering*, *43*(7), 1695-1705.

3.1 Summary

Collagen IV networks in the glomerular basement membrane (GBM) are essential for the maintenance and regulation of blood filtration in the kidneys. The GBM contains two different types of collagen IV networks: $[\alpha1(IV)]_2\alpha2(IV)$ and $\alpha3(IV)\alpha4(IV)\alpha5(IV)$, the latter of which has a higher number of supercoils (two or more collagens coiling around each other). To investigate the effects of supercoiling on the mechanical and permeability properties of collagen IV networks, we generated model collagen IV networks in the GBM and reconnected them to create different levels of supercoiling. We found that supercoiling greatly increases the stiffness of collagen IV networks but only minimally decreases the permeability. Also, doubling the amount of supercoils in a network had a bigger effect than doubling the stiffness of the supercoils. Our results suggest that the formation of supercoils is a specialized mechanism by the GBM that

provides it with a network stiff and strong enough to withstand the high hydrostatic pressures of filtration, yet porous enough that filtration is not hindered. Clinically, understanding the effects of supercoiling gives us insight into the mechanisms of GBM failure in some disease states where the normal collagen IV structure is disrupted.

3.2 Introduction

In the kidneys, blood filtration occurs in microscopic capillary clusters called glomeruli (Fig. 1). As blood flows through the semi-permeable glomerular capillaries, small solutes and water can leave the blood stream and enter the urinary space while large molecules (notably albumin) are mostly retained. Fluid flow across the capillary wall is driven by a large hydrostatic pressure difference, ~40 mmHg, that overcomes the osmotic pressure generated by the blood proteins [4,8]. The primary structural component of the glomerular capillary is the glomerular basement membrane (GBM), which is mainly composed of type IV collagen [17,21]. The GBM has a unique structure and composition, specialized to allow a high hydraulic conductivity while maintaining a collagen IV network stiff and strong enough to withstand the hydrostatic pressure [25,26,44].

Unlike many other collagens, which form fibrils and fibers, collagen IV forms networks on the nanoscale based on specific end-to-end interactions. The carboxy termini of collagen IV protomers (triple helices comprised of individual α(IV) collagen chains) connect into dimers, and the amino ends connect into tetramers, creating a network

resembling chicken wire but with significant lateral interactions between protomers [21,51]. Such side-by-side connections occur when two or more collagen IV protomers twist around each other, forming a supercoil [52,53]. Supercoiled segments of protomers correspond to sites of higher stiffness and supercoiling is interrupted in some locations by sites of higher flexibility due to interruptions in the regular Gly-X-Y collagenous sequence [19]. Many of the interruptions are conserved for different collagen IV isoforms, suggesting that they are important [32].

Collagen IV isoforms vary in their spatial and temporal distribution. The majority of basement membranes contain only $[\alpha1(IV)]_2\alpha2(IV)$ networks. In the GBM, and in a small number of other basement membranes, a second network is found - $\alpha3(IV)\alpha4(IV)\alpha5(IV)$ [37]. In healthy mature GBM, the two networks are separate - the $[\alpha1(IV)]_2\alpha2(IV)$ collagen IV network occupying the endothelial side of the capillary wall, and the $\alpha3(IV)\alpha4(IV)\alpha5(IV)$ collagen IV network on the epithelial side [48]. In the genetic disease Alport syndrome, a mutation prevents proper assembly/formation of the $\alpha3(IV)\alpha4(IV)\alpha5(IV)$ network or its incorporation into the GBM. The absence of the $\alpha3(IV)\alpha4(IV)\alpha5(IV)$ network results in a series of glomerular abnormalities (e.g. blood proteins leaking into the urinary space, splitting and scarring of the GBM) ultimately leading to kidney failure [20,24]. $[\alpha1(IV)]_2\alpha2(IV)$ is overproduced in Alport GBMs, possibly in an attempt to replace the missing $\alpha3(IV)\alpha4(IV)\alpha5(IV)$, but $[\alpha1(IV)]_2\alpha2(IV)$ alone does not seem capable of supporting the glomerular capillaries and normal filtration [23].

Many questions have been raised about the role of the α3(IV)α4(IV)α5(IV) network. There is increasing evidence that the α3(IV)α4(IV)α5(IV) network has different mechanical properties. In a mouse model of Alport syndrome, Alport lens basement membranes were shown to be significantly more distensible than healthy ones in a direction-dependant manner [15]. An investigation by Wyss et al. (2011) on whole glomeruli revealed that Alport glomeruli have a significantly lower elastic modulus [50]. Moreover, hydraulic conductivity may be decreased in Alport GBMs [27].

Compared to the α1 and α2 chains, the α3, α4, and α5 chains have a higher number of non-collagenous interruptions and an increased number of cysteine residues, which are believed to stabilize supercoils [14]. Structurally, the α3(IV)α4(IV)α5(IV) collagen IV network is described as being tighter, with a noticeably higher number of supercoils [14,23,32]. We hypothesized that an increased level of supercoiling, as seen in the α3(IV)α4(IV)α5(IV) collagen IV network, could account for the mechanical and permeability differences seen in healthy and Alport GBMs. In general, a more highly cross-linked polymer network is known to be stiffer, more stable, and resistant to creep and degradation [34]. This work presents a model of supercoiling in collagen IV networks, and how the structural differences within the collagen IV isoforms affect their mechanical and permeability properties.

3.3 Methods

Voronoi networks were used to represent collagen IV networks. The network model is primarily based on data from the GBM, but it could be applied to other basement membranes. The Voronoi networks were modified to model increased levels of supercoiling. Biologically, the different isoforms are produced and incorporated separately, but we are interested in comparing effects of supercoiling directly, so we transformed an $[\alpha1(IV)]_2\alpha2(IV)$-like network to a $\alpha3(IV)\alpha4(IV)\alpha5(IV)$-like network. The level of supercoiling was varied to investigate the relationship between supercoiling and mechanical/permeability properties.

3.3.1 Network generation

Voronoi networks have been used previously to represent type I collagen fiber networks [16,33,39]. Random 3D Voronoi networks were generated in Matlab using the built-in voronoin function as described in Stylianopoulos et al. (2008) [47]. Each edge in the final Voronoi network represented a segment of a collagen IV protomer forming part of a laterally connected network (Fig. 2a). The vertices of the Voronoi network could represent either branch points of a lateral interaction or tetrameric end-to-end connections. The networks were generated in a representative volume element (RVE) of size 560x560x175 nm – approximately half the thickness of the human GBM [9]. To match the collagen IV volume density of the GBM more closely, five interpenetrating networks were combined in the RVE. The radius, r, of each collagen IV segment was set to 3.5 nm [9]. These original networks were representative of the biological

$[\alpha1(IV)]_2\alpha2(IV)$ networks which already have some level of supercoiling. The base level of supercoiling in the original networks was not considered however, and we only looked at the effects of increasing the amount of supercoiling.

3.3.2 Supercoiling

Supercoiling in collagen IV networks was modeled by reconnecting the original Voronoi networks as described in Fig 2b. Going through every node in the original network, n_i, the two segments from a node going in the same direction (smallest angle, α_s) were combined along their midline M. Because in the model each segment can be supercoiled only once and supercoils longer than the original segment are not allowed, supercoils did not form at every node. To vary the amount of supercoiling in a network, the segments were combined for different distances based on a percentage of the length of the midline, p_m which will be referred to as supercoil ratio. Five cases were generated: p_m = 10%, 20%, 30%, 40%, 50%. Increasing p_m thereby increased the total amount of coiling in the network. The combined segment is referred to as a supercoil and given a radius $2r$. At the end of the supercoil, the two combined protomers were branched and returned to their original nodes. The length of the supercoil was set so that its total mass was equal to that of the original segments, resulting in a decreased rest length. For example, if two original segments were 20nm long, and they were combined for a supercoil of length 10nm, the leftover length should be 10nm long in each segment. The arms of the resulting Y shape, however, must be 10.66 nm long if the nodes do not move.

To account for this newly created length, the equilibrium lengths of the supercoiled segments were artificially shortened, meaning that the networks were pre-stressed. Supercoils were generated by combining only two original segments although higher-order supercoils have been observed among protomers in biological collagen IV networks [43].

Our supercoiling model does not take into account any bending angles, periodicity of coiling, or torsion in the coiled segments. The model only compares the effect of re-organizing a network to contain a higher number of supercoils. The properties of interest to us are the length of the supercoils, the total amount of coiled material in the network and the stiffness of the newly formed supercoil.

3.3.3 Network deformation

Before the simulated equibiaxial stretch experiment, the supercoiled networks were equilibrated to minimize their pre-stress. Equibiaxial stretch was chosen to simulate the conditions of the GBM in the glomerular capillaries, in which pressure is balanced by axial and circumferential stresses in the capillary wall. Stretching was performed based on the method described in Chandran and Barocas (2007) [6] applied to single three-dimensional RVE collagen IV networks in this case. Collagen IV protomers were modeled as nonlinear springs with the governing equation

$$F = \frac{EA}{B}(\exp(Be_G) - 1) \tag{3.1a}$$

where F is the force on each collagen IV segment, E is their elastic modulus at infinitesimal strain, A is the cross-sectional area of a collagen IV segment, B is a non-linearity fitting parameter, and e_G is the segment's Green strain. For supercoiled segments, the equation becomes

$$F = \frac{E_{SC} A_{SC}}{B} (\exp(B e_G) - 1) \tag{3.1b}$$

where E_{sc} is the elastic modulus of a supercoiled segment and A_{sc} is the cross-sectional area of a super-coiled segment. The values of the parameters are listed in Table 1. B can take on any non-negative value, and larger values give a more non-linear response. As there are no experimental stress-strain data available for the GBM, we chose a value that matched the non-linearity measured for the stress-strain response of the lens basement membrane [29]. The value of E_{sc} for the supercoiled segments was tested for two different cases: 1) keeping it the same as the value of the non-supercoiled segments, $E_{sc} = E$, and 2) doubling the original stiffness, $E_{sc} = 2E$. It is possible that the stiffness of the supercoiled protomers increases due to changes in bending energies, torsion and friction. The exact amount of a possible change is unknown, so we investigated how much of an effect would there be when the stiffness is doubled as an initial model.

The boundaries of the RVE were displaced equibiaxially in steps of 2% to 36% stretch. The third direction was compressed to preserve the volume of the RVE such that

$\lambda_x \lambda_y \lambda_z = 1$, where λ_i is the stretch ratio in direction *i*. At each step, the network nodes on the boundary were moved according to the RVE stretch, and the positions of the inner nodes were iterated (nodes could not break or re-form) until the stretch-dependent net force on each inner node reached zero. Bending and rotational forces were neglected. Once the inner nodes were equilibrated, the volume-averaged Cauchy stress tensor $\langle \sigma_{ij} \rangle$ was calculated from the local stresses σ_{ij} based on Chandran and Barocas (2006) [5],

$$\langle \sigma_{ij} \rangle = \frac{1}{V} \int \sigma_{ij} dV \tag{3.2}$$

Equation (3.2) can be re-written as,

$$\langle \sigma_{ij} \rangle = \frac{1}{V} \sum_{bc} x_i F_j \tag{3.3}$$

Where *bc* implies summation over all boundary nodes, x_i is the position of the nodes, and F_j is the force on that node.

3.3.4 Darcy permeability

Permeability of fibrous media is defined by Darcy's law as

$$v_i = -\frac{k_{ij}}{\mu} p_{,j} \tag{3.4}$$

where v_i is the fluid velocity, k_{ij} is the Darcy permeability tensor, μ is the fluid viscosity, and $p_{,j}$ is the mean pressure gradient. The equation can be re-written in terms of the drag forces to give

$$p_{,j} = -D_{ij} \mu v_i \tag{3.5}$$

where D_{ij} is the drag coefficient tensor which relates to the permeability by $k_{ij} = D_{ij}^{-1}$.

Permeability was calculated based on the method of Stylianopoulos *et al*. (2008) for creeping flow in periodic fiber arrays. In our model collagen IV network, we can consider each segment of the network to contribute as if it was part of a periodic network. Briefly, knowing the solid volume fraction, Φ, the length of the molecules, l, and their orientation, one can calculate the drag force parallel and perpendicular to the fibers. The drag coefficient tensor, d_{ij}, of a single molecule is calculated as

$$d_{ij} = R_{ik}^T C_{km} R_{mj} \tag{3.6}$$

where R_{ij} is the matrix of direction cosines, and C_{ij} is the diagonal coefficient matrix for drag. The components of C_{ij} were approximated using the solution of Drummond and Tahir (1984) for drag force in flow parallel to the periodic array,

$$C_{11} = \frac{4\pi l}{-\ln(\phi) - 1.476 + 2\phi - 0.5\phi^2 - O(\phi^4)} \tag{3.7}$$

and the solution of Sangani and Acrivos (1982) for drag force perpendicular to the periodic array,

$$C_{22} = C_{33} = \frac{8\pi l}{-\ln(\phi) - 1.476 + 2\phi - 1.774\phi^2 + 4.078\phi^3 - O(\phi^4)} \tag{3.8}$$

The drag coefficient tensor for the whole network, D_{ij}, is obtained by summing the drag of each molecule and normalizing by the total volume of the network, V_n,

$$D_{ij} = \frac{\sum d_{ij}}{V_n} \tag{3.9}$$

from which the permeability k_{ij} is calculated.

3.4 Results

We investigated the effect of supercoiling on the mechanical and permeability properties of collagen IV networks modeled as Voronoi networks. The model showed

that even small levels of supercoiling affect the mechanical properties of collagen IV networks but have minimal effect on network permeability.

3.4.1 Generated networks

Collagen IV networks (Fig 3), represented by Voronoi networks, had on average 711 segments with average length of 66 nm, and a solid volume fraction of 0.04. In comparison to our model (Fig 4a), the length distribution of a re-constituted collagen IV network is presented in Fig 4b (data from Yurchenco and Ruben, (1987)). The model and reconstituted collagen IV networks differ in their distribution of very short and very long segments. Imaging techniques may not be able to resolve the shortest fibers, and long segments can be missed if they are out of plane or leave the field of view. Upon supercoiling, average segment length decreased to 53 nm, a 20% decrease. Increasing the level of supercoiling further led to only a small decrease in average length of 6% (Table 2).

The five different supercoiling cases, for supercoil ratio p_m = 10%, 20%, 30%, 40%, 50%, gave increasing levels of total supercoiled material amounts (Table 2). The highest level of supercoiled material was 17% of the total material. The increased levels of supercoiling can be seen in Fig 5. Re-organizing the networks through supercoiling did not visibly affect the porosity or clustering of the network in the 2D projections.

3.4.2 Stress-stretch response

Networks were stretched equibiaxially up to 36% and treated as incompressible. An example of a network at the last step of deformation can be seen in Fig 3b. The average stress-stretch response of the original networks was non-linear with large initial deformation and stiffening at larger deformations (Fig 6a). At the final stretch ratio of 1.36, the average network stress was 6.5 MPa (N = 10). The average tangent modulus of the original network was 4.9 MPa at small deformations (<10% stretch), which is within the range for a basement membrane. At large deformations, the tangent modulus was 38.0 MPa.

The supercoiled networks were deformed under the same conditions. Fig 6b and Fig 6c show the average difference between the supercoiled networks (all five cases) and the original networks. Supercoiling increases the tangent modulus in all cases. The value of the supercoil modulus, E_{sc}, was tested for two different cases: E_{sc} = 0.5 GPa (same as non supercoiled segments, Fig 6b) and E_{sc} = 1 GPa (double that of non supercoiled segments, Fig 6c). For both cases, as the percent coiled material increased, the stress in the networks increased (comparing p_m = 10% to p_m = 50% cases), and the increase was bigger than when E_{sc} was doubled. Also, the differences become more pronounced at large deformations.

The relationship between the supercoil amount and the increase in stress was non-linear (Fig 7a). For the p_m = 10% case (low level of supercoiling), there was an increase of 5.3% from the original stress. For the p_m = 50% case (high level of supercoiling), the percent increase in stress at the last step was 38.7% when E_{sc} = 0.5 GPa and 52.2% when

E_{sc} = 1.0 GPa. It is clear from the plot that the effect of supercoil ratio was much larger than that of supercoil stiffness. The effect was also seen when the tangent modulus (i.e., the slope of the curves in Fig 6 at different stretches) was plotted vs. supercoiling ratio in Fig 7b and c. Figure 7b shows the increase in stress at small deformation and Fig 7c at large deformation At both small and large deformation, the effect of more supercoiling was much stronger than the effect of stiffer supercoils. For example, doubling the total amount of supercoils from 8% to 17% causes the percent increase in final stress to go from 11.3% to 38.7%. When E_{sc} was doubled, the percent increase in final stress only increases from 11.3% to 15.4%.

3.4.3 Darcy permeability

The average Darcy permeability of an undeformed original network was 0.98 nm^2, compared with the value of 1.2 nm^2 obtained by Bolton *et al.* (1998) and 1.5 nm^2 by Edwards *et al.* (1997) for the rat GBM by experimental methods. As the network stretched, there was a slight, supercoiling independent drop in permeability due to densification (Fig 8a). At small deformations, the most highly supercoiled network differs from the original network by only 7%. The difference becomes even smaller at large deformation, only 4%. In spite of the decreased permeability of the network, the permeability of the sample increased with stretch because the sample area increased and the thickness decreased (the latter increasing the pressure gradient for the same pressure drop). Fig 8b plots the permeability taking into account the changing cross-sectional area

and thickness by multiplying *k* by *A/h*. This effect is also nearly independent of supercoiling. Combining the earlier stretch-stress results (Fig 6) with the permeability results leads to a plot of permeability verses network stress (Fig 8c). If the networks were stretched at a given stress (e.g. by a set glomerular pressure), the permeability would increase as shown; the effect is slightly less pronounced in the more supercoiled models.

3.5 Discussion

We modeled supercoiling in collagen IV to investigate its effects on the mechanical and permeability properties of the networks. Our investigation revealed the following features of the simulated type IV collagen networks:

- Increasing the amount of supercoiling greatly increased the stiffness of the network and minimally decreases the permeability.
- Properties of the supercoils do not have as much of an effect as the total amount of supercoils.
- Effect of supercoiling on network stiffness and permeability became more pronounced at larger stresses.

The highly specific composition and organization of the GBM has been of interest for many years. It is speculated that the developmental switch between the $[\alpha1(IV)]_2\alpha2(IV)$ and $\alpha3(IV)\alpha4(IV)\alpha5(IV)$ collagen IV networks is in part based on the need of the GBM to transition from a more compliant structure to a stiffer one. In early

development, the compliant basement membrane facilitates the migration and organization of glomerular cells; while in the mature GBM, a stiffer network is needed to meet the increased mechanical demands. As the mechanical demands of the GBM increase, however, so do filtration demands. The balance between mechanical and hydraulic properties of the glomerular barrier has been addressed before in terms of the contribution of glomerular cells. Based on our model, supercoiling of collagen IV networks, which is higher in the α3(IV)α4(IV)α5(IV) networks, can help balance the mechanical and permeability demands by increasing network stiffness with minimal loss of permeability.

From a clinical perspective, the mechanical differences between the $[\alpha1(IV)]_2\alpha2(IV)$ and α3(IV)α4(IV)α5(IV) networks due to supercoiling highlight the importance of recognizing the loss of mechanical stability in the Alport GBM. Srinivasan et al. (2009) [46] investigated the changes in molecular stiffness due to mutations in the amino acid sequence of the collagen IV α chains. Their simulations revealed significant changes in the stress-strain and stiffness responses of the mutant collagens on the molecular level and that those changes are correlated to the clinical severity of the mutation. In our simulations on the network level, changing the stiffness of the supercoils, E_{sc}, did not have as much of an effect as the total amount of supercoils present. It is possible that the mutations that led to reduced stiffness influence clinical phenotypes in other ways; for example, by interfering with the formation of the collagen triple helix or supercoils, which in turn affects network mechanics and disease severity.

Promoting the formation of collagen IV supercoiling could affect the properties of the diseased GBM.

In general, increased lateral connectivity in a polymeric network causes increased stiffness, stability, reduced creep over time, and resistance to solvents/enzymes [34]. The effect of cross-linking on natural and synthetic polymers has been studied extensively for applications in generating tissue-equivalent material [13], consumer goods and textiles [7], cytoskeleton mechanics [38], and many others. For biological polymers, lateral connectivity and higher-order structures have been extensively studied in type I collagen [22,40], but less progress has been made on the formation and significance of supercoiling in type IV collagen. Supercoiling is not exclusive to type IV collagen; it is also found in type VI collagen [28], the compaction of DNA [35], and even tensile ropes [41]. Increasing lateral connectivity in synthetic or biological materials could be a great strategy for improving their mechanical properties without compromising their permeability properties.

We made several assumptions about the organization of collagen IV networks and the formation of supercoils. There is limited information on the interaction of the two collagen IV networks in the GBM and modeling limitations introduced some discrepancies between our model and real networks. The average segment length of our model was 66 nm, while that of the GBM has been reported to be 22 nm [18]. The number varies among basement membranes and is over 40 nm for the amniotic basement membrane [51]. Formation of supercoils was also simplified to include only two protomers although larger structures are observed biologically [52]. Even with these

differences, the model networks provided an adequate representation of the biological collagen IV networks and the possibility to explore the role of collagen IV network structures in determining GBM mechanical properties.

3.6 References

1. Abrahamson, D. Development of kidney glomerular endothelial cells and their role in basement membrane assembly. Organogenesis 275–287, 2009.

2. Barocas, V. H., K. D. Dorfman, and Y. Segal. A Model of Strain-Dependent Glomerular Basement Membrane Maintenance and its Potential Ramifications in Health and Disease. J. Biomech. Eng. 134:081006 1–8, 2012.

3. Bolton, G. R., W. M. Deen, and B. S. Daniels. Assessment of the charge selectivity of glomerular basement membrane using Ficoll sulfate. Am. J. Physiol. 274:F889–96, 1998.

4. Brenner, B. M., C. Baylis, and W. M. Deen. Transport of molecules across renal glomerular capillaries. Physiol. Rev. 56:502–34, 1976.

5. Chandran, P. L., and V. H. Barocas. Affine versus non-affine fibril kinematics in collagen networks: theoretical studies of network behavior. J. Biomech. Eng. 128:259–70, 2006.

6. Chandran, P. L., and V. H. Barocas. Deterministic material-based averaging theory model of collagen gel micromechanics. J. Biomech. Eng. 129:137–47, 2007.

7. Chen, X., F. Wudl, A. Mal, H. Shen, and S. Nutt. New thermally remendable highly cross-linked polymeric materials. Macromolecules 36:1802–1807, 2003.

8. Daniels, B., E. Hauser, W. Deen, and T. Hostetter. Glomerular basement membrane: in vitro studies of water and protein permeability. Am. J. Physiol. 262:, 1992.

9. Deen, W. M., M. J. Lazzara, and B. D. Myers. Structural determinants of glomerular permeability. Am. J. Physiol. Renal Physiol. 281:F579–96, 2001.

10. Drummond, J. E., and M. I. Tahir. Laminar viscous flow through regular arrays of parallel solid cylinders. Int. J. Multiph. Flow 10:515–540, 1984.

11. Edwards, a, B. S. Daniels, and W. M. Deen. Hindered transport of macromolecules in isolated glomeruli. II. Convection and pressure effects in basement membrane. Biophys. J. 72:214–22, 1997.

12. Endlich, N., and K. Endlich. The challenge and response of podocytes to glomerular hypertension. Semin. Nephrol. 32:327–41, 2012.

13. Girton, T., T. Oegema, and R. Tranquillo. Exploiting glycation to stiffen and strengthen tissue equivalents for tissue engineering. J. Biomed. Mater. Res. 46:87–92, 1999.

14. Gunwar, S., F. Ballester, M. E. Noelken, Y. Sado, Y. Ninomiya, and B. G. Hudson. Glomerular Basement Membrane. Identification of a novel disulfide- cross-linked netowrk of alpha3, alpha4, and alpha5 chains of type IV collagen and its implications for the pathogenesis of Alport syndrome. J. Biol. Chem. 273:8767–8775, 1998.

15. Gyoneva, L., Y. Segal, K. D. Dorfman, and V. H. Barocas. Mechanical response of wild-type and Alport murine lens capsules during osmotic swelling. Exp. Eye Res. 113:87–91, 2013.

16. Hadi, M. F., and V. H. Barocas. Microscale fiber network alignment affects macroscale failure behavior in simulated collagen tissue analogs. J. Biomech. Eng. 135:021026 1–8, 2013.

17. Haraldsson, B., J. Nystrom, and W. Deen. Properties of the glomerular barrier and mechanisms of proteinuria. Physiol. Rev. 451–487, 2008.

18. Hironaka, K., H. Makino, Y. Yamasaki, and Z. Ota. Renal basement membranes by ultrahigh resolution scanning electron microscopy. Kidney Int. 43:334–45, 1993.

19. Hofmann, H., T. Voss, K. Kühn, and J. Engel. Localization of flexible sites in thread-like molecules from electron micrographs:: Comparison of interstitial, basement membrane and intima collagens. J. Mol. Biol. 172:325–343, 1984.

20. Hudson, B. G., R. Kalluri, S. Gunwar, M. Weber, F. Ballester, J. K. Hudson, M. E. Noelken, M. Sarras, W. R. Richardson, J. Saus, and others. The pathogenesis of Alport syndrome involves type IV collagen molecules containing the alpha 3 (IV) chain: evidence from anti-GBM nephritis after renal transplantation. Kidney Int 42:179–187, 1992.

21. Hudson, B. G., S. T. Reeders, and K. Tryggvason. Type IV collagen: structure, gene organization, and role in human diseases. J. Biol. Chem. 268:26033–26036, 1993.

22. Hulmes, D. J. S. Building collagen molecules, fibrils, and suprafibrillar structures. J. Struct. Biol. 137:2–10, 2002.

23. Kalluri, R., C. F. Shield, P. Todd, B. G. Hudson, and E. G. Neilson. Isoform switching of type IV collagen is developmentally arrested in X-linked Alport syndrome leading to increased susceptibility of renal basement membranes to endoproteolysis. J. Clin. Invest. 99:2470–8, 1997.

24. Kashtan, C. E. Alport syndrome: an inherited disorder of renal, ocular, and cochlear basement membranes. Medicine (Baltimore). 78:338, 1999.

25. Kefalides, N. A., and B. Denduchisi. Structural Components of Epithelial and ENdothelial Basement Membranes. Biochemistry 8:4613–4621, 1969.

26. Khoshnoodi, J., V. Pedchenko, and B. G. Hudson. Mammalian collagen IV. Microsc. Res. Tech. 71:357–70, 2008.

27. Kim, K., Y. Kim, M. Gubler, M. Steffes, P. Lane, C. Kashtan, J. Crosson, and S. Mauer. Structural-functional relationships in Alport syndrome. J. Am. Soc. Nephrol. 5:1659–1668, 1995.

28. Knupp, C., and J. M. Squire. A new twist in the collagen story--the type VI segmented supercoil. EMBO J. 20:372–6, 2001.

29. Krag, S., and T. T. Andreassen. Mechanical properties of the human lens capsule. Prog. Retin. Eye Res. 22:749–767, 2003.

30. Kriz, W., M. Elger, P. Mundel, and K. V. Lemley. Structure-stabilizing forces in the glomerular tuft. J. Am. Soc. Nephrol. 5:1731–1739, 1995.

31. Kriz, W., M. Kretzler, a P. Provoost, and I. Shirato. Stability and leakiness: opposing challenges to the glomerulus. Kidney Int. 49:1570–4, 1996.

32. Kühn, K. Basement membrane (type IV) collagen. Matrix Biol. 14:439–45, 1995.

33. Lake, S. P., M. F. Hadi, V. K. Lai, and V. H. Barocas. Mechanics of a fiber network within a non-fibrillar matrix: model and comparison with collagen-agarose co-gels. Ann. Biomed. Eng. 40:2111–21, 2012.

34. Lee, K., and D. Mooney. Hydrogels for tissue engineering. Chem. Rev. 101:1869–1879, 2001.

35. Lyubchenko, Y., and L. Shlyakhtenko. Visualization of supercoiled DNA with atomic force microscopy in situ. Proc. Natl. Acad. Sci. U. S. A. 94:496–501, 1997.

36. Martinez-Hernandez, A., and P. Amenta. The basement membrane in pathology. Lab. Investig. 48:656, 1983.

37. Miner, J. H., and J. R. Sanes. Collagen IV alpha 3, alpha 4, and alpha 5 chains in rodent basal laminae: sequence, distribution, association with laminins, and developmental switches. J. Cell Biol. 127:879–91, 1994.

38. Mizuno, D., C. Tardin, C. F. Schmidt, and F. C. Mackintosh. Nonequilibrium mechanics of active cytoskeletal networks. Science 315:370–3, 2007.
Nachtrab, S., S. C. Kapfer, C. H. Arns, M. Madadi, K. Mecke, and G. E. Schröder-Turk. Morphology and linear-elastic moduli of random network solids. Adv. Mater. 23:2633–7, 2011.

39. Orgel, J., T. Irving, A. Miller, and T. Wess. Microfibrillar structure of type I collagen in situ. Proc. Natl. Acad. Sci. U. S. A. 103:9001–9005, 2006.

40. Pan, N., and D. Brookstein. Physical Properties of Twisted Structures . II . Industrial Yarns , Cords , and Ropes. J. Appl. Polym. Sci. 83:610–630, 2002.

41. Pavenstädt, H., W. Kriz, and M. Kretzler. Cell biology of the glomerular podocyte. Physiol. Rev. 83:253–307, 2003.

42. Ruben, G. C., and P. D. Yurchenco. High resolution platinum-carbon replication of freeze-dried basement membrane. Microsc. Res. Tech. 28:13–28, 1994.

43. Sakai, F., and W. Kriz. The structural relationship between mesangial cells and basement membrane of the renal glomerulus. Anat. Embryol. (Berl). 176:373–386, 1987.

44. Sangani, A. S., and A. Acrivos. Slow flow past periodic arrays of cylinders with application to heat transfer. Int. J. Multiph. Flow 8:193–206, 1982.

45. Srinivasan, M., S. G. M. Uzel, A. Gautieri, S. Keten, and M. J. Buehler. Alport syndrome mutations in type IV tropocollagen alter molecular structure and nanomechanical properties. J. Struct. Biol. 168:503–10, 2009.

46. Stylianopoulos, T., A. Yeckel, J. J. Derby, X.-J. Luo, M. S. Shephard, E. a Sander, and V. H. Barocas. Permeability calculations in three-dimensional isotropic and oriented fiber networks. Phys. Fluids (1994). 20:123601, 2008.

47. Suleiman, H., L. Zhang, R. Roth, J. E. Heuser, J. H. Miner, a. S. Shaw, and a. Dani. Nanoscale protein architecture of the kidney glomerular basement membrane. Elife 2:e01149–e01149, 2013.

48. Welling, L., M. Zupka, and D. Wellin. Mechanical properties of basement membrane. News Physiol. Sci. 10:30–35, 1995.

49. Wyss, H. M., J. M. Henderson, F. J. Byfield, L. a Bruggeman, Y. Ding, C. Huang, J. H. Suh, T. Franke, E. Mele, M. R. Pollak, J. H. Miner, P. a Janmey, D. a Weitz, and R. T. Miller. Biophysical properties of normal and diseased renal glomeruli. Am. J. Physiol. Cell Physiol. 300:C397–405, 2011.

50. Yurchenco, P. D., and G. C. Ruben. Basement membrane structure in situ: evidence for lateral associations in the type IV collagen network. J. Cell Biol. 105:2559–68, 1987.

51. Yurchenco, P. D., and G. C. Ruben. Type IV collagen lateral associations in the EHS tumor matrix. Comparison with amniotic and in vitro networks. Am. J. Pathol. 132:278–91, 1988.

52. Yurchenco, P., and J. Schittny. Molecular architecture of basement membranes. FASEB J. 4:1577–1590, 1990.

3.7 Tables

Table 3.1. Parameters for governing equation of collagen IV (Equation 3.1)

Parameters for collagen IV governing equation		
Parameter	**Value**	**Reference**
E	0.5 GPa	Srinivasan *et al.* (2009)[46]
E_{sc}	Case 1: 0.5 GPa Case 2: 1.0 GPa	
A	38.5 nm^2	radius from Deen *et al.* (2001)[9]
A_{sc}	154 nm^2	Double the radius
B	4	From fit (see text)

Table 3.2. Summary of generated networks. p_m is the percent of the midline length that was super-coiled (see Figure 2).

Summary of generated networks						
	Original network	**Super-coiled networks**				
		Supercoil ratio p_m (%)				
		10	**20**	**30**	**40**	**50**
Mean segment length (nm)	66	53	52	51	51	50
% total new coiled material	0	4	8	11	14	17

3.8 Figures

Figure 3.1. Structure and function of the kidneys at different scales. (a) The outer section of the kidneys contains millions of filtration centers. **(b)** In the filtration centers, called glomeruli, pre-filtered blood enters through the afferent arteriole, travels through the glomerular capillaries where water and small solutes can escape to the urinary space, and the filtered blood continues to the efferent arteriole. The walls of the glomerular capillaries are composed of the glomerular basement membrane (GBM). **(c)** Schematic of collagen IV networks in the GBM with the $[\alpha1(IV)]_2\alpha2(IV)$ (blue) and $\alpha3(IV)\alpha4(IV)\alpha5(IV)$ (red) networks occupying separate sides. Drawings of kidney and glomeruli were reproduced from Gray's anatomy public domain graphic plates.

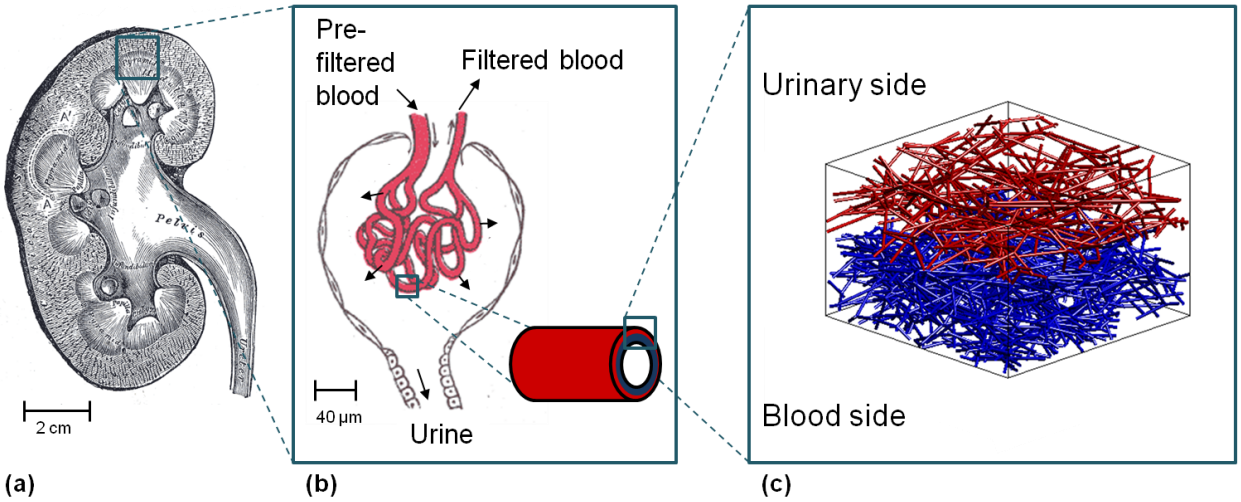

Figure 3.2. Schematic of original networks and how supercoils were formed. (a) Voronoi networks (in black) were used to represent native collagen IV networks. Each Voronoi edge is a segment of a collagen IV protomer (in red). The protomers in the original network are laterally connected and already have some supercoils (arrow). **(b)** New supercoils are created along the midline of the two segments at each node n_i with the smallest angle α_s; the length of the supercoil was varied as a percent (p_m) of the length of the midline (M). At the end of the supercoil, the combined segments branch off and return to their original nodes. The value of p_m was varied to generate different levels of supercoiling. In this example, p_m = 50% of the midline length.

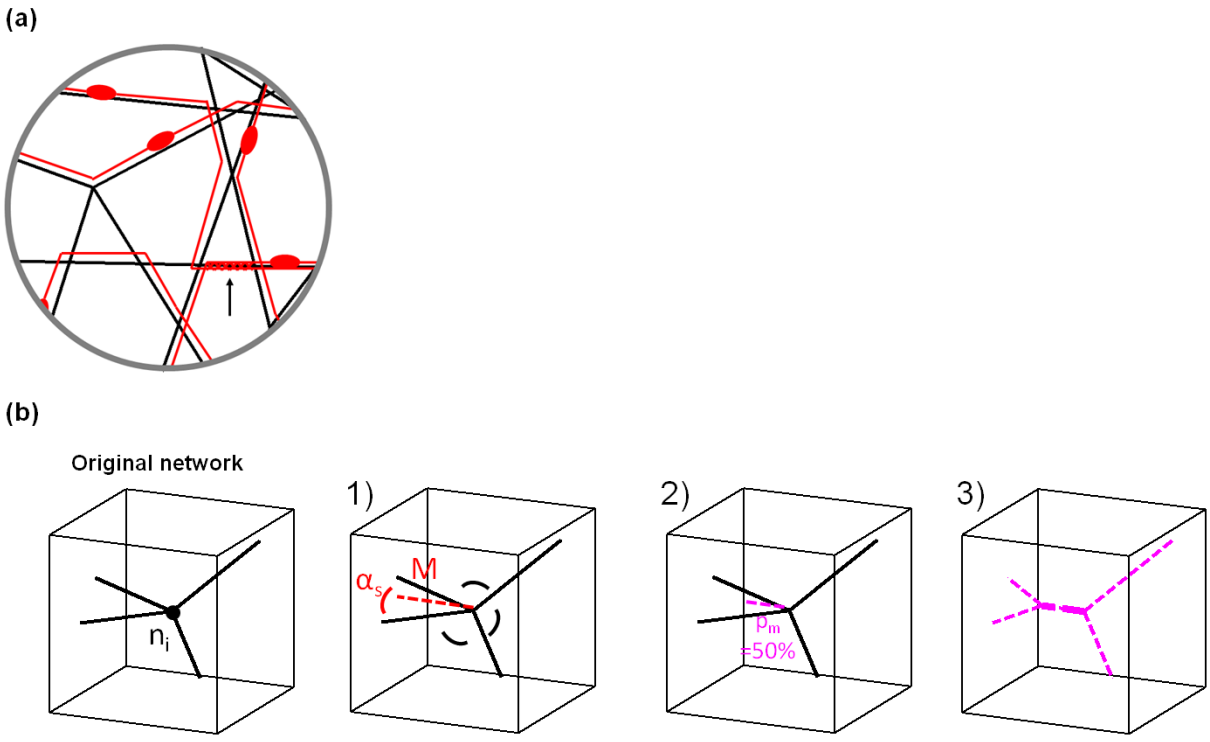

Figure 3.3. Example of a generated collagen IV network. **(a)** Before deformation, the network has dimensions of 560x560x175 nm. **(b)** The same network at the final step of deformation, 36% stretch. Networks were stretched equibiaxially and treated as incompressible.

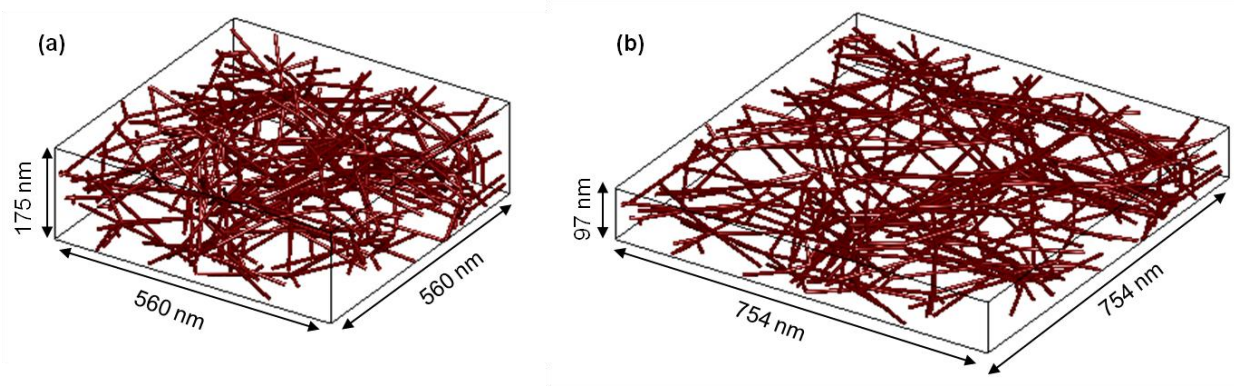

Figure 3.4. Distribution of collagen IV segment lengths. **(a)** In the Voronoi collagen IV network model, very short segments were common and there was also a small number of very long segments. **(b)** In a reconstituted collagen IV network (data from Yurchenco and Ruben (1987)[51]), average segment length was 44 nm and there was only a small number of very short segments and no long segments.

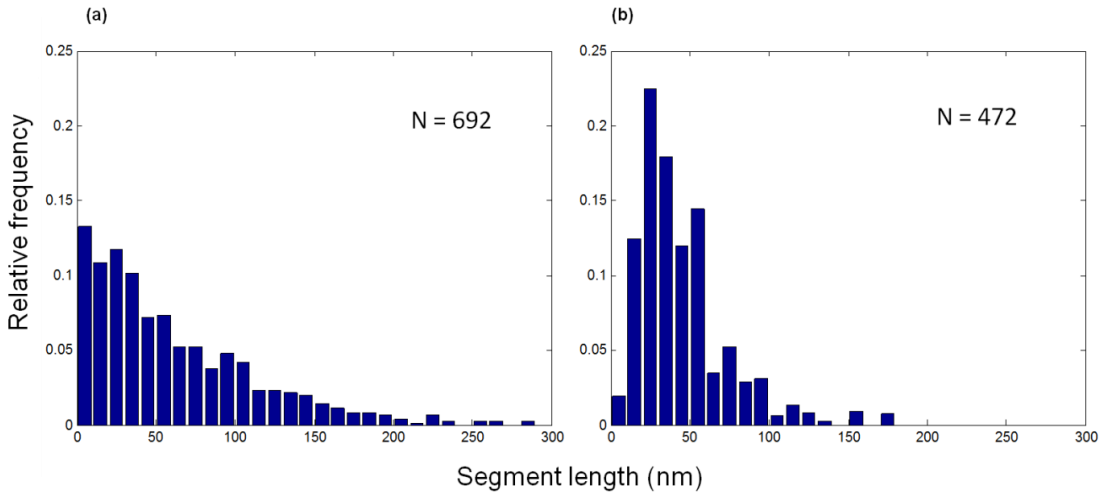

Figure 3.5. An example network at different levels of super-coiling. From top to bottom: original network, p_m = 10%, p_m = 30%, and p_m = 50%, where p_m is the percent of the midline length that was super-coiled (see Fig 2). Networks were projected into two dimensions for easier visualization.

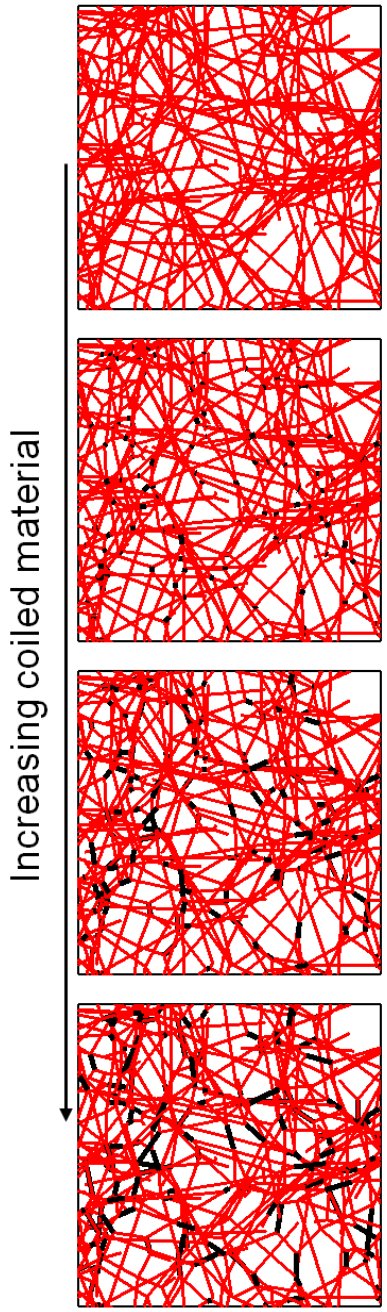

Figure 3.6. Effect of supercoiling on stress-stretch response of collagen IV networks. **(a)** Average stress-stretch response with 95% confidence interval of the original collagen IV networks (N=10), before new supercoils are introduced. **(b)** and **(c)** Difference in stress of supercoiled networks from original networks when the spring constant of supercoils is **(b)** E_{sc} = 0.5 GPa and **(c)** when E_{sc} = 1.0 GPa. Arrow indicates increasing value for the supercoil ratio p_m so the five curves go from p_m = 10% to p_m = 50%.

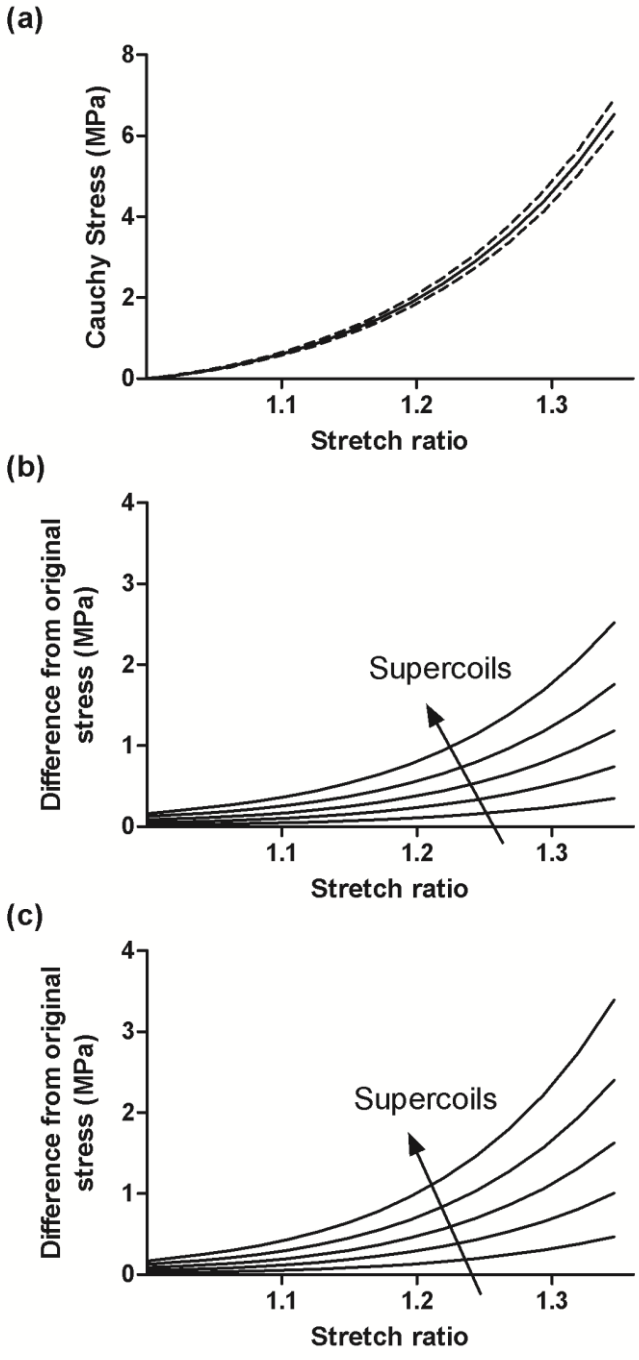

Figure 3.7. Percent increase of final stress and tangent modulus. (a) The increase in stress due to supercoiling for each stretched network at 36% stretch. Two cases are shown: when E_{sc} = 0.5 GPa (circles) and when E_{sc} = 1 GPa (triangles). **(b)** and **(c)** The increase in network tangent modulus due to supercoiling at **(b)** small deformation and **(c)** large deformation. The tangent modulus of the original network was 4.9 MPa at small deformation and 39.0 MPa at large deformation.

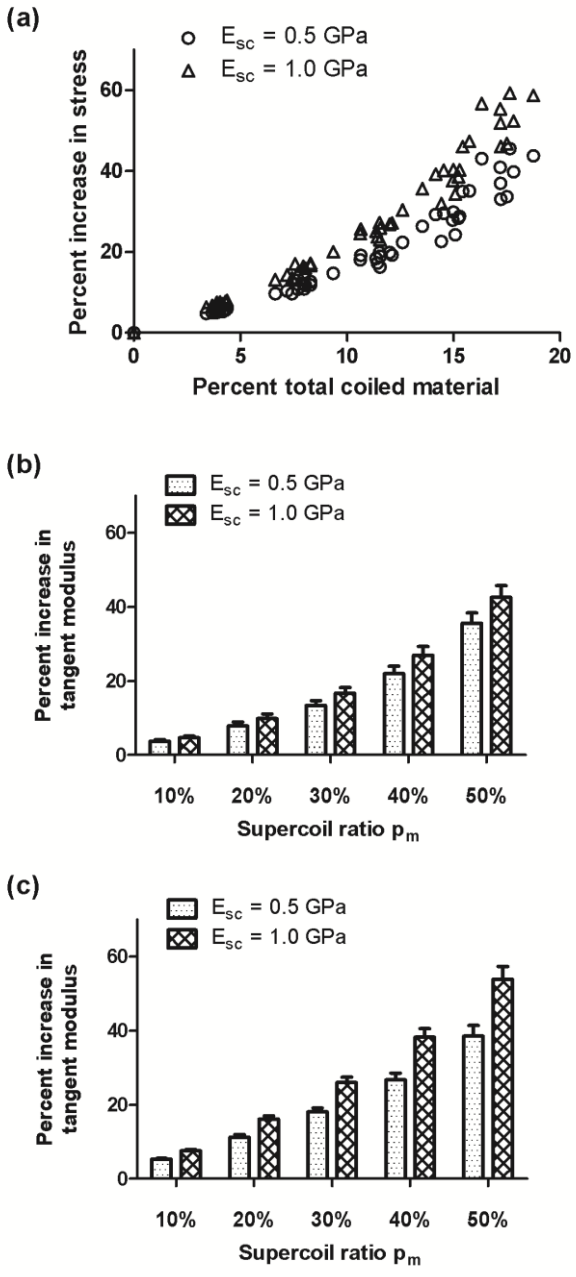

Figure 3.8. Darcy permeability and total permeability of model collagen IV networks. **(a)** As the network is stretched, there is a slight, supercoiling independent drop in permeability due to densification. **(b)** Total permeability is defined as permeability in which the changing cross-sectional area and thickness of the stretched network are accounted for. **(c)** Effect of supercoiling on the total permeability when a network is stretched at a given stress. Arrow indicates increasing value for the supercoil ratio p_m so the five solid black curves go from p_m = 10% to p_m = 50%. The red dashed line is the permeability of the original network, before supercoiling.

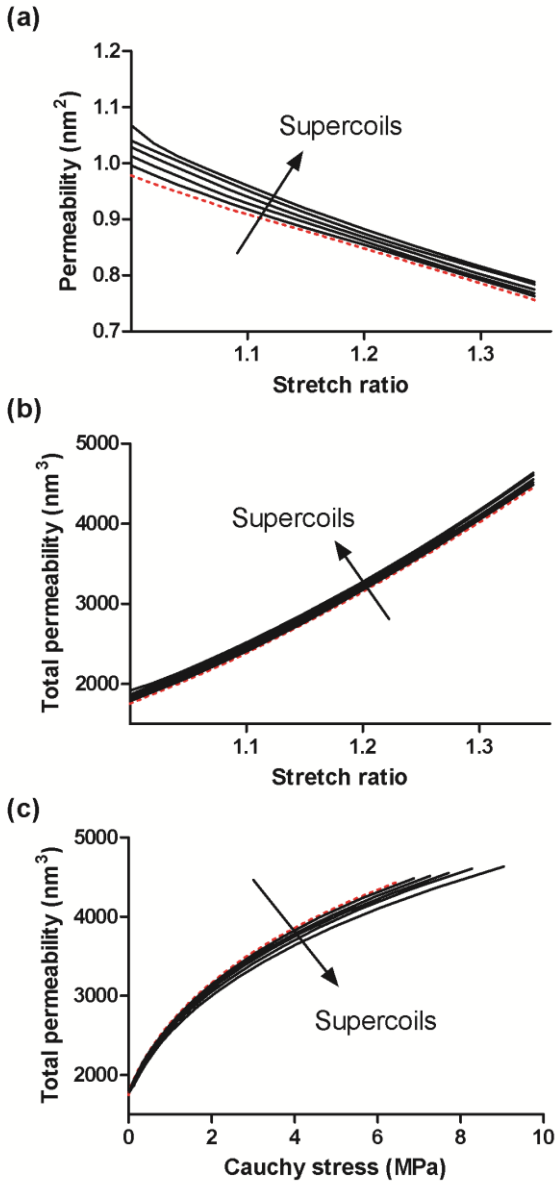

Chapter 4: Cell-Matrix Interaction during Strain-Dependent Remodeling of Simulated Collagen Networks

This chapter is part of the manuscript:

Gyoneva, L., Hovell, C. B., Pewowaruk, R. J., Dorfman, K. D., Segal, Y., & Barocas, V. H. (2016). Cell–matrix interaction during strain-dependent remodelling of simulated collagen networks. *Interface Focus*, *6*(1), 20150069.

4.1 Summary

The importance of tissue remodeling is widely accepted, but the mechanism by which the remodeling process occurs remains poorly understood. At the tissue scale, the concept of tensional homeostasis, in which there exists a target stress for a cell and remodeling functions to move the cell stress towards that target, is an important foundation for much theoretical work. We present here a theoretical model of a cell in parallel with a network to study what factors of the remodeling process help the cell move toward mechanical stability. The cell-network system was deformed and kept at constant stress. Remodeling was modeled by simulating strain-dependent degradation of collagen fibers and four different cases of collagen addition. The model did not lead to complete tensional homeostasis in the range of conditions studied, but it showed how different expressions for deposition and removal of collagen in a fiber network can

interact to modulate the cell's ability to shield itself from an imposed stress by remodeling the surroundings. This study also showed how delicate the balance between deposition and removal rates is and how sensitive the remodeling process is to small changes in the remodeling rules.

4.2 Introduction

Human tissues routinely change in response to environmental cues. The fundamental processes of growth and remodeling are necessary for the development of healthy tissues and for healing of tissues in the aftermath of injury or illness. Growth and remodeling can occur by a wide range of mechanisms, including cell proliferation [1] or death [2,3], pattern formation [4,5], and synthesis and/or degradation of extracellular matrix (ECM) [6–8]. This last process, cell-driven modification of the ECM, is of great interest because of the critical mechanical role played by ECM proteins, especially collagen, in many tissues [9]. The collagen network is often responsible for maintaining mechanical integrity and tensile strength of the tissue [7,10–15]. Although many other components (e.g. elastin [16], proteoglycans [17]) are also essential for tissue function, the ubiquity of collagens in load-bearing tissues makes them an attractive target for theoretical and experimental study. Collagen remodeling reflects the complex biomechanical relationship between the extracellular matrix and the cells that it supports.

In order to understand the remodeling of collagenous tissues, the underlying biochemical and biomechanical interactions between cells and the extracellular matrix

must be explored. Significant strides have been made through the use of theoretical models that treat the cells and extracellular matrix as a continuum (e.g. [18–22]). In particular, many models invoke the concept of tensional homeostasis, in which cells grow and/or modify the ECM to achieve a target stress. In its simplest form, the tensional homeostasis principle postulates that a target stress σ_o exists, and that some remodeling process occurs at a rate proportional to the deviation (σ-σ_o) between the cell stress and that of the target. Under most circumstances, the target stress is stable - actions taken in response to a deviation tend to reduce that deviation and return the system to the homeostatic stress state. Examples of this principle in models of tissue remodeling may be found throughout the biomechanics literature [23–26], and it is obviously related to the effect of matrix mechanics on cell behavior [27–29].

It remains unclear, however, how tensional homeostasis is achieved or what factors are necessary for tensional homeostasis. Tissue-level stress must be translated into tensions on the individual cells, and any tissue-level response must be driven by individual cellular responses. The details of these translations and the mechanisms by which the cell changes the collagen fibers around it are far from obvious, and the complex interactions between the different individual components of the tissue make exploration of these questions difficult. Experimental studies have shown, for example, that collagen synthesis is altered by the stretch [30] and the stiffness [31] of the substrate on/within which fibroblasts are cultured, and the enzymatic degradation of collagen is dependent on the collagen fiber tension [32]. The question at hand, then, is whether remodeling of the extracellular matrix through synthesis and degradation of collagen

fibers can lead a system to tensional homeostasis. We found that proportional remodeling alone did not lead to a fully stable system, but that it was an efficient method to move towards stability with minimal feedback required from the cell.

4.3 Methods

To study the stresses on a remodeling system of collagen networks and cells, we used an idealized model of a network and cell in parallel (Figure 1). In this configuration, the cell and network experience the same strain, and their individual stresses sum to the total stress of the system. The system was stretched by varied amounts and held at constant stress during remodeling. While the schematic in Figure 1 shows a single cell, the "Cell" component of the system is representative of the collection of cells in a tissue.

Figure 2 presents an overview of the multistep remodeling strategy. First, the fiber network was generated. Next, the system, consisting of a Neo-Hookean cell and a fiber network in parallel, was stretched to a specific stretch level, and the system stress was recorded. The system was then allowed to remodel by adding and/or removing material, and the strain was adjusted to maintain the same applied stress. The remodeling and adjusting steps were repeated until the entire system had equilibrated, and the final cell and network stresses and strains were recorded. Details on each step in the process are provided in the subsequent sections.

4.3.1 Collagen Network and Cell Models

Collagen networks were modeled as 3-dimensional networks of non-linear hyperelastic springs connected at freely-rotating nodes as we have done previously [33]. The networks were generated by randomly seeding points inside a unit cubic representative volume element (RVE), and Delaunay triangulation was used to connect polygonal elements from the seed points. The edges of the polygons became the collagen springs and the vertices became the nodes. Five random Delaunay networks were created with 714±48 (mean ± standard deviation) collagen fibers. The fibers were assigned an initial radius of 50 nm and stiffness of 79MPa [34]. The fiber volume fraction of the RVEs was 1.2±0.07%. The real size of the RVE was determined by a conversion factor between the computational and real domains that is defined in terms of the fiber radius. Setting the collagen fiber radius to 0.005 computational units (CU) gave us a desired collagen volume fraction of ~1%. Using the conversion 0.005 CU = 50 nm makes the real size of the RVE 10 μm.

The cell was modeled as an incompressible Neo-Hookean solid which was enforced by setting the Jacobian J = 1, preserving the volume. The Cauchy stress on the cell, $\sigma_{11,Cell}$, was then defined as

$$\sigma_{11,Cell} = C\left(\lambda_1^2 - \frac{1}{\lambda_1}\right) \tag{4.1}$$

where C is a constant defining the stiffness of the cell. Depending on the cell type, cell stiffness can vary widely, therefore, the value of C was defined with respect to the stiffness of the unremodeled collagen network to explore three different cases:

i. A cell twice as stiff as the network - could also represent a system of low-density matrix and many cells;

ii. A cell with the same stiffness as the network - cell and matrix have the same contribution in the system;

iii. A cell half as stiff as the network - could also represent a system of high-density matrix and few cells.

Network stiffness was defined as the slope of a secant line on the stress-strain curve from the origin to half-maximum stretch (before remodeling).

4.3.2 System Deformation

The cell-network system was stretched by different amounts (5, 10, 15, 20, 25, 30, 35, 40, 45, 50, 55, and 60% strain) before remodeling. The system was stretched uniaxially and incompressibility was enforced. Stretching was performed as previously described [35]. Briefly, the boundaries of the network were moved in steps of 1% in the direction of stretch, which we will call the 1-direction. In the other two directions, the stretch ratio was set to preserve the volume of the RVE ($\lambda_2 = \lambda_3 = 1/\sqrt{\lambda_1}$). The internal network nodes were iteratively moved until all were at mechanical equilibrium. The force, F, on each node was defined using an exponential relation such that the forces on

fibers in tension are much larger than forces on fibers in compression with a computationally advantageous continuous force function.

$$F = \frac{E_{fiber} A_{fiber}}{B} (\exp(B\varepsilon_G) - 1) \tag{4.2}$$

where E_{fiber} is the collagen fiber modulus at infinitesimal strain, A_{fiber} is the cross-sectional area of the fiber, ε_G is the Green strain of the fiber, and B is a non-linearity parameter which was set to 1.2 based on previously fitted data from collagen gels [36].

The volume-averaged stress on the equilibrated network, $\langle \sigma_{ij} \rangle$, was calculated as

$$\langle \sigma_{ij} \rangle = \frac{1}{V} \sum_{bc} x_i f_j - p\delta_{ij} \tag{4.3}$$

where $\langle \sigma_{ij} \rangle$ is the volume-averaged Cauchy stress tensor, V is the current volume of the RVE, bc indicates discrete summation over the boundary nodes, x_i is the position of a node on the boundary, f_j is the force on that node, p is the hydrostatic pressure term for incompressible materials, and δ_{ij} is the identity. The value of p was obtained by solving for the stresses on the free surfaces. For full derivation, refer to [37].

4.3.3 Network Remodeling

Collagen network remodeling was represented in the model by increasing or decreasing the radius of the cylindrical collagen fibers based on addition and removal rates, respectively. The radius-based approach does not allow creation of new fibers or the complete removal of a fiber.

4.3.3.1 Collagen removal

The rate of fiber removal, $\left(\frac{dr}{dt}\right)_{removal}$, was related to the stretch of the fibers such that more highly stretched fibers were more protected from degradation, following the observations of [32].

$$\left(\frac{dr}{dt}\right)_{removal} = -k_1 \frac{r}{r + r_{small}} \exp(-k_2(\lambda_{fiber} - 1)) \tag{4.4}$$

where λ_{fiber} is the stretch ratio of the fiber, r is the fiber radius, and r_{small} is a value representing a small radius, chosen here to be 10% of the original value. The factor $\frac{r}{r + r_{small}}$ ensures that the fiber radius will not become negative during the course of remodeling. When $r >> r_{small}$, the ratio approaches unity and (dr/dt) becomes r-independent, leading to linear decrease in the case of constant stretch. When $r << r_{small}$, however, the ratio approaches r/r_{small}, and the radius decays exponentially to zero. The scaling constant k_1 has units of nm/sec, and k_2 is a dimensionless constant determining

the amount of exponential dependence on stretch. The negative exponential form of the governing equation gives more stretched fibers (larger λ_{fiber}) lower degradation rates.

The values of the constants k_1 and k_2 were obtained previously by fitting the experimental data of [32]. Hadi et al. [34] found k_1 to be 1.05×10^{-3} nm/sec and k_2 to be 0.83. The obtained values are for a specific *in vitro* case of collagen degradation by bacterial collagenase. To look at a more general case of collagen remodeling, we write the equation in dimensionless form. If we let the characteristic time scale to be $\tau = R / k_1$, where R is the initial value of the fiber radius (50nm), then the scaling factor for the removal rate can be re-written as

$$-k_1 \frac{r}{r + r_{small}} = -\tau \frac{r/R}{r/R + r_{small}/R}$$

If we further define the dimensionless constants $\rho \equiv r/R$, $\rho_o \equiv r_{small}/R$, and $\zeta = t/\tau$, then the dimensionless rate of removal becomes

$$\left(\frac{d\rho}{d\zeta}\right)_{removal} = \frac{dr}{dt}\frac{d\rho}{dr}\frac{dt}{d\zeta} = -\frac{\rho}{\rho + \rho_o}\exp(-k_2(\lambda_{fiber} - 1)) \tag{4.5}$$

This degradation expression was used in all simulations.

4.3.3.2 Collagen addition

A vast array of options exists for modeling fiber deposition. In this paper, we begin with a general form based on the principle that two factors can influence deposition: (1) the cell may tend to deposit more material when it is more stretched (note that because of the elastic constitutive model for the cell, this assumption is equivalent to a cell-stress-based model), and/or (2) the cell may tend to align and thus deposit new matrix in the direction in which the current fibers are already aligned (via contact guidance). Assuming separability of the two factors, we write the general form

$$\left(\frac{dr}{dt}\right)_{addition} = k_3 f(\textit{cell stretch}) g(\textit{fiber orientation}) \tag{4.7}$$

where k_3 is a constant.

For the cell stretch effect, we postulate an exponential factor such that

$$f(\lambda_{cell}) = \exp(k_4(\lambda_{cell} - 1)) \tag{4.8}$$

where λ_{cell} is the cell stretch ratio and is equal to the matrix stretch under the assumptions of Figure 1. The constant k_4 captures the sensitivity to stretch. A large value of k_4 indicates a very stretch-sensitive cell, and $k_4 = 0$ indicates stretch-independent deposition. For the fiber orientation effect, we scaled the deposition rate according to a von Mises distribution,

$$g(\theta) = \frac{\exp(\kappa \cos(2(\theta - \theta_o)))}{I_0(\kappa)} \tag{4.9}$$

where θ is the orientation of a fiber to be deposited, θ_o is the average orientation of the existing matrix, $I_o(\kappa)$ is the modified Bessel function of order zero, and κ is a shape parameter that indicates stronger alignment for larger κ. If κ=0, $g(\theta)=1$ for all θ, and all directions have equal strength; as κ goes to infinity, g approaches a delta function at $\theta=\theta_o$. Because of the uniaxial stretch in this study, the direction of θ was always the 1 direction. The normalization factor of π normally present in the von Mises distribution has been absorbed into the constant k_3. This model does not account for the degree of orientation in the matrix, only the direction; a strongly-aligned network is no more likely to induce aligned deposition than a weakly-aligned one.

Combining these expressions, the total deposition rate is given by

$$\left(\frac{dr}{dt}\right)_{addition} = k_3 \exp(k_4(\lambda_{cell} - 1)) \frac{\exp(\kappa \cos(2(\theta - \theta_o)))}{I_0(\kappa)} \tag{4.10}$$

or, in the dimensionless form following Eqn 4.5,

$$\left(\frac{d\rho}{d\zeta}\right)_{addition} = \alpha \exp(k_4(\lambda_{cell} - 1)) \frac{\exp(\kappa \cos(2(\theta - \theta_o)))}{I_0(\kappa)} \tag{4.11}$$

where $\alpha = k_3/k_1$ is a dimensionless quantity representing the rate of deposition relative to removal.

In the current study, we considered four cases (Table 1):

1. Stretch-independent, isotropic deposition ($k_4 = \kappa = 0$)

2. Stretch-dependent, isotropic deposition ($k_4 \neq 0$, $\kappa = 0$)

3. Stretch-independent, anisotropic deposition ($k_4 = 0$, $\kappa \neq 0$)

4. Stretch-dependent, anisotropic deposition ($k_4 \neq 0$, $\kappa \neq 0$)

The dimensionless parameters were varied to cover a broad range of possibilities. The values used in each case are presented in Table 1.

The net rate change of radius based on the above expressions was

$$\left(\frac{d\rho}{d\zeta}\right)_{net} = \left(\frac{d\rho}{d\zeta}\right)_{addition} + \left(\frac{d\rho}{d\zeta}\right)_{removal} \tag{4.12}$$

and the new fiber radius was calculated by a forward Euler step,

$$r_{\zeta+1} = r_{\zeta} + \left(\frac{d\rho}{d\zeta}\right)_{net} r_{\zeta} \tag{4.13}$$

4.3.4 Remodeling at constant stress

When the radius for each fiber was updated, the stress in the system changed. To return the system to the applied stress, the strain was adjusted (either by contracting the

system or by stretching it further). The adjustment was done by iterating the strain until the new stress was within a specified tolerance of the applied stress ($\pm 1 \times 10^{-5}$ kPa). Once the applied stress had been achieved, another remodeling time step was taken, and the rates of removal and addition were calculated for each fiber again. A total of 3000 remodeling iterations were performed (each iteration representing 20 seconds remodeling time), enough for the cell and network stresses to stabilize. The equilibrium cell and total system stresses were plotted versus each other as shown in Figure 3.

4.4 Results

The deformation steps before remodeling starts were the same for all cases. Cellular and network stiffness varied in the range of 150 kPa to 300 kPa before remodeling. For the case of a cell with half the stiffness of the network, the cell stiffness range was between 75 kPa and 150 kPa. For the stiff cell cases, cell stiffness was over 300 kPa.

4.4.1 Case 1 ($k_4 = \kappa = 0$)

The rate of collagen removal in this case, as in all others, was based on the stretch of the fibers. The rate of addition was set to the dimensionless constant α. The value of α had an upper limit of 1, for which the rate of addition was equal to the rate of removal at zero stretch, which caused the network to deposit collagen continuously and prevented it

from equilibrating (Figure 4). On the other hand, a low α value of 0.8 led to more removal than addition. Net loss of collagen is reasonable, as would be expected in a tensional homeostasis model if the cell stress were below the target stress, but for this study, we considered systems that would lead to net collagen deposition. Therefore, the values of α were selected to be 0.9, 0.92, and 0.95.

At α = 0.9 and a medium stretch of 20%, the system maintained a constant stress of 171 kPa during remodeling as the cell and network stresses moved in opposing directions until both reached equilibrium (Figure 5). The stress on the network increased during remodeling, prompted by an increase in the collagen volume fraction. The stress on the cell, in complement, decreased as the system stretch ratio decreased to maintain a constant total system stress. The volume fraction increase was a result of the net deposition of new material. The mean fiber radius in the network increased - all fibers started with a radius of 50 nm and during remodeling some fiber radii became much bigger (Figure 6). The results presented with these parameters are representative of the qualitative behavior seen for other values of α and for other stretches. The value of α had a significant impact on the equilibrium stresses (Figure 7). An increase in α caused an increase in the collagen volume fraction, as expected, and it also corresponded to a decrease in the fraction of the total stress that was borne by the cell. For all three values of α, however, the cells never reached a constant stress value independent of the total stress. For example, in the low-slope (high-stress) region of the plot in Figure 7b, a 16.6% increase in total stress led to a 5.4% increase in cell stress when α = 0.9. When α =

0.95, increasing the total stress by the same amount increased the cell equilibrium stress by 5.5%.

To check whether tensional homeostasis can be achieved by a cell of different stiffness, we varied the stiffness of the cell in relation to the collagen network, making it twice and half as stiff as the network (Figure 8). The stiffer cell saw an increase in cell and total stress, as well as the fraction of the stress carried by the cell. With the softer cell, the cell was responsible for a smaller fraction of the total stress. Still, in all cases of cell stiffness, the cell stress became less sensitive to total stress but did not reach a clear plateau. At the higher stress, a 17.5% increase in total stress led to a 5.3% increase in cell stress for a soft cell. For a stiff cell, a 15.8% increase in total stress led to a 4.7% increase in cell stress.

4.4.2 Case 2 ($k_4 \neq 0$, $\kappa = 0$)

In Case 2, the cell was given more control of the remodeling process by allowing it to deposit more collagen the more stretched it became. Similar to Case 1, the cell stress decreased with remodeling while the network stress increased (Figure 9). The plots in Figure 9 are again for $\alpha = 0.9$, but now if we look at two different system strains, 5% and 35%, we see that the stresses equilibrate much faster at higher strain. The larger the initial system deformation, the faster the cell responded because of the cell-stretch-dependent deposition term. The cell bore only about 5% of total system stress. Compared to Case 1, the final cell stress was decreased in half.

4.4.3 Case 3 ($k_4 = 0$, $\kappa \neq 0$)

In Case 3, the cell was allowed to remodel the network by preferentially depositing collagen fibers in the direction of stretch but without changing the total deposition rate with stretch. The level of anisotropic deposition was controlled by the parameter κ. The values selected for κ were 0.02,0.04,0.06, and 0.08. The values were chosen again to ensure that the system would reach equilibrium, as larger values for κ caused a dramatic increase in the collagen volume fraction.

The representative example in Figure 10a is with $\alpha = 0.9$, $\kappa = 0.2$, and 20% initial strain. Similar to Cases 1 and 2, the cell stress decreased and network stress increased while the total system stress remained constant. Increasing κ increased the collagen volume fraction and decreased the system stretch ratio, similar to the effect of α. The fraction of the cell stress out of total system stress also decreased with increasing κ but the cell stress did not plateau for any of the κ values. For $\kappa = 0.02$, at high stress, changing the total stress by 16.6%, increased the equilibrium cell stress by 5.3%. For $\kappa = 0.08$, the cell stress increased by 4.8% for the same total stress increase as above. How the new fibers were deposited can be seen in Figure 11. The fibers oriented in the 1-direction have a larger radius, though the effect of the increasing κ is not immediately obvious.

4.4.4 Case 4 ($k_4 \neq 0$, $\kappa \neq 0$)

In Case 4, the cell was given the most control over the remodeling process, allowing it to deposit more collagen the more stretched it became and at the same time to deposit fibers in a preferred direction. The representative plot in Figure 12 is for $\alpha = 0.9$, $\kappa = 0.02$, and 20% initial stretch where the system equilibrates quickly. Increasing κ led to a small increase in the collagen volume fraction and a small decrease in the system stretch ratio. With the larger $\kappa = 0.08$, the cell had a smaller fraction of the total stress, compared to smaller $\kappa = 0.02$. The value of deposition at preferred orientation had a smaller effect on the remodeling process than the initial stretch (Figure 13). The collagen fiber radius visibly increased when the initial stretch was changed from 5% to 35%, but the differences between Cases 2 and 4 were harder to see. Overall, Case 4 had the smallest fraction of the cell stress out of the total system stress (Figure 14). At high stresses, a 16.6% increase in total stress led to a 4.6% increase in cell stress, when $\kappa = 0.02$.

4.5 Discussion

Tensional homeostasis has been a subject of interest for many years now, though experimental limitations have left many open questions [23]. The theoretical model presented here serves as a tool to explore how a cell can control its environment by remodeling its extracellular matrix. To model turnover of collagen fiber networks, we modeled the rate of collagen removal as dependent on the stretch of the fibers and we

modeled the rate of addition in four different ways: 1) constant rate of addition; 2) a more stretched cell deposits more collagen material; 3) collagen material is deposited in the direction of stretch; and 4) the cell is sensitive to both stretch and fiber orientation (combination of cases 2 and 3). The model allowed us to investigate how a cell might control its mechanical environment in an effort to achieve tensional homeostasis.

For all remodeling cases, the equilibrium cell stress approached a plateau but it never fully reached a zero slope. In general, increasing the rate of collagen addition led to a decrease in the fraction of the total system stress carried by the cell and an increase in the contraction of the system, moving it closer to its original configuration. The system was very sensitive to even small changes in α and could be induced into entering a non-converging state for larger values of α. Changing the stiffness of the cell in relation to the network changed the amount of cellular contribution to the system stress - a stiffer cell held a higher fraction of the total stress than a softer cell. The system was also very sensitive to changes in the initial stretch especially in cases where the cell could sense stretch and adjust its collagen deposition accordingly. The values used for κ in Cases 3 and 4 had to be kept very low, because, as with large α's, the system did not reach a stable equilibrium for larger κ's. An increase in κ led to an increase in the amount of added collagen and the contraction of the system. Even for very small κ's, the system showed some improvement in reducing the cell stress fraction from the total stress compared to Case 1. The combination of allowing the cell to both sense stretch and align the collagen matrix resulted in the biggest reduction to cell stress compared to Case 1.

The trends observed when α and κ were large are best explained by recognizing that there is a minimum deposition rate and a maximum removal rate. For the isotropic cases (1 and 2), the dimensionless deposition rate must be at least α, and for the anisotropic cases, the dimensionless deposition rate for fibers oriented in the 1 direction goes as $\alpha(1 + \kappa)$ for small κ values. Because the sample is in tension, the minimum fiber stretch for most of the fibers is 1, and thus the minimum dimensionless removal rate is 1. Thus, if $\alpha > 1$ or if $\alpha(1 + \kappa) > 1$, then the deposition rate will always exceed the removal rate, and the fiber will thicken without bound.

Based on Figure 14, it appears that very different modes of operation for the addition process can all be adequate for bringing the cell close to tensional homeostasis. The differences between Case 1and Case 4 were not great in terms of the final slope of the curves, but they were very different in the value of the cell stress - in Case 4, the cell stress was 3 times smaller. When the cell had more control over its remodeling environment, it was not only able to further reduce the stresses acting on it, but it was also able to reach remodeling equilibrium quicker. These factors could be important in protecting the cell from entering a pathological state, such as stiffening of the cell (as seen in tumor cells) [29].

There are certain assumptions and simplifications in our model that could merit further discussion. The cell was allowed to change only the collagenous matrix and not its internal structure; that is, the cell component was modeled as a homogeneous incompressible Neo-Hookean solid with constant properties, whereas it is known that cell stiffness can in fact change in response to many factors, including the substrate stiffness

[41,42]. Furthermore, in the current model, the cell was treated as entirely passive, with no active (contractile) contribution to the mechanical environment. New collagen fibers were deposited pre-stressed at a level equal to that of the already existing fibers. Finally, the remodeling feedback controls were based on a single proportional feedback rule. All of these assumptions are examined further below.

Our model did not take into consideration the internal structure of the cell, nor accounted for the many changes that can happen to it during remodeling. The exact molecular pathways of how mechanical stresses and strains are sensed by the cell and translated into a response are still not well understood. In this model, the cell was considered only as an elastic solid at three different stiffness levels. It is known that cells can change their stiffness with changes in stretch by reorganizing cytoskeleton components [43]. It is possible that giving the cell another level of control would change the equilibrium stresses. Mizutani et al. [43] found experimentally that cells returned to their pre-deformation stress levels in just 2 hours, indicating that the cells can maintain an equilibrium stress level without the remodeling of the extracellular matrix. However, remodeling of the cytoskeleton and the extracellular matrix seem to occur on different time scales - with internal cellular remodeling occurring very rapidly compared to slower turnover of collagen fibers.

Of course, remodeling is a very complex process involving a multitude of chemical and mechanical pathways. Cells can release growth factors, hormones, and enzymes, produce matrix, and change cell alignment. The degradation of the collagen matrix can also be regulated by a number of factors, not just strain-dependent protection.

Our model focused on the mechanical aspects of remodeling and how it applies to the local microenvironment of a cell. The different types of pathways available to a cell give it the ability to respond to different types of stimuli. Though mechanical and chemical stimuli cannot be fully separated, it is still informative to look at the mechanical response of a cell to mechanical cues. The mechanical responses that we covered have been appreciated rather recently and also contain some unanswered questions, for example, how new collagens are integrated into the matrix. There is yet no experimental evidence on the stress state of newly deposited collagen, but for the cells to maintain a constant stress during remodeling, collagens would need to be deposited pre-stressed. In our work, new collagens were added by increasing the radius of already existing collagen fibers, which inherently meant that new collagens were pre-stressed.

The lack of complete tensional homeostasis in any of the models is reminiscent of the offset that exists in a proportional control system. Although the system in the current study is considerably more complex than a simple linear controller, the similarities are informative. The deposition rate is constant, so equilibrium for a given load must occur when the fiber stretch is such that the deposition rate matches the removal rate. This stretch, however, is an equilibrium stretch, not the set point stretch (i.e., the stretch at which no control action is taken, which in the current model would be zero stretch). The equilibrium is offset from the set point just as in a classical proportional control problem, and, as in the classical case, the offset is a function of the operating conditions, which in our system means that the equilibrium cell stretch must be a function of the imposed stress. A set point could be achieved through an adaptive

control algorithm or through the addition of integral control, which may well exist for this purpose inside the cell and which would allow the deposition rate to depend not only on the stress but on the accumulation of some stress marker over time. The possible role of integral control within the cell is a topic of considerable study [44–47], and it would be interesting to explore it in the context of remodeling.

In conclusion, the results presented in this work show that, at least in some cases, a leveling-off similar to tensional homeostasis can arise naturally from the balance of deposition and removal without requiring that the cell "knows" what the target stress is. Most importantly as relates to this issue, in our Case 1, a tensional-homeostasis-like response (defined as small changes in cell stress over a wide range of tissue stresses because of remodeling) was achieved without any presumed sensory mechanisms in the cell. Even in the more complex models of our other cases, the remodeling was not driven by a desire to achieve a target stress. Rather, the target stress emerges from the various processes. We thus conclude that tensional homeostasis is not an end unto itself but a consequence of multiple cell and ECM processes in balance.

4.6 References

1. Goss, R. J. 1966 Hypertrophy versus Hyperplasia. Science (80-.). 153, 1615–1620. (doi:10.1126/science.153.3744.1615)

2. Polunovsky, V. A., Chen, B., Henke, C., Snover, D., Wendt, C., Ingbar, D. H. & Bitterman, P. B. 1993 Role of Mesenchymal Cell Death in Lung Remodeling after Injury. J. Clin. Invest. 92, 388–397. (doi:10.1172/JCI116578)

3. Takemura, G. & Fujiwara, H. 2004 Role of apoptosis in remodeling after myocardial infarction. Pharmacol. Ther. 104, 1–16. (doi:10.1016/j.pharmthera.2004.07.005)

4. Wolpert, L. 1978 Pattern Formation in Biological Development. Sci. Am. 239, 154–164. (doi:10.1038/scientificamerican1078-154)

5. Peirce, S. M. & Skalak, T. C. 2003 Microvascular remodeling: a complex continuum spanning angiogenesis to arteriogenesis. Microcirculation 10, 99–111. (doi:10.1038/sj.mn.7800172)

6. Nissen, R., Cardinale, G. J. & Udenfriendt, S. 1978 Increased turnover of arterial collagen in hypertensive rats. Proc. Natl. Acad. Sci. U. S. A. 75, 451–453.

7. Humphrey, J. D. 1999 Remodeling of a Collagenous Tissue at Fixed Lengths. J. Biomech. Eng. 121, 591–597. (doi:10.1115/1.2800858)

8. Yoshida, K., Reeves, C., Vink, J., Kitajewski, J., Wapner, R., Jiang, H., Cremers, S. & Myers, K. 2014 Cervical collagen network remodeling in normal pregnancy and disrupted parturition in Antxr2 deficient mice. J. Biomech. Eng. 136, 021017. (doi:10.1115/1.4026423)

9. Fung, Y. 1993 Biomechanics: Mechanical Properties of Living Tissues. 2nd edn. Springer-Verlag.

10. Elliott, D. M., Robinson, P. S., Gimbel, J. a., Sarver, J. J., Abboud, J. a., Iozzo, R. V. & Soslowsky, L. J. 2003 Effect of Altered Matrix Proteins on Quasilinear Viscoelastic Properties in Transgenic Mouse Tail Tendons. Ann. Biomed. Eng. 31, 599–605. (doi:10.1114/1.1567282)

11. Quapp, K. M. & Weiss, J. A. 1998 Material Characterization of Human Medial Collateral Ligament. J. Biomech. Eng. 120, 757–763. (doi:10.1115/1.2834890)

12. Gupta, H. S., Seto, J., Krauss, S., Boesecke, P. & Screen, H. R. C. 2010 In situ multi-level analysis of viscoelastic deformation mechanisms in tendon collagen. J. Struct. Biol. 169, 183–91. (doi:10.1016/j.jsb.2009.10.002)

13. Gyoneva, L., Segal, Y., Dorfman, K. D. & Barocas, V. H. 2013 Mechanical response of wild-type and Alport murine lens capsules during osmotic swelling. Exp. Eye Res. 113, 87–91. (doi:10.1016/j.exer.2013.05.008)

14. Coudrillier, B., Pijanka, J., Jefferys, J., Sorensen, T., Quigley, H. a, Boote, C. & Nguyen, T. D. 2015 Collagen structure and mechanical properties of the human sclera: analysis for the effects of age. J. Biomech. Eng. 137, 041006. (doi:10.1115/1.4029430)

15. Zeinali-Davarani, S., Wang, Y., Chow, M.-J., Turcotte, R. & Zhang, Y. 2015 Contribution of collagen fiber undulation to regional biomechanical properties along porcine thoracic aorta. J. Biomech. Eng. 137, 051001. (doi:10.1115/1.4029637)

16. Bellini, C., Ferruzzi, J., Roccabianca, S., DiMartino, E. S. & Humphrey, J. D. 2014 A Microstructurally Motivated Model of Arterial Wall Mechanics with Mechanibiological Implications. Ann. Biomed. Eng. 42, 488–502. (doi:10.1007/s10439-013-0928-x.A)

17. Screen, H. R. C., Shelton, J. C., Chhaya, V. H., Kayser, M. V, Bader, D. L. & Lee, D. A. 2005 The influence of noncollagenous matrix components on the micromechanical environment of tendon fascicles. Ann. Biomed. Eng. 33, 1090–9. (doi:10.1007/s10439-005-5777-9)

18. Ramasubramanian, A. & Taber, L. A. 2008 Computational Modeling of Morphogenesis Regulated by Mechanical Feedback. Biomech. Model. Mechanobiol. 7, 77–91. (doi:10.1007/s10237-007-0077-y.Computational)

19. Gasser, T. C., Schulze-Bauer, C. A. J. & Holzapfel, G. A. 2002 A Three-dimensional Finite Element Model for Arterial Clamping. J. Biomech. Eng. 124, 355–363. (doi:10.1115/1.1485284)

20. Fata, B., Zhang, W., Amini, R. & Sacks, M. S. 2014 Insights into regional adaptations in the growing pulmonary artery using a meso-scale structural model: effects of ascending aorta impingement. J. Biomech. Eng. 136, 021009. (doi:10.1115/1.4026457)

21. Zhao, S. & Gu, L. 2014 Implementation and validation of aortic remodeling in hypertensive rats. J. Biomech. Eng. 136, 091007. (doi:10.1115/1.4027939)

22. Grytsan, A., Watton, P. N. & Holzapfel, G. a 2015 A thick-walled fluid-solid-growth model of abdominal aortic aneurysm evolution: application to a patient-specific geometry. J. Biomech. Eng. 137, 1–10. (doi:10.1115/1.4029279)

23. Humphrey, J. D., Dufresne, E. R. & Schwartz, M. a. 2014 Mechanotransduction and extracellular matrix homeostasis. Nat. Rev. Mol. Cell Biol. 15, 802–812. (doi:10.1038/nrm3896)

24. Gleason, R. L. & Humphrey, J. D. 2015 A mixture model of arterial growth and remodeling in hypertension: altered muscle tone and tissue turnover. J. Vasc. Res. 41, 352–63. (doi:10.1159/000080699)

25. Alford, P. W. & Taber, L. A. 2008 Computational Study of Growth and Remodleing in the Aortic Arch. Comput. Methods Biomech. Biomed. Engin. 11, 525–538. (doi:10.1080/10255840801930710.Computational)

26. Kuhl, E., Garikipati, K., Arruda, E. M. & Grosh, K. 2005 Remodeling of biological tissue: Mechanically induced reorientation of a transversely isotropic chain network. J. Mech. Phys. Solids 53, 1552–1573. (doi:10.1016/j.jmps.2005.03.002)

27. DuFort, C. C., Paszek, M. J. & Weaver, V. M. 2011 Balancing forces: architectural control of mechanotransduction. Nat. Rev. Mol. Cell Biol. 12, 308–19. (doi:10.1038/nrm3112)

28. Webster, K. D., Ng, W. P. & Fletcher, D. a 2014 Tensional homeostasis in single fibroblasts. Biophys. J. 107, 146–55. (doi:10.1016/j.bpj.2014.04.051)

29. Paszek, M. J. et al. 2005 Tensional homeostasis and the malignant phenotype. Cancer Cell 8, 241–54. (doi:10.1016/j.ccr.2005.08.010)

30. Li, Q., Muragaki, Y., Hatamura, I., Ueno, H. & Ooshima, A. 1998 Stretch-induced collagen synthesis in cultured smooth muscle cells from rabbit aortic media and a possible involvement of angiotensin II and transforming growth factor-beta. J. Vasc. Res. 35, 93–103. (doi:10.1159/000025570)

31. Chiquet, M., Renedo, A. S., Huber, F. & Flück, M. 2003 How do fibroblasts translate mechanical signals into changes in extracellular matrix production? Matrix Biol. 22, 73–80. (doi:10.1016/S0945-053X(03)00004-0)

32. Bhole, A. P., Flynn, B. P., Liles, M., Saeidi, N., Dimarzio, C. A. & Ruberti, J. W. 2009 Mechanical strain enhances survivability of collagen micronetworks in the presence of collagenase: implications for load-bearing matrix growth and stability. Philos. Trans. A. Math. Phys. Eng. Sci. 367, 3339–3362. (doi:10.1098/rsta.2009.0093)

33. Hadi, M. F. & Barocas, V. H. 2013 Microscale fiber network alignment affects macroscale failure behavior in simulated collagen tissue analogs. J. Biomech. Eng. 135, 021026 1–8. (doi:10.1115/1.4023411)

34. Hadi, M. F., Sander, E. A., Ruberti, J. W. & Barocas, V. H. 2012 Simulated remodeling of loaded collagen networks via strain-dependent enzymatic degradation and constant-rate fiber growth. Mech. Mater. 44, 72–82. (doi:10.1016/j.biotechadv.2011.08.021.Secreted)

35. Chandran, P. L. & Barocas, V. H. 2007 Deterministic material-based averaging theory model of collagen gel micromechanics. J. Biomech. Eng. 129, 137–47. (doi:10.1115/1.2472369)

36. Stylianopoulos, T. & Barocas, V. H. 2007 Multiscale, structure-based modeling for the elastic mechanical behavior of arterial walls. J. Biomech. Eng. 129, 611–8. (doi:10.1115/1.2746387)

37. Chandran, P. L. & Barocas, V. H. 2006 Affine versus non-affine fibril kinematics in collagen networks: theoretical studies of network behavior. J. Biomech. Eng. 128, 259–70. (doi:10.1115/1.2165699)

38. Syedain, Z. H., Meier, L. a, Bjork, J. W., Lee, A. & Tranquillo, R. T. 2011 Implantable arterial grafts from human fibroblasts and fibrin using a multi-graft pulsed flow-stretch bioreactor with noninvasive strength monitoring. Biomaterials 32, 714–22. (doi:10.1016/j.biomaterials.2010.09.019)

39. Robinson, P. S., Johnson, S. L., Evans, M. C., Barocas, V. H. & Tranquillo, R. T. 2008 Functional tissue-engineered valves from cell-remodeled fibrin with commissural alignment of cell-produced collagen. Tissue Eng. Part A 14, 83–95. (doi:10.1089/ten.a.2007.0148)

40. Barocas, V. H. & Tranquillo, R. T. 1997 An anisotropic biphasic theory of tissue-equivalent mechanics: the interplay among cell traction, fibrillar network deformation, fibril alignment, and cell contact guidance. J. Biomech. Eng. 119, 137–145. (doi:10.1115/1.2796072)

41. Solon, J., Levental, I., Sengupta, K., Georges, P. C. & Janmey, P. A. 2007 Fibroblast adaptation and stiffness matching to soft elastic substrates. Biophys. J. 93, 4453–61. (doi:10.1529/biophysj.106.101386)

42. Tee, S.-Y., Fu, J., Chen, C. S. & Janmey, P. a 2011 Cell shape and substrate rigidity both regulate cell stiffness. Biophys. J. 100, L25–7. (doi:10.1016/j.bpj.2010.12.3744)

43. Mizutani, T., Haga, H. & Kawabata, K. 2004 Cellular stiffness response to external deformation: tensional homeostasis in a single fibroblast. Cell Motil. Cytoskeleton 59, 242–8. (doi:10.1002/cm.20037)

44. Ang, J. & McMillen, D. R. 2013 Physical constraints on biological integral control design for homeostasis and sensory adaptation. Biophys. J. 104, 505–15. (doi:10.1016/j.bpj.2012.12.015)

45. LeDuc, P. R., Messner, W. C. & Wikswo, J. P. 2011 How do control-based approaches enter into biology? Annu. Rev. Biomed. Eng. 13, 369–96. (doi:10.1146/annurev-bioeng-071910-124651)

46. Steil, G., Rebrin, K. & Mastrototaro, J. J. 2006 Metabolic modelling and the closed-loop insulin delivery problem. Diabetes Res. Clin. Pract. 74, S183–6. (doi:10.1016/S0168-8227(06)70028-6)

47. Peterka, R. 2003 Simplifying the complexities of maintaining balance. Eng. Med. Biol. Mag. IEEE 22, 63–68. (doi:10.1109/MEMB.2003.1195698)

4.7 Tables

Table 4.1.
Dimensionless governing equations for rates of removal and addition.

Case	Rate equation	Parameters
	Removal	
All	$\left(\frac{d\rho}{d\zeta}\right)_{removal} = -\frac{\rho}{\rho+\rho_o}\exp(-k_2(\lambda_{fiber}-1))$	k_2 = 0.83 [24]
	Addition	
1	$\left(\frac{d\rho}{d\varsigma}\right)_{addition} = \alpha$	α = 0.9, 0.92, 0.95, 1.0
2	$\left(\frac{d\rho}{d\varsigma}\right)_{addition} = \alpha\exp(k_4(\lambda_{cell}-1))$	α = 0.9, 0.92, 0.95 k_4 = 0.83 (kept same as k_2)
3	$\left(\frac{d\rho}{d\varsigma}\right)_{addition} = \alpha\frac{\exp(\kappa\cos(2(\theta-\theta_o)))}{I_o(\kappa)}$	α = 0.9, 0.92, 0.95 κ = 0.02,0.04,0.06, 0.08
4	$\left(\frac{d\rho}{d\varsigma}\right)_{addition} = \alpha\exp(k_4(\lambda_{cell}-1))\frac{\exp(\kappa\cos(2(\theta-\theta_o)))}{I_o(\kappa)}$	α = 0.9, 0.92, 0.95 k_4 = 0.83 κ = 0.02,0.04,0.06, 0.08

4.8 Figures

Figure 4.1. Model of Cell and Network System. In this parallel configuration, the cell and network experience the same strain, ε_{Tot}, and the total stress of the system, σ_{Tot}, is the sum of the cell and network stresses.

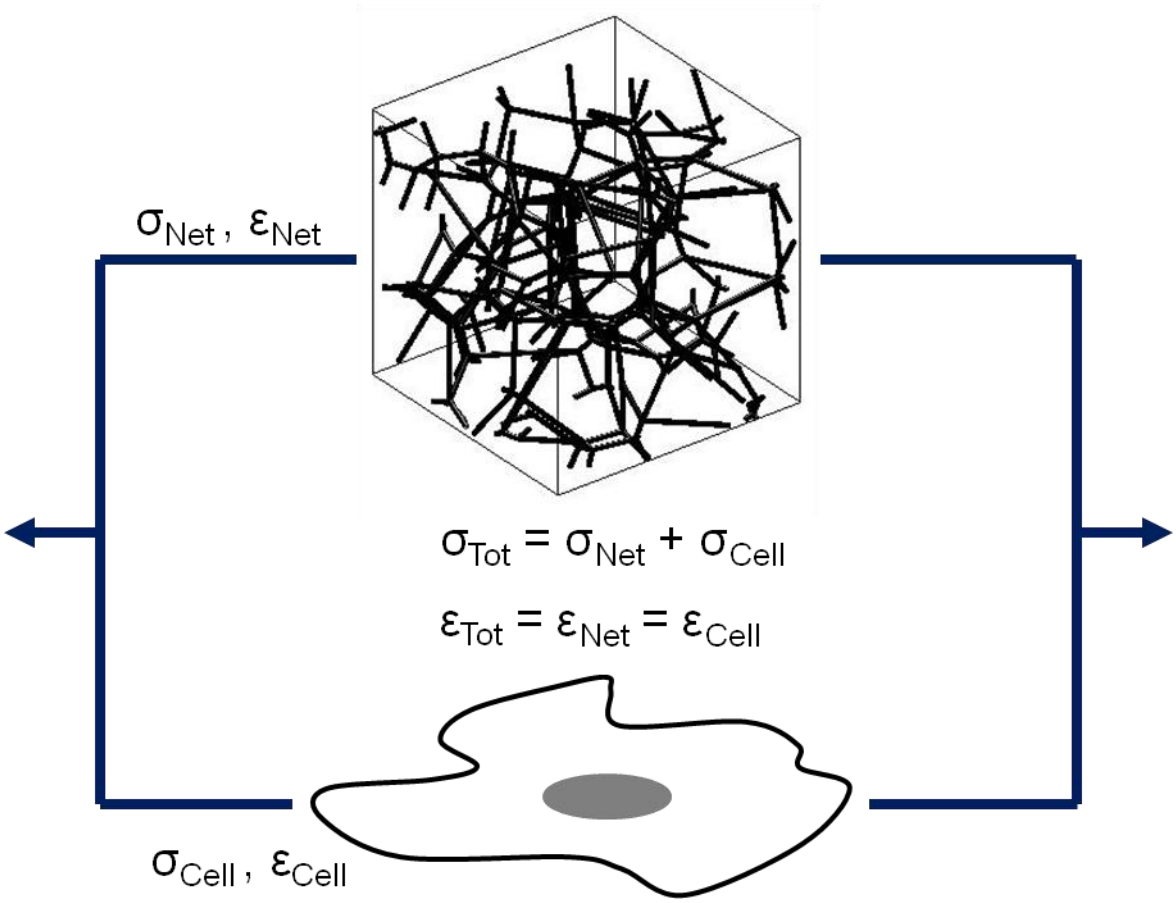

Figure 4.2. Schematic of Remodeling Model. (a) A network is generated as described in Section 2.1. **(b)** Before remodeling starts, the system of cell + collagen network is deformed to some strain ε and its concomitant stress σ. **(c)** The final stress in the system ($\sigma_{applied}$) is maintained during remodeling **(d)**, which causes the strain to change by either increasing or decreasing over time depending on the net rate of collagen deposition and removal. In this example, the net amount of collagen in the network increases, causing the system to contract to maintain the same level of applied stress.

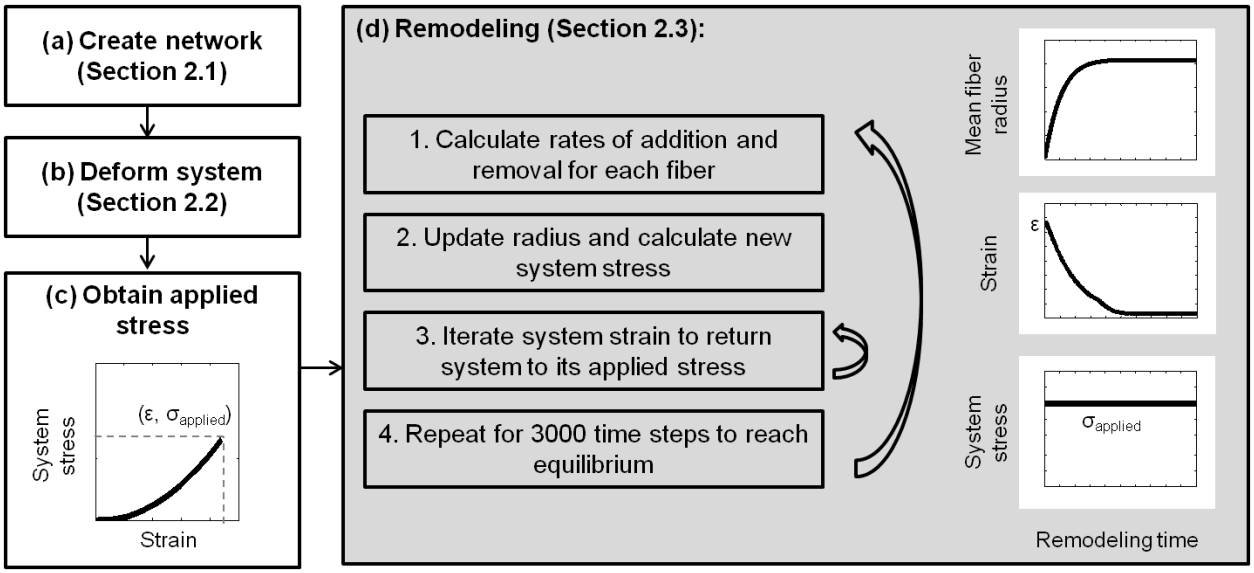

Figure 4.3. Cellular Contribution to the System Stress. (a) Once the remodeling system reached equilibrium at different applied stresses (stress A and stress B in the schematic below), the equilibrium cellular contribution to the system stress (C_A and C_B) were determined. **(b)** An aggregate plot was produced of the equilibrium cell stress vs. applied stress, with each part representing one of the plots from panel (a). A cell in perfect tensional homeostasis would see the cellular stress plateau – the equilibrium cell stress becomes independent from the applied system stress.

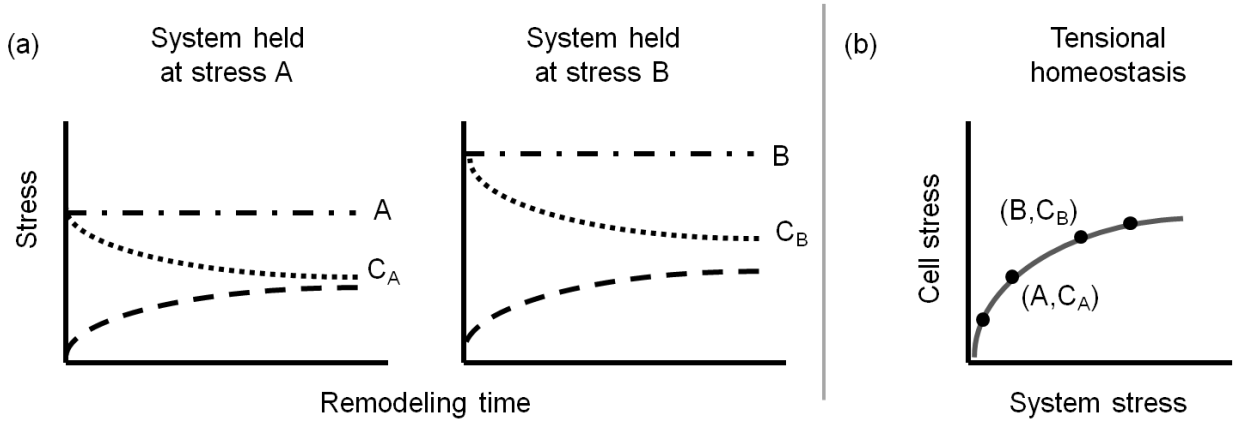

Figure 4.4.Choosing values for parameter α. The values selected for alpha ensured that the collagen network had overall higher rates of addition than removal and that the network was able to reach equilibrium. **(a)** For a low value of α = 0.8, the amount of collagen in the network decreases, especially at low stretches. **(b)** For a high value of α = 1.0, the network is not able to equilibrate because the rate of addition is substantially larger than the rate of removal.

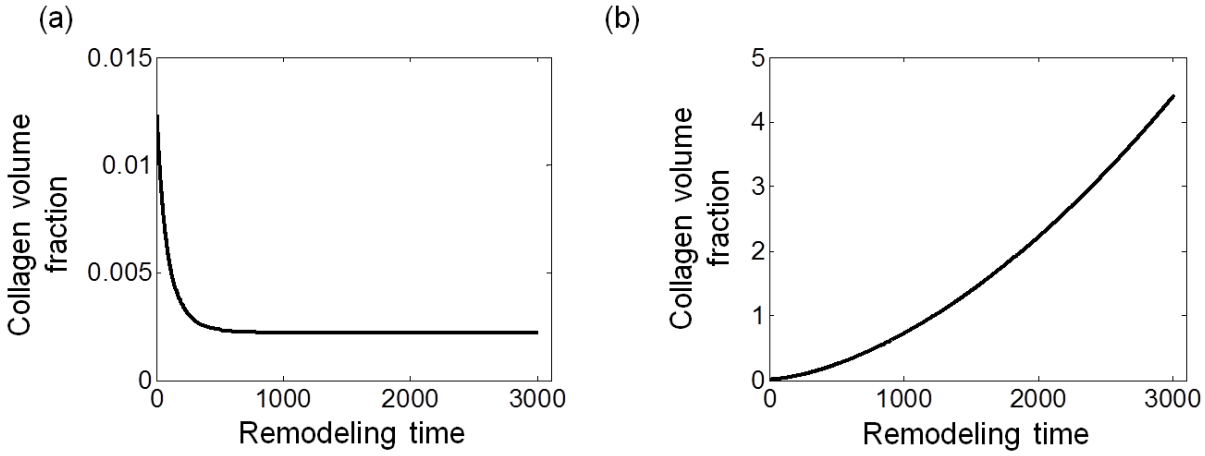

Figure 4.5. Typical Remodeling Results. The results are for Case 1 (constant addition, $k_4 = \kappa = 0$), at 20% initial strain, $\alpha = 0.9$, and a cell with stiffness equal to the network stiffness, but are representative of other cases and parameters. **(a)** The system was perturbed to a new stress (171 kPa), and the collagen network remodeled at constant system stress until both the cell and network reached equilibrium. **(b)** The rate of collagen addition was larger than the rate of collagen removal, causing the collagen volume fraction to increase as remodeling proceeded. **(c)** As more collagen was added, the system had to contract from the initial strain of 20% to maintain the total system stress constant. **(d)** The effect of remodeling on the network can be easily seen by plotting the collagen fibers to scale. Before remodeling, each fiber had radius of 50 nm and the volume fraction of the matrix was 1.2%. At the end of remodeling, the volume fraction had increased to 2.7% and the radius of fibers in the network had visibly increased.

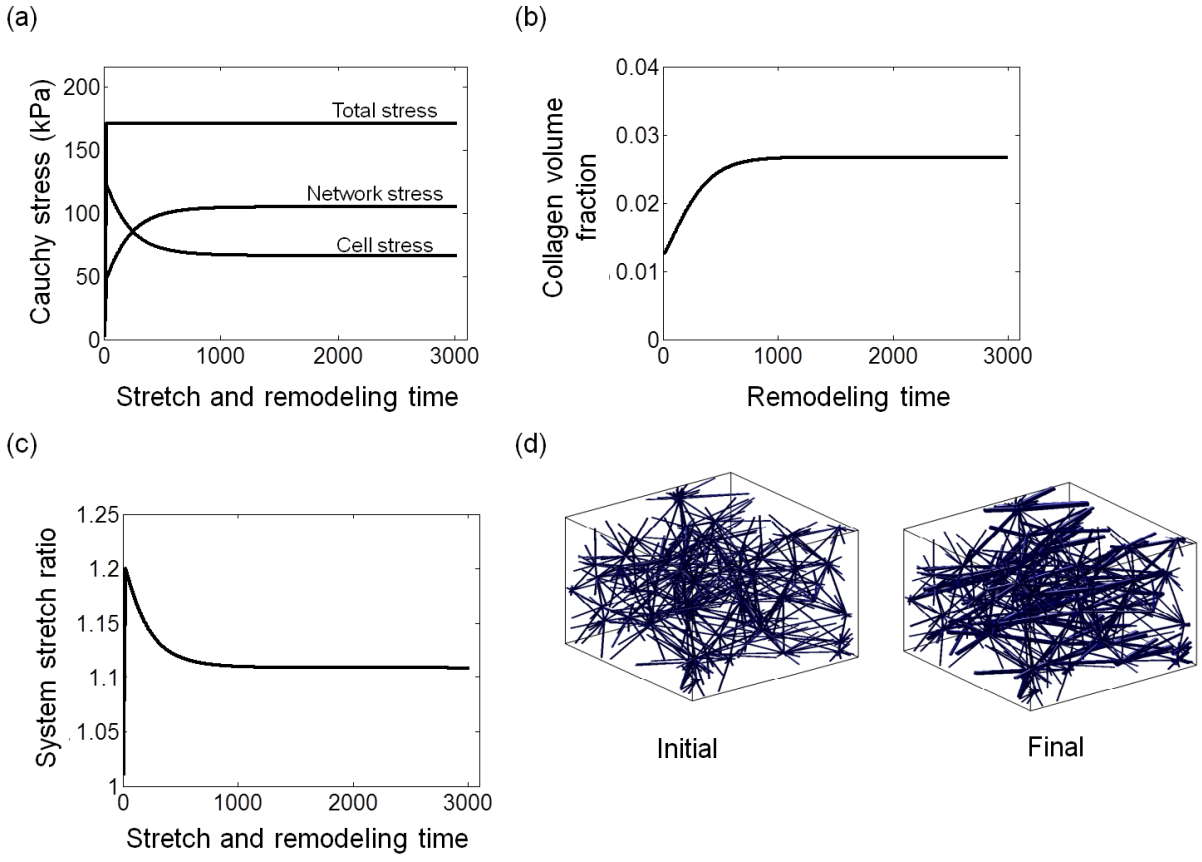

Figure 4.6. Changes to fiber radius distribution during remodeling. The results are for Case 1 (constant addition, $k_4 = \kappa = 0$), at 20% initial strain, $\alpha = 0.9$, and a cell with stiffness equal to the network stiffness, but are representative of other cases and parameters. **(a)** The mean collagen fiber radius increased with remodeling before reaching equilibrium. **(b)** Before remodeling, all fibers (721 for this network) had a fiber radius of 50 nm. During remodeling, some fibers saw an increase in radius. The increase was not the same for all fibers because even though the addition rate was constant in Case 1, the removal rate was not.

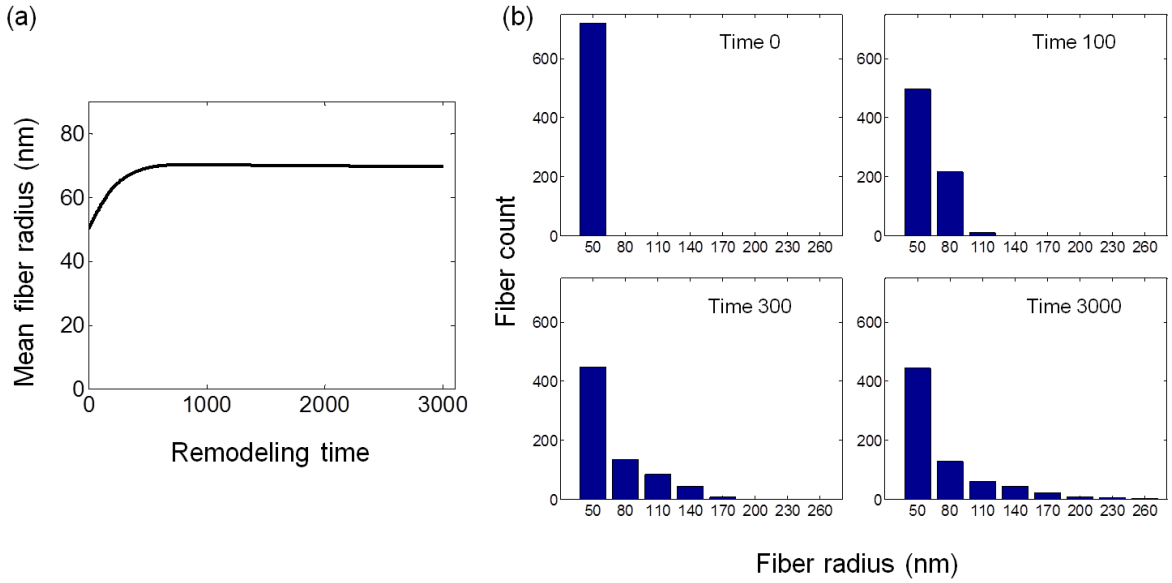

Figure 4.7. Varying the rate of addition in Case 1. (a) For all α values, the rate of addition was larger than the rate of removal, leading to net deposition of collagen and increase in the collagen volume fraction with remodeling. **(b)** Increase in α resulted in decrease in the cellular contribution to the equilibrium stress. For all α values, the cell stress appears to be approaching a plateau but does not reach it. **(c)** Representative remodeled network for Case 1 at 20% initial stretch.

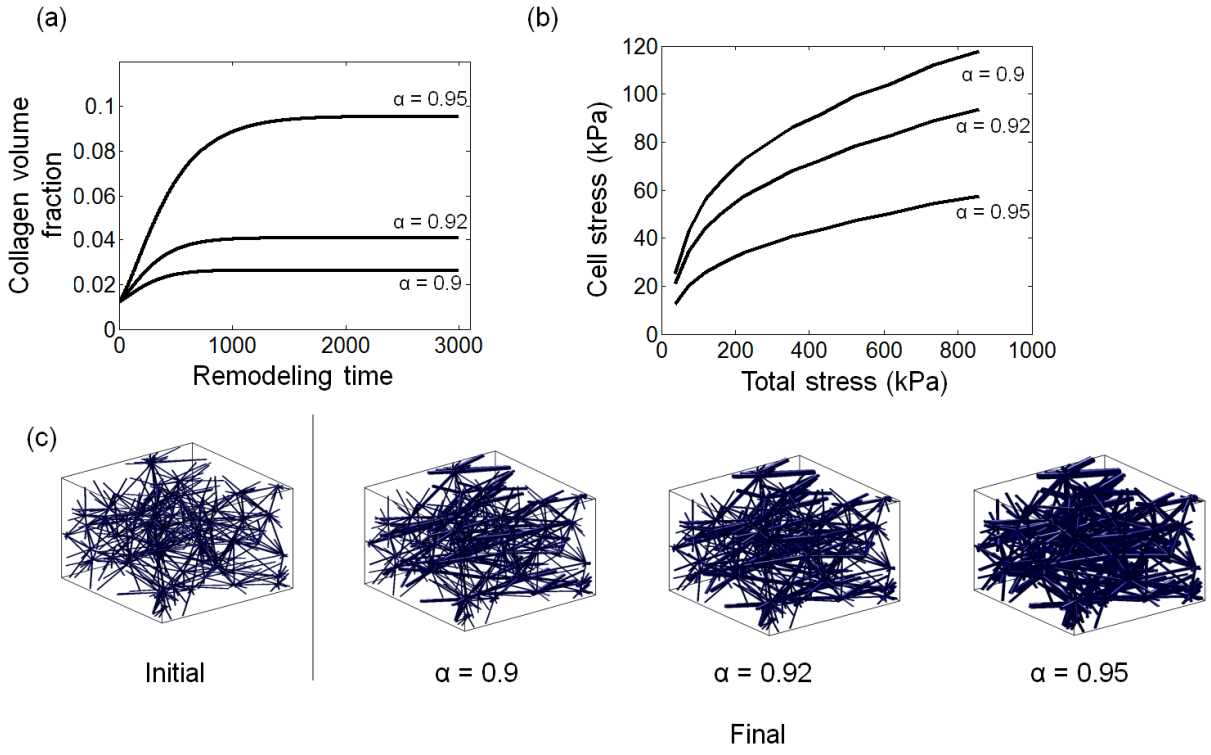

Figure 4.8. Effect of cell stiffness. Representative results for Case 1, $\alpha = 0.9$. As the cell stiffness increased, the cell stress increased but the qualitative results were unchanged.

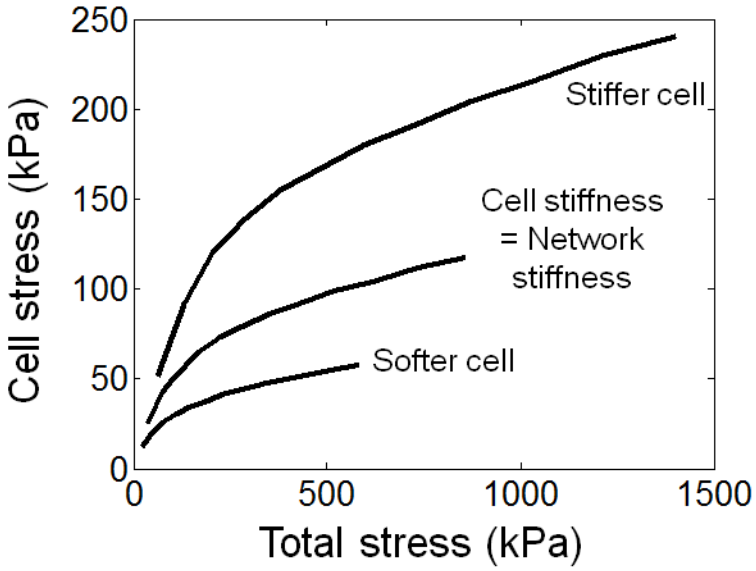

Figure 4.9. Remodeling with Case 2 – addition dependent on cell stretch. All plots are with $\alpha = 0.9$ and a cell with stiffness equal to that of the network. **(a)** As in Case 1, network stress went up with remodeling and cell stress decreased. **(b)** For all initial stretches, the system returned to almost its initial configuration. Only 500 remodeling steps shown for clarity. **(c)** The cell stress was only about 10% of total system stress. Cell stress increased with network stress and did not become homeostatic.

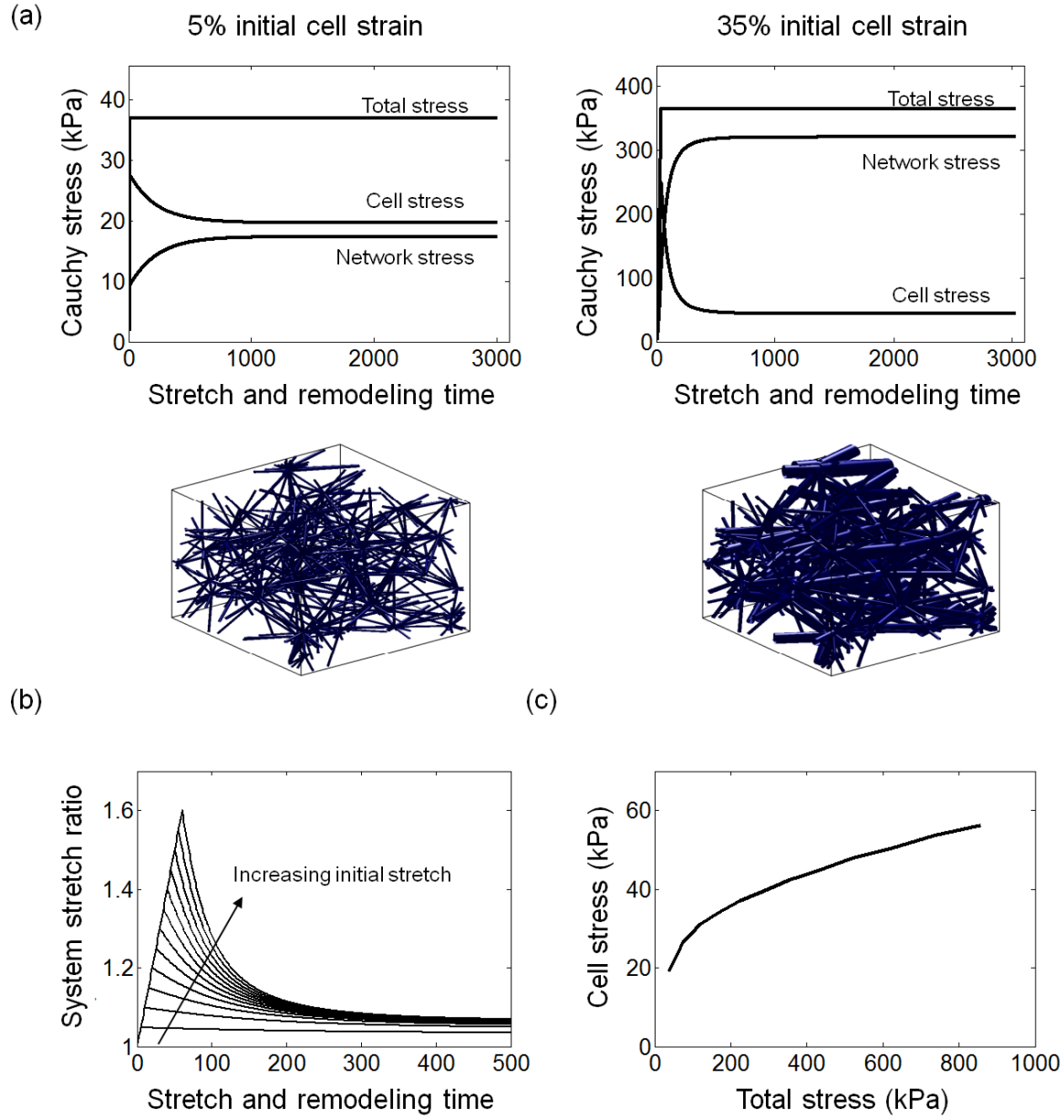

Figure 4.10. Remodeling with Case 3. (a) Representative data with α = 0.9, 20% initial stretch, cell stiffness equal to network stiffness, and κ = 0.02. Parameters are the same for (b)-(d) but κ is varied. **(b)** The amount of deposited collagen increased with an increase in κ. **(c)** The system returned to a smaller strain and a higher value of κ resulted in a larger system contraction. **(d)** Increasing κ resulted in a decrease in the cell stress fraction from the total stress.

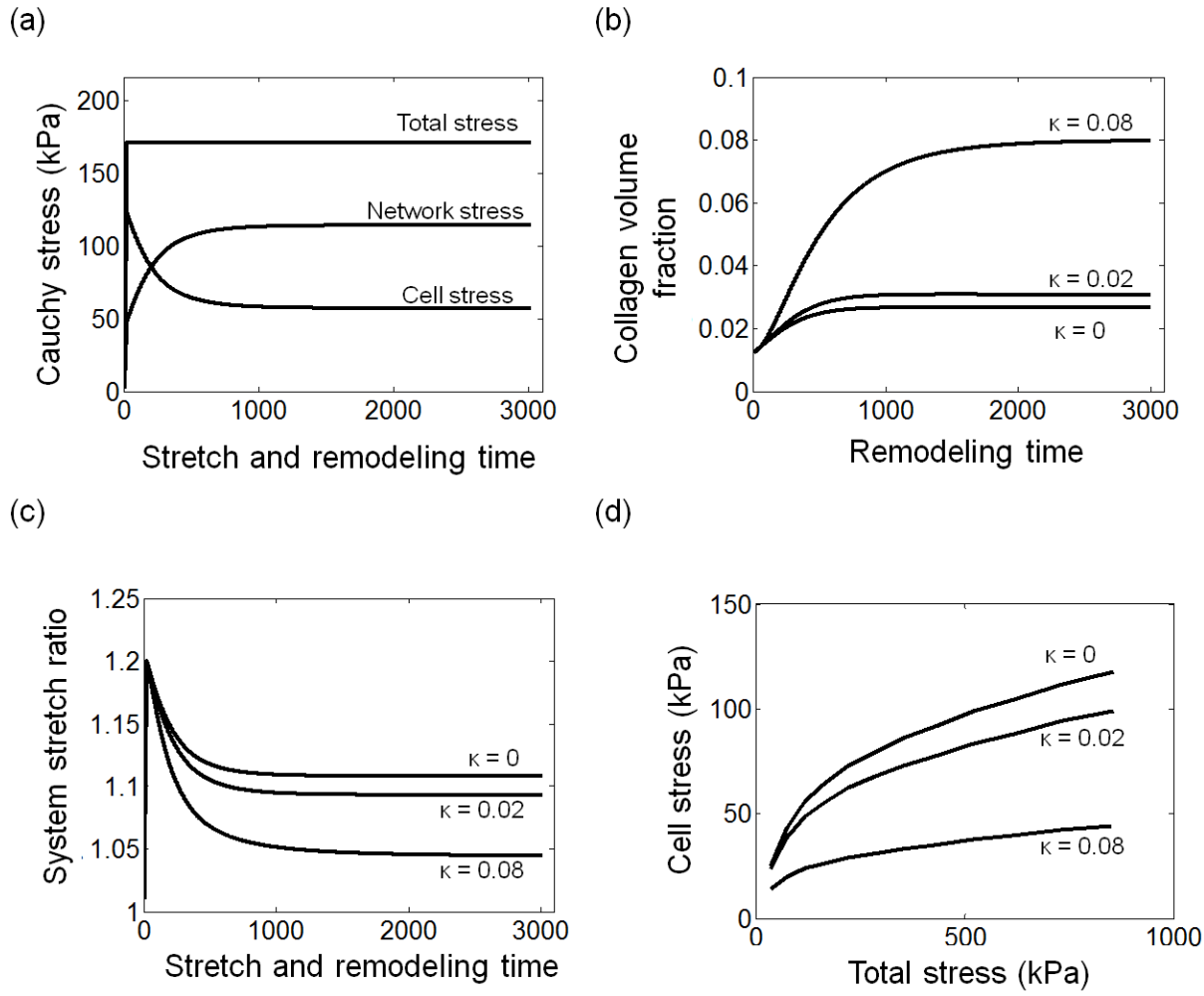

Figure 4.11. Remodeled networks in Case 3 – preferential deposition of fibers in direction of stretch (1-direction). Representative results with $\alpha = 0.9$ and 20% initial stretch. At $\kappa = 0$, collagen addition was constant for all fibers and not affected by fiber orientation. At even small increases of κ, a preferential deposition was observed - the fibers oriented in the 1-direction had a much larger radius.

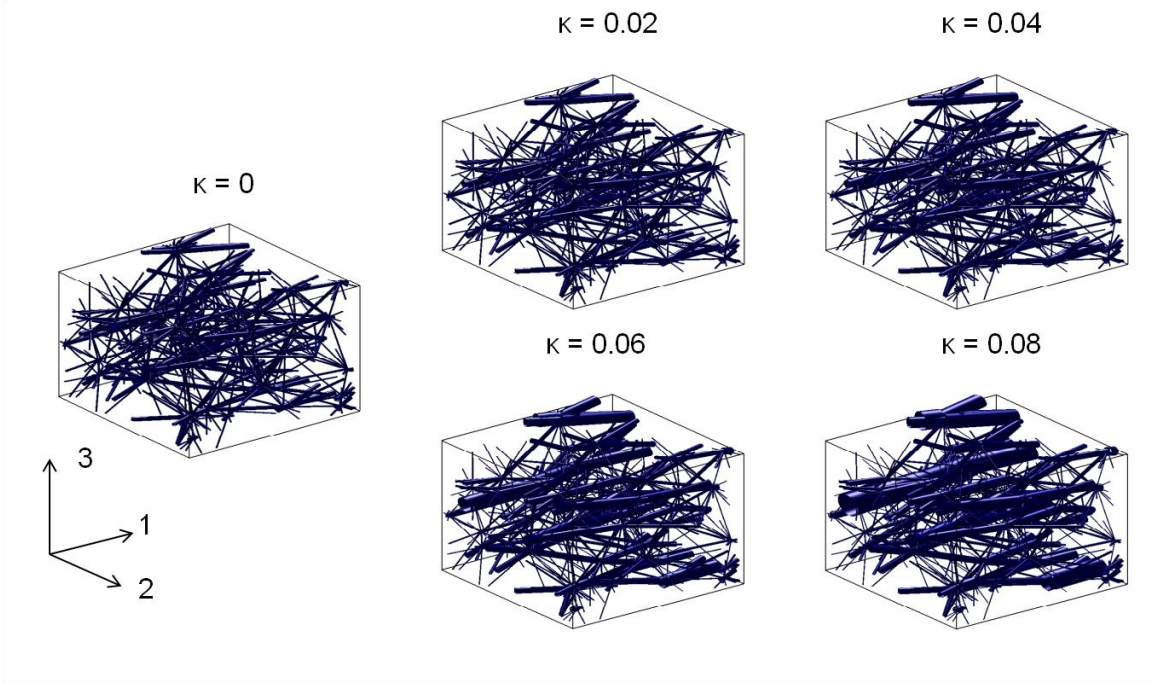

Figure 4.12. Remodeling with Case 4. (a) Representative data with $\alpha = 0.9$, 20% initial stretch, cell stiffness equal to network stiffness, and $\kappa = 0.02$. Parameters are the same for (b)-(d) but κ is varied between 0.02 and 0.08. **(b)** The amount of deposited collagen increased with an increase in κ. **(c)** The system returned to a smaller strain and a higher value of κ resulted in a larger system contraction. **(d)** Increasing κ resulted in a decrease in the cell stress fraction from the total stress.

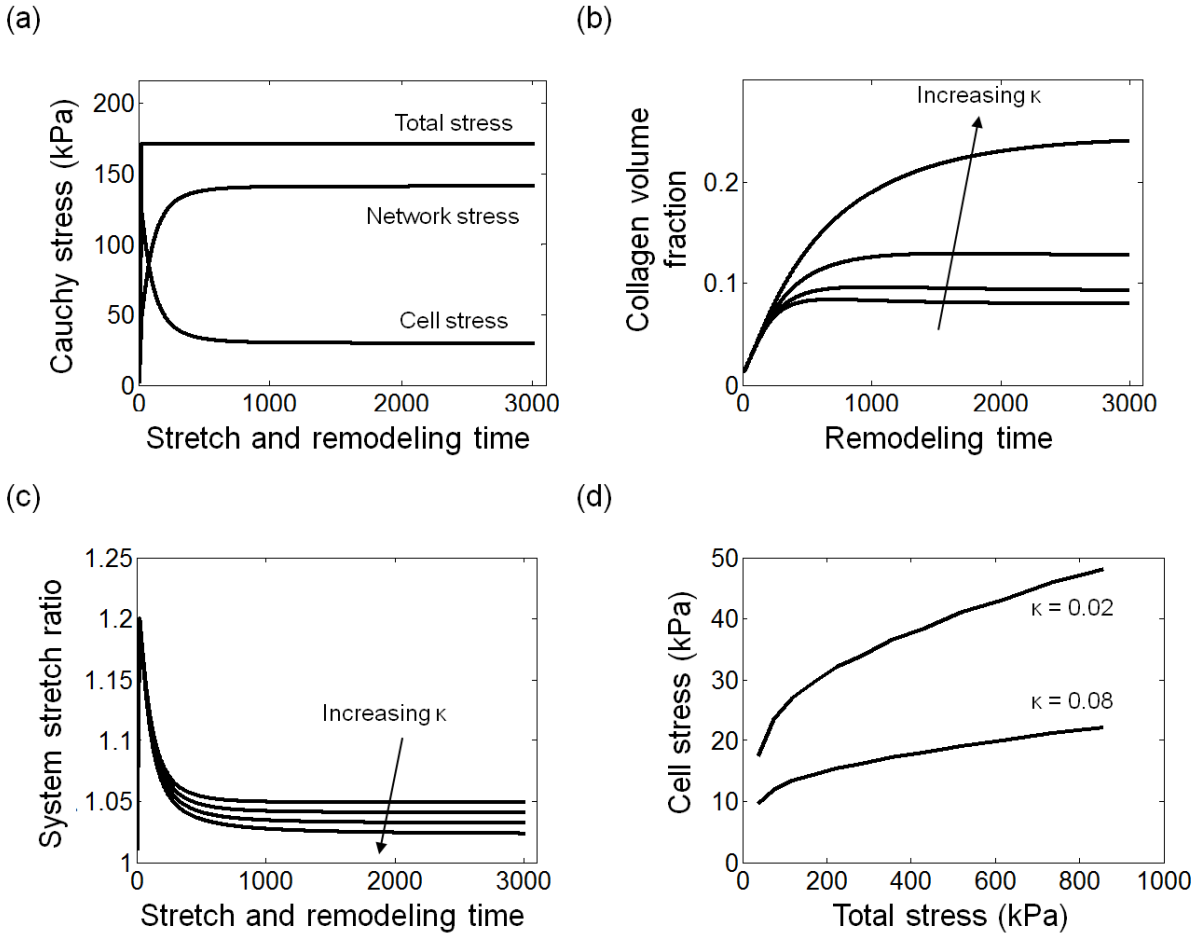

Figure 4.13. Remodeled networks in Case 4 - combining effects of cell stretch and preferential fiber deposition. At low 5% strain, Cases 2 and 4 are very similar, when the network has not rearranged much, and they both have larger collagen fibers than Case 3. At high strain, the collagen fibers in Case 4 have a visibly larger radius that those in Cases 2 and 3. Case 3 has the clearest difference in fiber radius between fibers aligned in the 1-direction and those perpendicular to it. In Case 4, the presence of the term which increases collagen deposition with cell stretch ensures that fibers in the other directions also see an increase in radius.

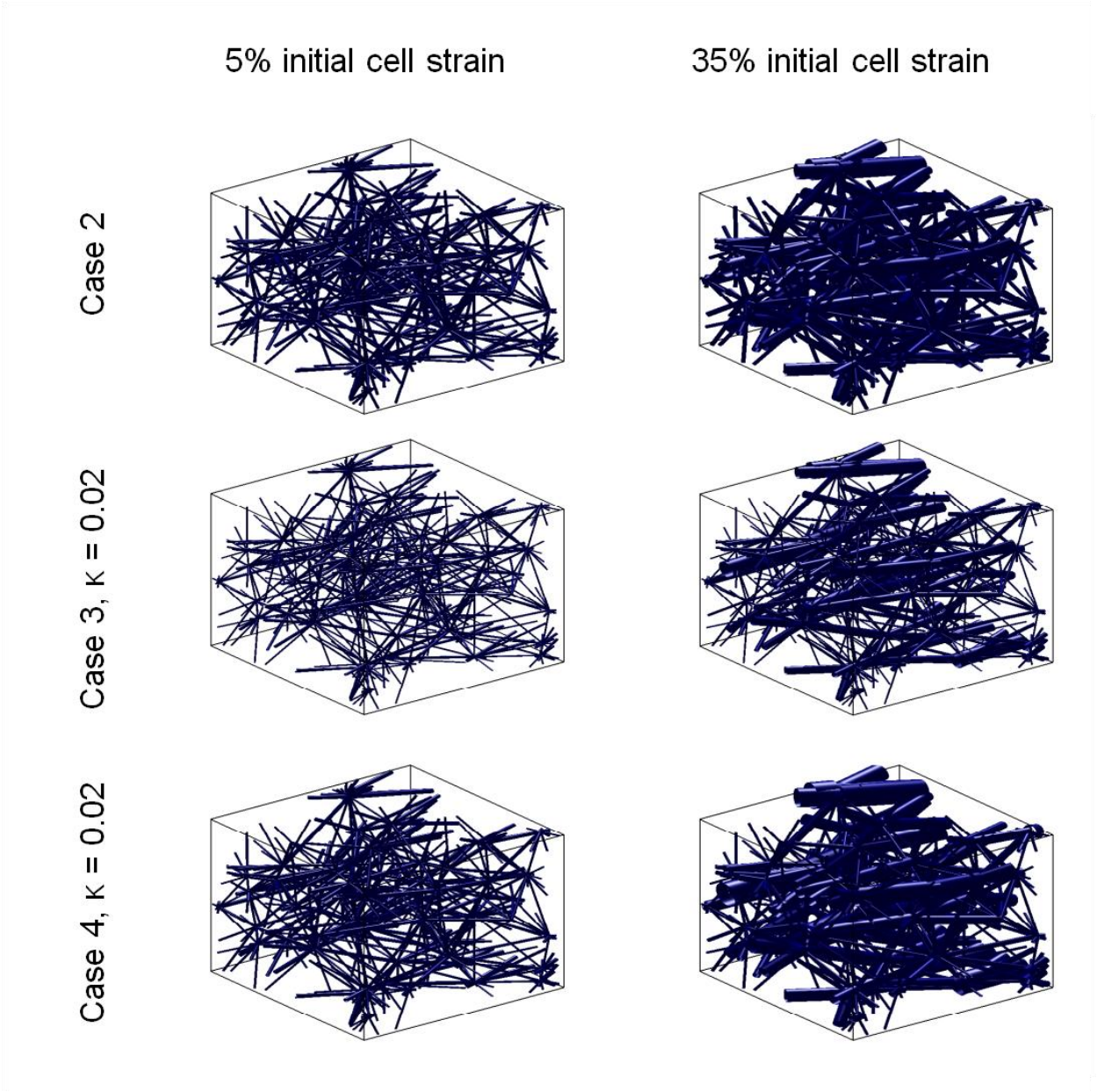

Figure 4.14. Comparing cellular contribution between cases. All cases produced similar results, though for some, the fraction of cell stress out of total stress was reduced. Data is with $\alpha = 0.9$ for all cases and $\kappa = 0.02$ for Cases 3 and 4.

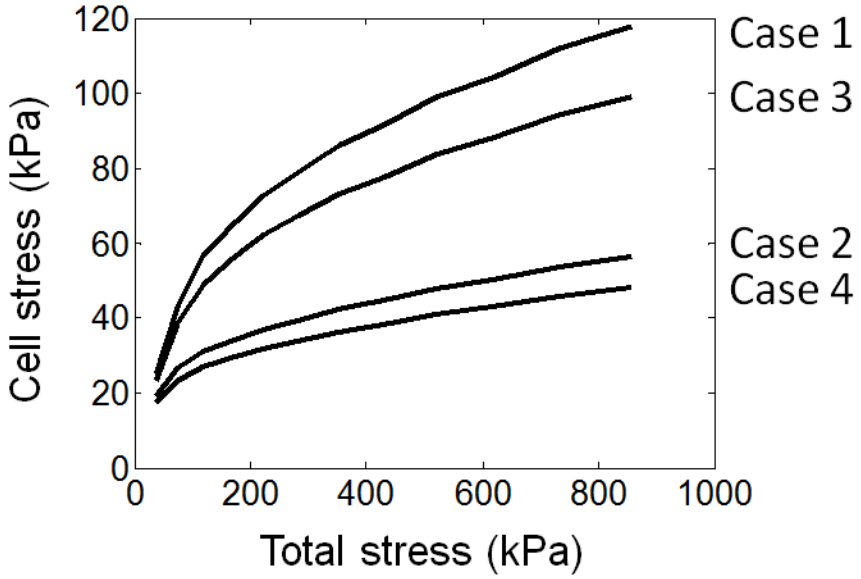

Chapter 5: Flow-rate-controlled remodeling of glomerular capillaries: current model and future outlook

5.1 Summary

Based on observations from the previous three chapters (ability of supercoiling to increase network stiffness without affecting permeability, combined with experimental evidence that α3(IV)α4(IV)α5(IV) networks are more protected from enzymatic degradation), we hypothesized that remodeling of the glomerular basement membrane (GBM) in the presence of α3(IV)α4(IV)α5(IV) networks would stabilize the system, while remodeling in the presence of [α1(IV)]2α2(IV) networks could cause a breakdown in the autoregulatory negative feedback loop. For that purpose, we applied the cell-matrix remodeling scheme from Chapter 4 to a multiscale finite element model of the glomerular capillaries, containing one layer of elements representing the GBM and one layer representing podocytes. The capillary model was inflated to a physiological pressure and allowed to remodel by depositing and removing collagen IV material incorporating feedback from the cell layer. Remodeling was performed at a constant transcapillary filtration rate. To preserve the filtration rate, the applied pressure, and subsequently the capillary thickness and diameter, were allowed to change. Remodeling with the α3(IV)α4(IV)α5(IV) networks resulted in net deposition of material, reduction in the system stresses and decreases in capillary strain and capillary pressure. Remodeling with

the [α1(IV)]2α2(IV) networks saw opposite trends: there was net removal of material, system stresses and strains increased, and pressure increased. The simulation results were due to differences in removal rates of the [α1(IV)]2α2(IV) networks, not due to the mechanical difference between supercoiled and non-supercoiled networks. The current model is at its early stages of development, but future modifications will ensure that the model is representative of physiological GBM remodeling and will allow us to answer important questions about the progression of Alport syndrome.

5.2 Introduction

The glomerular capillary wall is a highly specialized ultrafilter with size and charge selectivity. It is composed of three layers: a glomerular basement membrane (GBM), a layer of endothelial cells on the luminal side of the GBM, and specialized epithelial cells called podocytes on the outer side of the GBM (Figure 1) [1]. The GBM and podocyte layers are believed to contribute the majority of the water resistance of the filter, so we will focus on them [2]. Importantly, the GBM also provides mechanical support and anchorage for the cells attached to it, resists tensile deformation of the capillaries, and holds a reserve of cytokines and other signaling molecules. The capillary wall must be stiff enough to oppose distension but still be porous enough to allow filtration - two opposing tasks [3,4]. Keeping them in balance is vital for the normal function of the kidney.

The amount of water and solutes filtering through the capillaries is tightly regulated by the tubuloglomerular feedback (TGF) system [5]. As part of the TGF system, sensor cells in the tubules respond to deviations in the flow rate and salt content of luminal fluid. The feedback has a complicated mechanism of inputs and outputs, but its actions in response to an increase in filtration rates is illustrative. In case of increased glomerular hydrostatic pressures, filtration of water and salts through the capillary wall increases; in response, the sensory cells detect the change and initiate a signaling cascade causing constriction of the afferent arteriole and reduction of the glomerular capillary pressure and filtration rates. The role of this negative feedback controller, however, can be disrupted in some disease states [6–8].

In the genetic disease Alport syndrome, for example, mutations prevent the proper function of the GBM [9]. The GBM is composed primarily of laminin, type IV collagen, nidogen, and proteoglycans, of which, type IV collagen is the component primarily responsible for the mechanical stability of the GBM. The type IV collagen of the embryonic GBM is a heterotrimer of the α1(IV) and α2(IV) isoforms, but in the mature GBM a developmental switch in podocytes begins production of a heterotrimer made up of the α3(IV), α4(IV), and α5(IV) isoforms [10]. In Alport syndrome, the α3(IV)α4(IV)α5(IV) networks are absent from GBMs [11]. The α3(IV)α4(IV)α5(IV) networks are more resistant to degradation from matrix metaloproteinases and are likely stiffer and less distensable than the $[\alpha1(IV)]_2\alpha2(IV)$ networks [12]. Podocytes compensate for the loss of the α3(IV)α4(IV)α5(IV) protomers by overproducing the $[\alpha1(IV)]_2\alpha2(IV)$ protomers, but the resulting collagen networks do not seem capable of

dealing with the large forces acting on mature GBMs. The filtration barrier of the capillary wall gradually becomes leaky, eventually letting through large proteins and blood cells [13]. Later stages of the disease present scarring and hypertension in remaining glomeruli and an overall decrease in the filtration flow rate of the kidneys, ultimately resulting in kidney failure.

The progression of Alport syndrome illustrates the importance of the α3(IV)α4(IV)α5(IV) collagen IV networks for maintaining the mechanical and permeability properties of the glomerular filtration barrier, as well as the failure of renal control systems to maintain normal function. The opposing challenges of mechanical stability and high permeability must remain in balance, even as the capillaries are growing, remodeling, or responding to abnormal conditions. One possibility for the loss of GBM functionality in Alport syndrome is that the capillaries experience larger than normal deformations with the more distensible $[\alpha1(IV)]_2\alpha2(IV)$ collagen IV networks. The larger strains on the podocytes may initiate abnormal remodeling mechanisms of the GBM, or even detachment/death of podocytes, all of which would affect the filtration rates. Over time, the more easily degraded $[\alpha1(IV)]_2\alpha2(IV)$ networks would likely cause further loss of mechanical function and more attempts by podocytes to rescue the system, but clinically we see that they are unable to do so. Our goal is to investigate how a GBM remodeling scheme would function when subjected to the constraint of constant filtration rate in a GBM with normal α3(IV)α4(IV)α5(IV) collagen IV networks and more distensible and degradable $[\alpha1(IV)]_2\alpha2(IV)$ networks.

5.3 Methods

To investigate the differences between the α3(IV)α4(IV)α5(IV) and $[\alpha1(IV)]_2\alpha2(IV)$ networks, we used a custom multiscale finite element code that allowed us to monitor the effects of remodeling on both the microscale glomerular capillary and nanoscale collagen IV networks. Glomerular capillaries were modeled as a quarter section of a thin cylinder (making a simplification of mirror symmetry) and small axial length. The capillary wall consisted of two layers: an inner GBM layer and an outer podocyte layer. Both layers were modeled using a multiscale scheme that included a representative network (collagen IV network in GBM and cytoskeleton in podocytes) at each integration point in the model. The simulated capillary was inflated to a physiological pressure and then allowed to remodel, with new GBM being secreted in response to the podocyte strain. Since the new GBM also affected the permeability of the GBM, the capillary pressure was adjusted to maintain constant filtration rate, simulating tubuloglomerular feedback. The entire system was allowed to evolve to a new steady state. The simulations were performed with either α3(IV)α4(IV)α5(IV) or $[\alpha1(IV)]_2\alpha2(IV)$ networks to compare how remodeling proceeds in each case.

5.3.1 Whole Capillary Model

In the multiscale finite element model, the capillary was modeled as a quarter section of a cylindrical capillary with initial diameter of 8 μm, thickness of 600 nm, and short axial length of 1 μm (Figure 2). The geometry was discretized into two layers with

7 finite elements in each layer - the inner layer representing the GBM and the outer layer representing the podocytes. The complex shape of podocytes was not replicated in our model as the cell layer was primarily concerned with detecting strains and depositing material. Pressure was applied to the inner capillary surface to expand it to a diameter of 10 μm at pressure of 20 mmHg, which are normal conditions for the glomerular capillary.

The custom multiscale finite element model has been described previously and used for a variety of geometries and conditions [14–17]. The multiscale model links the nanoscale, in which the collagen IV networks operate, and the microscale of the glomerular capillaries. Each element in the capillary geometry (14 elements total) contained 8 Gauss integration points at which a representative volume element (RVE) was constructed of collagen IV or actin representing networks. Networks are described in the next section. The calculation of stresses on each RVE was performed as described in Chapter 3 for the simulations performed in MATLAB on a single RVE. The stresses on the equilibrated nanoscale RVEs were passed onto the microscale geometry to calculate the stresses in each element and equilibrate the microscale forces. Pressure was applied as a boundary condition on the inner/luminal surface by adding it to the residuals for those elements - residuals used in the microscale force balance. The capillary was also fixed on its "bottom" axial surface but was allowed to translate along the planer axes. All other surfaces were free.

The capillary was inflated in steps of 2 mmHg to a final pressure of 20 mmHg. Transcapillary flow rate, *Q*, was calculated at each step as

$$Q = \frac{k_{Tot} A P}{\mu h} \qquad \text{(Equation 5.1)}$$

where k_{Tot} is the Darcy permeability through the RVE and podocyte layers, A is the cross sectional area of the element, P is the transcapillary pressure, μ is the fluid viscosity, and h is the thickness of the two layers. Taking the GBM and podocyte layers as to resistors in series, k_{Tot} was found as:

$$\frac{1}{k_{Tot}} = \frac{1}{k_{GBM}} + \frac{1}{k_{Cell}} \qquad \text{(Equation 5.2)}$$

The permeability of the cell layer was held constant at the permeability of the GBM at the last inflation step. Thus, unlike k_{GBM}, k_{Cell} was not changed during remodeling.

The simulations were run on the Minnesota Supercomputing Institute's Itasca module, using 32 nodes in parallel, each simulation taking approximately 5 hours.

5.3.2 Network generation

The RVEs constructed at the Gauss points of the inner layer were representative of the collagen IV networks found in the GBM. The RVEs in the outer layer were representative of the actin cytoskeleton of podocytes. The two types of networks had different properties and organization. Each element had a unique randomly generated network.

Similarly to the networks described in Chapter 3, collagen IV networks were modeled by Voronoi networks created in Matlab. However, the radius of the protomers was set to 50 nm, much larger than that of physiological collagen IV molecules but the volume fraction of collagen IV was still 0.04, which is normal for the GBM. The generated Voronoi networks were aligned to match the orientation of the elements. This

was done by stretching the whole isotropic network in one direction, cropping the RVE to its original size, and rotating all the nodes in the network to match the angle of the corresponding element. The aligned networks were supercoiled using the previously described method: at each node, the two protomers with the smallest angle were combined for 30% of the length of the shorter protomer. The resulting supercoil was given twice the radius of a non-supercoiled protomer, and its undeformed length was artificially reduced so the amount of material was preserved.

The actin representative networks were constructed based on the edges of Delauney tessellations, which produce networks of much higher nodal connectivity than the Voronoi method. The higher connectivity gives the networks higher stability, which was needed because actin parameters were chosen to make the networks 10 times softer than the GBM networks, but the multiscale code struggled with very soft Voronoi networks. The Delauney networks were rotated the same way as the Voronoi networks to align them with their corresponding elements. Examples of the generated networks can be seen in Figure 2.

5.3.3 Remodeling

Remodeling was modeled similarly to the approach described in Chapter 4, but with some important distinctions applicable to a GBM-podocyte system. Only the networks in the inner GBM representative layer were remodeled. Addition and removal of collagen IV material was still modeled by increasing or decreasing, respectfully, the

radius of collagen IV protomers. The removal rate was dependent on the stretch ratio of the collagen IV protomers

$$\left(\frac{d\rho}{d\zeta}\right)_{removal} = -\frac{\rho}{\rho+\rho_o}\exp(-k_2(\lambda_{fiber}-1)) \qquad \text{(Equation 5.3, also see Equation 4.5)}$$

where more stretched fibers were more protected. For the addition rate, only one case was considered this time, basing deposition on the strain of the cell

$$\left(\frac{d\rho}{d\zeta}\right)_{addition} = \alpha\exp(k_4(\lambda_{cell}-1)) \qquad \text{(Equation 5.4)}$$

The more stretched the cell was, the more material it deposited. Experiments by [11] have shown that the α3(IV)α4(IV)α5(IV) collagen IV networks are more protected from enzymatic degradation, compared to $[\alpha1(IV)]_2\alpha2(IV)$ networks. In the simulations performed with $[\alpha1(IV)]_2\alpha2(IV)$ networks, the removal rate calculated for each protomer was increased by 50%. Supercoils are believed to be more protected from enzymatic degradation [12] and their removal rate was decreased by 50%. The net rate of radius change (Equation 5.5) and the new fiber radius (Equation 5.6) were then calculates as:

$$\left(\frac{d\rho}{d\zeta}\right)_{net} = \left(\frac{d\rho}{d\zeta}\right)_{addition} + \left(\frac{d\rho}{d\zeta}\right)_{removal} \qquad \text{(Equation 5.5, also see Equation 4.12)}$$

$$r_{\zeta+1} = r_\zeta + \left(\frac{d\rho}{d\zeta}\right)_{net} r_\zeta \qquad \text{(Equation 5.6, also see Equation 4.13)}$$

Remodeling of the GBM layer was initiated only after the ring had been inflated to 20 mmHg. The trascapillary flow rate at 20 mmHg is set as the target flow rate of the system, Q_{Target}, and the pressure, P, was modulated during remodeling to maintain the target flow (similar to the auto regulation mechanism of the glomerular capillaries) using

Newtonian iterations. After each remodeling step, the permeability through the networks, k_{GBM}, was calculated, together with the new capillary thickness, h, and the cross sectional area of the capillary, A. The updated values were used to calculate the current flow rate, $Q_{Current}$. Permeability was calculated using the same method described in Chapter 3. The deviation of the current flow rate from Q_{Target} was found as:

$$\Delta Q = Q_{Current} - Q_{Target} \qquad \text{(Equation 5.7)}$$

and used to calculate the needed new pressure by a Newton step:

$$P = \Delta Q \frac{dP}{dQ} \qquad \text{(Equation 5.8)}$$

The $\frac{dP}{dQ}$ term comes from the slope of a Pressure-Flow curve built during inflation which is nearly linear. The process is iterated 10 times which is enough for Q_{Target} to be maintained.

5.4 Results

Remodeling in the capillary system was modeled with both the supercoiled α3(IV)α4(IV)α5(IV) collagen IV networks and the more degradable $[\alpha1(IV)]_2\alpha2(IV)$ collagen IV networks. The system was inflated to 20 mmHg hydrostatic pressure, and allowed to remodel for over 250 time steps, which was sufficient for the equilibration of the system.

As Figure 3 confirms, the fluid flow rate through the capillary wall was maintained constant during remodeling, at a value of 38.5 nL/sec - a value which is an

order of magnitude larger than it is physiologically where it is closer to 1 nL/sec for a single glomerulus. In the supercoiled networks case, the pressure decreased slightly to preserve the target flow rate, from 20 mmHg to 18.8 mmHg, a 6% decrease. The Darcy permeability of the GBM increased from 1 nm2 to 1.07 nm^2, a 7% increase. In comparison, with the non-supercoiled networks (plots not shown), the flow rate still remained constant, but the pressure increased from 20 mmHg to 21.2 mmHg, an increase by 6%. The Darcy permeability decreased slightly from 0.62 nm^2 to 0.59 nm^2, a 5% decrease. The permeability of the supercoiled and non-supercoiled networks was different even before the start of remodeling, possibly due to different levels of network compression.

The net amount of material deposited/removed in the two cases also differed. With the supercoiled networks, where supercoils were more protected from removal, there was net addition of material (Figure 4). The opposite happened with the non-supercoiled networks, in which all fibers were subjected to increased degradation -there was net removal of material.

In Figure 5, we see how the stresses and strains change in the capillary, both for the GBM and podocyte layers. With both supercoiled and non-supercoiled networks, stresses on the podocytes were much lower than stresses on the GBM. Once remodeling started, stresses on the supercoiled GBM decreased from 46 kPa to 39 kPa, an 11% decrease. The strain of the capillary also decreased to approximately 6% strain. The thickness of the GBM changed from 0.26 μm to 0.27 μm, a 4% increase. Stresses on the non-supercoiled networks increased from 47 kPa to 54 kPa, a 13% increase. The strain on

the capillary remained very large - approximately 30% strain. The thickness of the GBM decreased even more, from 0.25 μm to 0.24 μm, a 4% decrease. The changes in the capillary can be more easily visualized by looking at the system itself before and after remodeling (Figure 6).

5.5 Discussion

In the current model, we explored a methodology to compare the ability of simplified glomerular capillaries to autoregulate in the presence of the stiffer supercoiled α3(IV)α4(IV)α5(IV) networks versus the more degradable and more distensible $[\alpha1(IV)]_2\alpha2(IV)$ networks. We inflated a section of a capillary to its normal physiological pressure and simulated a remodeling method in which material is added based on the strain on the podocyte cells layer and collagen IV protomers are removed based on their strain (unless protected). At the same time, the system had to maintain constant filtration rate through the capillary wall, even as more material was added to or removed from the GBM and its hydraulic permeability properties changed. The simple model was sufficient to show drastically different progression of remodeling between the two types of networks. With the α3(IV)α4(IV)α5(IV) networks, the system moved towards stability, while with the $[\alpha1(IV)]_2\alpha2(IV)$ networks, the problems of the system (large pressures, stresses, and strains) were worsened.

To see how different parameters adjusted to maintain the constant transcapillary flow rate, we monitored the variables that determine Q throughout remodeling. In the

supercoiled case, P decreased by 6%, thickness increased by 4% and capillary radius decreased by 6%. But the biggest change was observed in the Darcy permeability, k, which increased by 10% even though more material was deposited. That could be accounted for in the relaxation of the network as capillary strains decreased. But it also raises the possibility that the remodeling method of depositing material by increasing collagen IV radius (instead of depositing whole new protomers) is affecting the permeability calculations. Looking back to the permeability calculations described in Chapter 3, the drag coefficient tensor depends on the volume fraction of collagen material, the angle of the protomers, and the length of the protomers; it is then summed for all protomers. The effect of depositing new protomers verses changing their radius on this calculation should be explored in more detail.

Before remodeling was initiated, the systems did not behave very differently. Both with the α3(IV)α4(IV)α5(IV) networks and $[\alpha1(IV)]_2\alpha2(IV)$ networks, the strain on the capillary was very similar - 23% strain verses 24% strain, respectively. This puts into question the idea that the more distensible $[\alpha1(IV)]_2\alpha2(IV)$ network allows larger capillary expansion that negatively affects the podocytes. But as seen in the results from Chapter 3 with single RVE supercoiled networks, the effect of network stiffening due to supercoiling was more pronounced at larger strains. It would be illustrative to inflate the capillaries to larger than normal pressures to see if the responses with the two type of networks change then. Related to this is the observation that the large differences in remodeling with the two types of networks were observed only after the removal rate of the $[\alpha1(IV)]_2\alpha2(IV)$ networks was increased in the model. Initial simulations (data not

shown), in which the removal rates of the two networks were the same, saw remodeling progressing very similarly in the two cases. As such, in our model, the breakdown of the remodeling process with the $[\alpha1(IV)]_2\alpha2(IV)$ networks was only due to difference in degradation rates, not just difference in mechanical properties in the presence of supercoils.

One of the main limitations of the current work presented in this chapter is that the effects of different parameters and conditions were not fully explored. The increase in removal rate for the $[\alpha1(IV)]_2\alpha2(IV)$ networks and the decrease in removal rate for supercoils were not selected based on experimental evidence and the effect of those numbers should be investigated. Some of the constant values used in the addition and removal equations are based on experiments with type I collagen and may not be applicable to type IV collagen. The stiffness of podocytes in relation to the GBM is also an area of interest for which there is very little experimental evidence. Finally, while in Chapter 3 we looked at the effects of different levels of supercoiling, in the current simulations, only one level of supercoiling was tested.

Looking again at the physiological GBM, it is known that the GBM is not a static structure. Even under normal conditions, it is constantly remodeled and replaced, although it is a slow process. In the mature GBM, new material is deposited on the epithelial surface, secreted by podocytes. It takes approximately 1 year for the full GBM to turnover [18]. While the polarity of addition and removal sites may be based on practical considerations (proximity to the cells performing the tasks) our model could be modified to apply the same strategy.

There are still many questions to be answered on the significance of the α3(IV)α4(IV)α5(IV) collagen IV networks for the mechanical, permeability, and remodeling properties of the GBM. It is still unclear why the absence of the α3(IV)α4(IV)α5(IV) networks results in proteinurea as the initial sign of glomerular injury. How does the mechanical environment contribute to the progression of the disease versus interruptions in biochemical signaling pathways? And most importantly, what are the best approaches to reversing or preventing the damage to the glomerular filtration apparatus in Alport syndrome? Further improvements to the model would allow us to better address those questions.

5.6 References

1. Arkill, K. P. et al. 2014 Resolution of the three dimensional structure of components of the glomerular filtration barrier. BMC Nephrol. 15, 24. (doi:10.1186/1471-2369-15-24)

2. Drumond, M. C. & Deen, W. M. 1994 Structural determinants of glomerular hydraulic permeability. Am. J. Physiol. 266, F1–12.

3. Kriz, W., Kretzler, M., Provoost, a P. & Shirato, I. 1996 Stability and leakiness: opposing challenges to the glomerulus. Kidney Int. 49, 1570–4.

4. Barocas, V. H., Dorfman, K. D. & Segal, Y. 2012 A Model of Strain-Dependent Glomerular Basement Membrane Maintenance and its Potential Ramifications in Health and Disease. J. Biomech. Eng. 134, 081006 1–8. (doi:10.1115/1.4007098)

5. Carlstrom, M., Wilcox, C. S. & Arendshorst, W. J. 2015 Renal Autoregulation in Health and Disease. Physiol. Rev. 95, 405–511. (doi:10.1152/physrev.00042.2012)

6. Cooper, M. E. 2001 Interaction of metabolic and haemodynamic factors in mediating experimental diabetic nephropathy. Diabetologia 44, 1957–72. (doi:10.1007/s001250100000)

7. Zatz, R., Meyer, T., Renke, H. G. & Brenner, B. M. 1985 Predominance of hemodynamic rather than metabolic factors in the pathogenesis of diabetic glomerulopathy. Proc. Natl. Acad. Sci. U. S. A. 82, 5963–5967.

8. Meehan, D. T., Delimont, D., Cheung, L., Zallocchi, M., Sansom, S. C., Holzclaw, J. D., Rao, V. & Cosgrove, D. 2009 Biomechanical strain causes maladaptive gene regulation, contributing to Alport glomerular disease. Kidney Int. 76, 968–76. (doi:10.1038/ki.2009.324)

9. Kashtan, C. E. 1999 Alport syndrome: an inherited disorder of renal, ocular, and cochlear basement membranes. Medicine (Baltimore). 78, 338.

10. Langeveld, J. P., Wieslander, J., Timoneda, J., McKinney, P., Butkowski, R. J., Wisdom, B. J. & Hudson, B. G. 1988 Structural heterogeneity of the noncollagenous domain of basement membrane collagen. J. Biol. Chem. 263, 10481–8.

11. Kalluri, R., Shield, C. F., Todd, P., Hudson, B. G. & Neilson, E. G. 1997 Isoform switching of type IV collagen is developmentally arrested in X-linked Alport syndrome leading to increased susceptibility of renal basement membranes to endoproteolysis. J. Clin. Invest. 99, 2470–8. (doi:10.1172/JCI119431)

12. Gunwar, S., Ballester, F., Noelken, M. E., Sado, Y., Ninomiya, Y. & Hudson, B. G. 1998 Glomerular Basement Membrane. Identification of a novel disulfide- cross-linked netowrk of alpha3, alpha4, and alpha5 chains of type IV collagen and its implications for the pathogenesis of Alport syndrome. J. Biol. Chem. 273, 8767–8775.

13. Hudson, B. G., Reeders, S. T. & Tryggvason, K. 1993 Type IV collagen: structure, gene organization, and role in human diseases. J. Biol. Chem. 268, 26033–26036.

14. Hadi, M. F. & Barocas, V. H. 2013 Microscale fiber network alignment affects macroscale failure behavior in simulated collagen tissue analogs. J. Biomech. Eng. 135, 021026 1–8. (doi:10.1115/1.4023411)

15. Hadi, M. F., Sander, E. A., Ruberti, J. W. & Barocas, V. H. 2012 Simulated remodeling of loaded collagen networks via strain-dependent enzymatic degradation and constant-rate fiber growth. Mech. Mater. 44, 72–82. (doi:10.1016/j.biotechadv.2011.08.021.Secreted)

16. Chandran, P. L. & Barocas, V. H. 2007 Deterministic material-based averaging theory model of collagen gel micromechanics. J. Biomech. Eng. 129, 137–47. (doi:10.1115/1.2472369)

17. Stylianopoulos, T. & Barocas, V. H. 2007 Multiscale, structure-based modeling for the elastic mechanical behavior of arterial walls. J. Biomech. Eng. 129, 611–8. (doi:10.1115/1.2746387)

18. Walker, F. 1972 The Deposition of Silver in Glomerular Basement Membrane. Virchows Arch. Abt. 11, 90–96.

5.7 Figures

Figure 5.1. Structure of the glomerular filtration barrier. (a) Primary blood filtration happens in the part of kidneys called glomerulus. Unfiltered blood enters the glomerulus through the afferent arteriole, passes through a network of capillaries through the walls of which water and small molecules are filtered into urinary space, and the remaining blood exits the glomerulus through the efferent arteriole. **(b)** The walls of the glomerular capillaries are a 3-layered filter: starting from inside the capillary lumen, filtrate must pass through the pores of endothelial cells, the glomerular basement membrane, and channels in the epithelial cell layer.

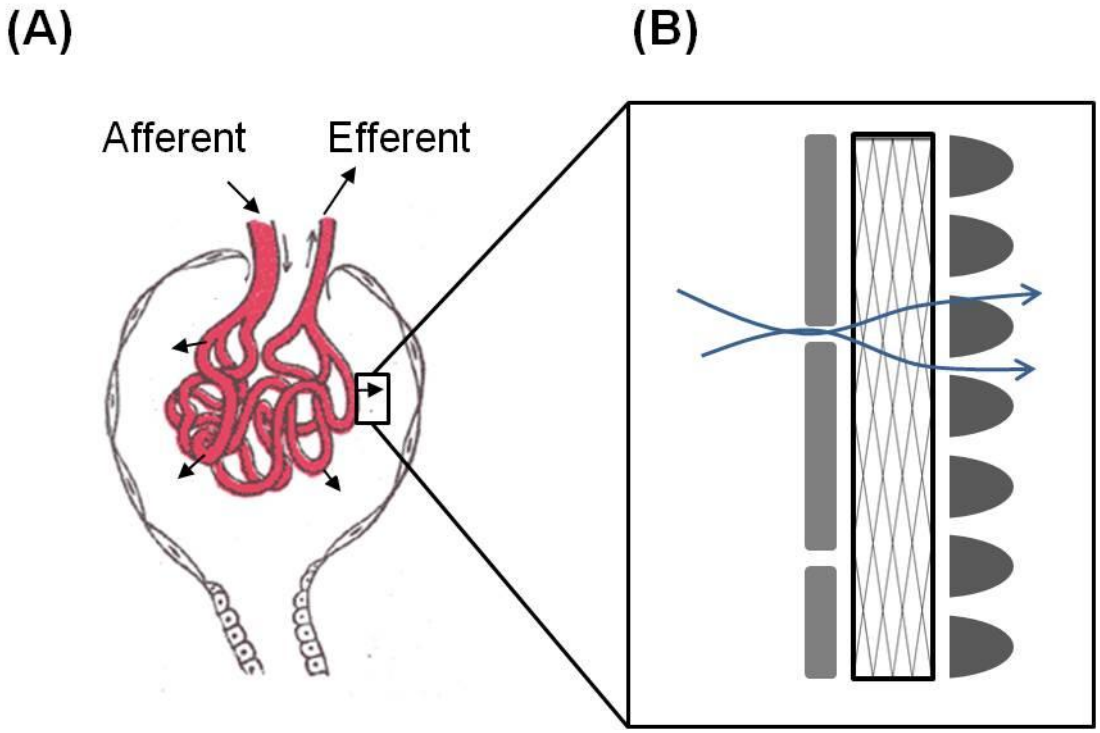

Figure 5.2. Capillary geometry. The capillary was modeled as a two layered quarter section of a short cylinder; the inner layer represents the glomerular basement membrane (GBM) and the outer layer represent the podocytes. Initially, the capillary has a radius of 4 µm and thickness of 600 nm. Different representative networks were used in each layer but all networks were aligned to match the orientation of the finite elements. Pressure was applied to the elements of the inner layer to inflate the capillary before remodeling was initiated.

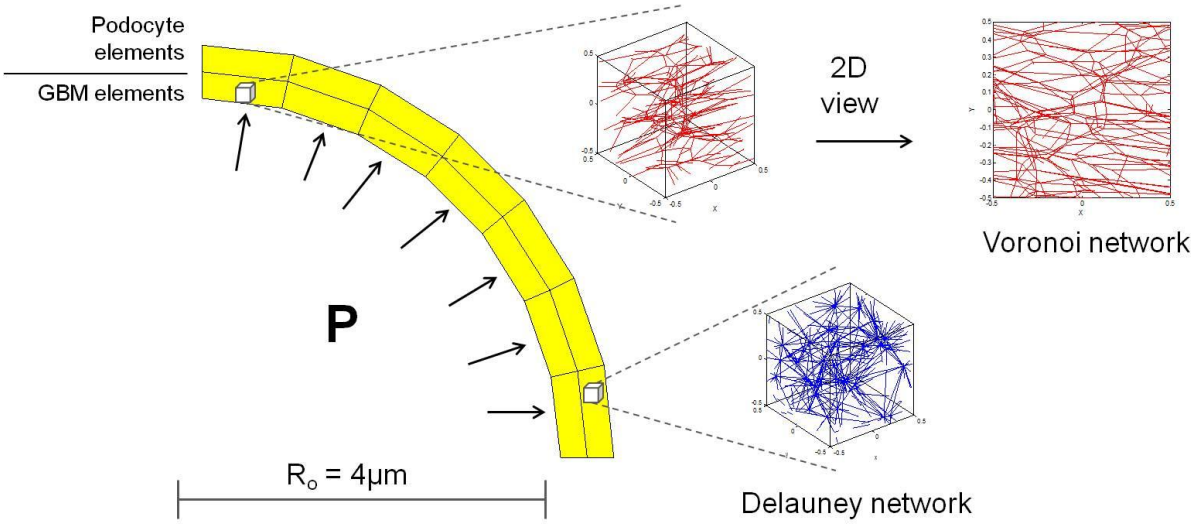

Figure 5.3. Constant fluid flow rate through the capillary wall was maintained throughout the remodeling time steps. These results are with the supercoiled α3(IV)α4(IV)α5(IV) network but the same is also true for the $[\alpha1(IV)]_2\alpha2(IV)$ networks. In contrast to the constant fluid flow rate, the pressure gradually lowered and Darcy permeability of the GBM increased.

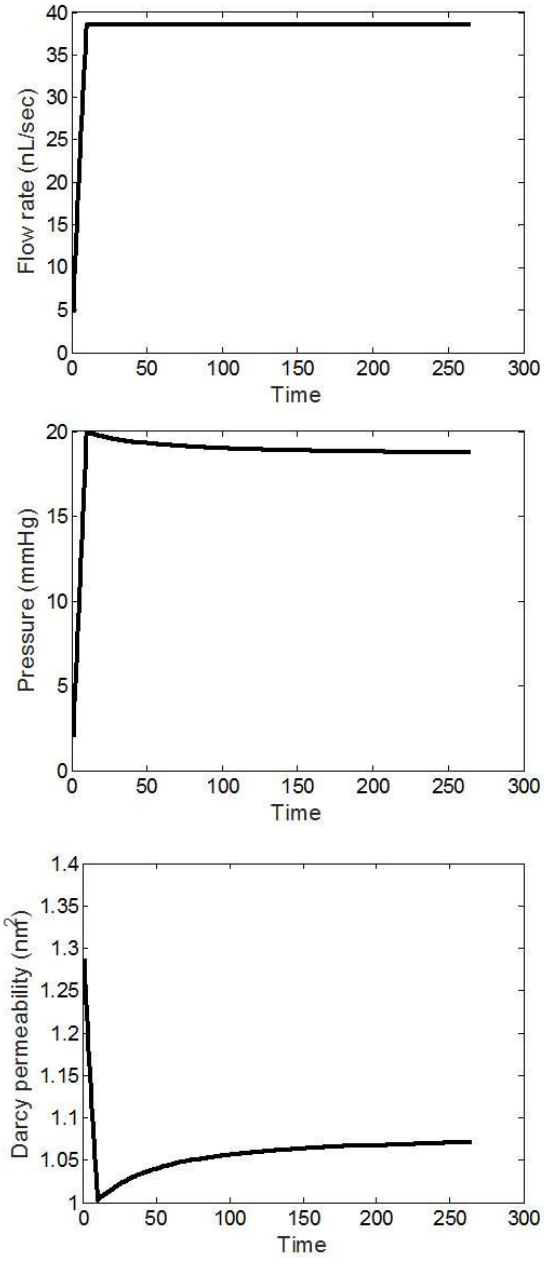

Figure 5.4. Changes to average collagen IV radius due to remodeling. (a) With supercoiled networks, there is net addition of material. **(b)** With non-supercoiled networks, there is net removal of material.

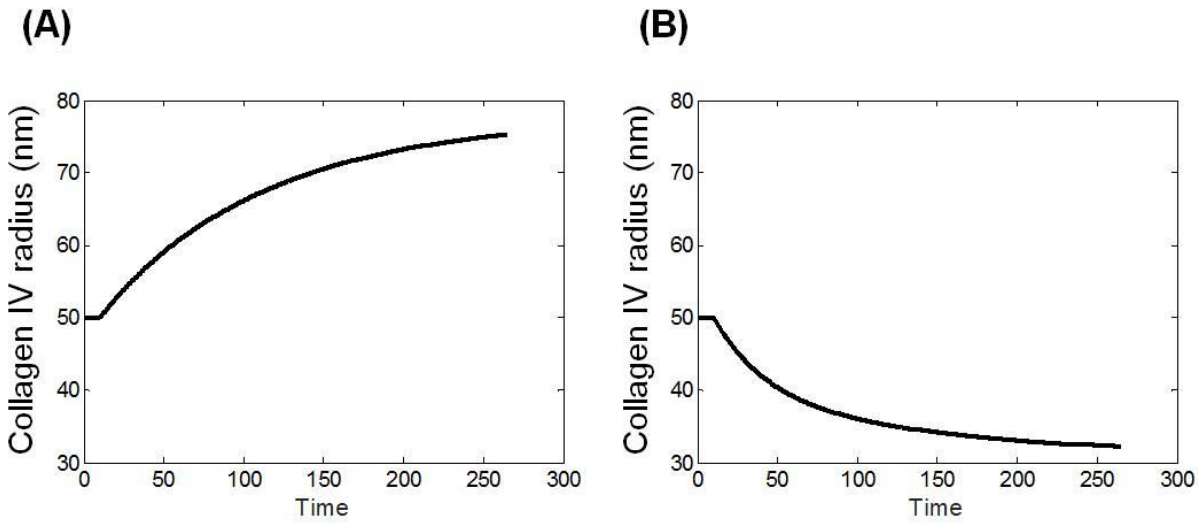

Figure 5.5. Changes in stress, strain, and thickness of GBM and podocytes during remodeling. (a) When the GBM contains the supercoiled networks, stresses are reduced, the capillary diameter decreases, and the thickness of the system increases. **(b)** When the GBM contains the non-supercoiled networks, stresses increase, the capillary expands further, and the capillary wall becomes thinner.

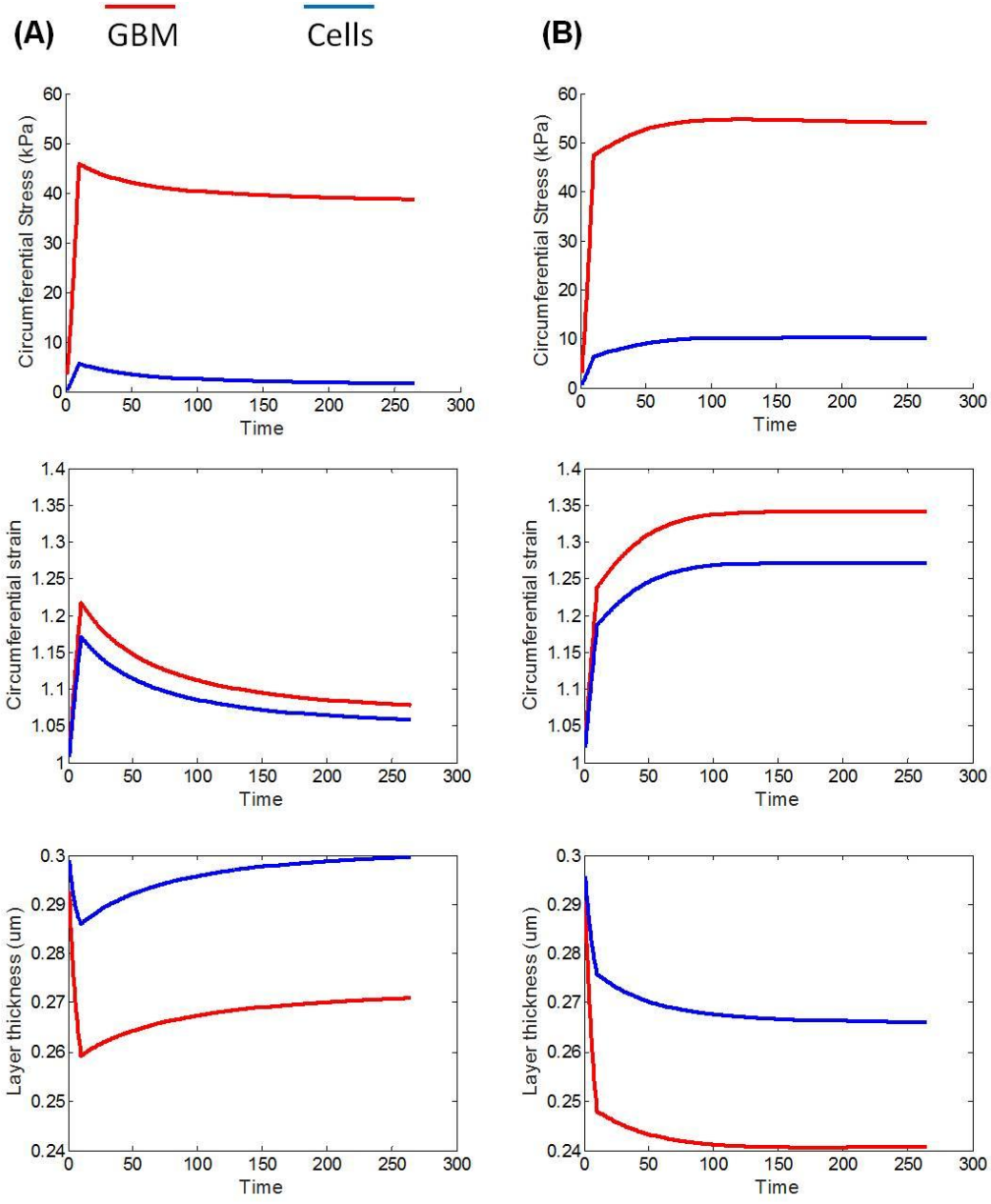

Figure 5.6. Visualizing changes in capillaries dues to remodeling. (a) With the supercoiled networks, stresses in capillary are reduced and strains are lowered. **(b)** With the non-supercoiled networks, the capillary remains highly strained and stresses become even higher.

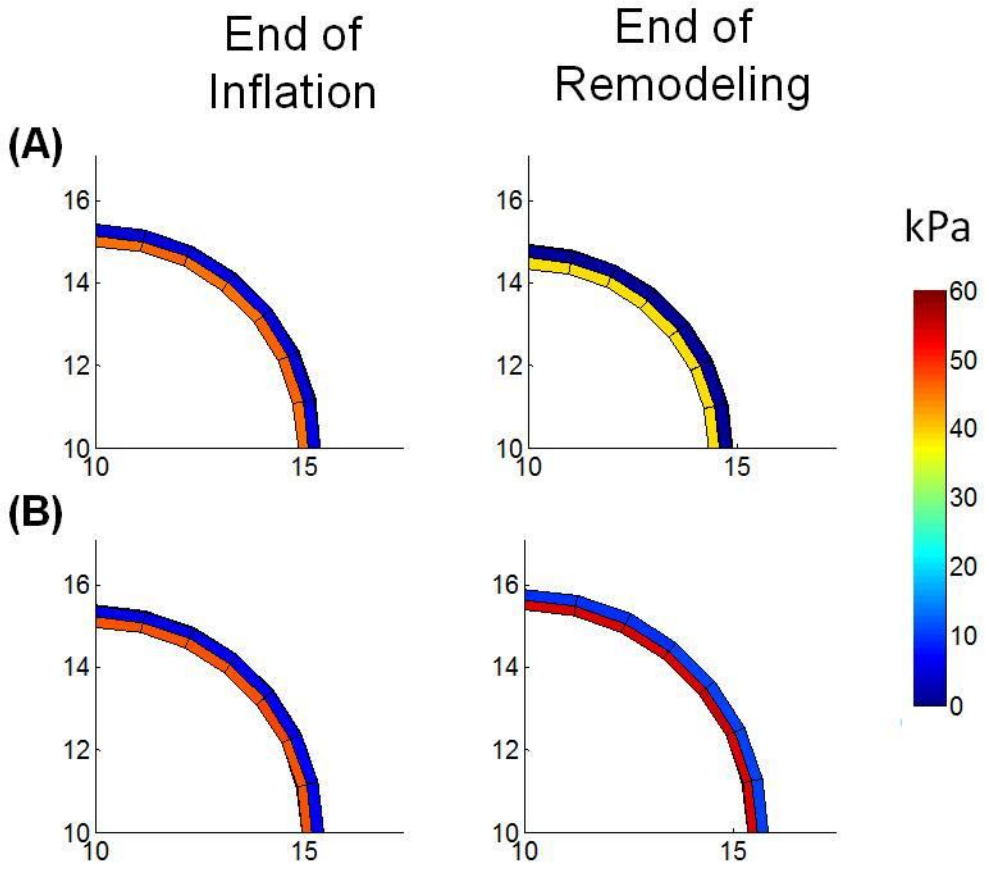

Chapter 6: Conclusions and Future Work

6.1 Conclusions

The glomerular basement membrane (GBM) is a vital part of the blood-urine filtration barrier in the kidneys. In healthy GBMs, the main tension-resisting component is type IV collagen of the α3(IV), α4(IV), and α5(IV) isoforms, called the minor chains. In some diseases, the proper production or assembly of the minor chains is interrupted, and they are replaced by other collagen IV isoforms, called the major chains. As a result, the GBM becomes leaky and disorganized, ultimately causing kidney failure in patients, a consequence that suggests an important role for the minor chains in maintaining the mechanical and permeability properties of the GBM. Understanding the biomechanical aspects of the minor chains and how their absence could be responsible for (1) the initial injury to the GBM and (2) the progression to kidney failure, would provide valuable insights into possible treatment options and strategies.

A combination of experiments and computational models was designed to test the contribution of the minor chains to the mechanical properties of the GBM. A model basement membrane, the lens basement membrane (LBM) was used in experiments to compare the distensibility of tissues with the minor chains and with the major chains. The experiments showed basement membranes containing only major chains were much more distensible, quantifying clear differences in mechanical properties between the major and minor chains. The results from the LBM offer insight into the mechanical changes of the GBM, which is much harder to test experimentally.

It has been postulated in the literature that the higher level of lateral cross-linking (supercoiling) in the minor chain network contributes additional strength/stability to basement membranes. To investigate the effects of supercoiling on the mechanical and permeability properties of collagen IV networks, model networks were generated and reconnected to create different levels of supercoiling. Supercoiling greatly increases the stiffness of collagen IV networks but only minimally decreases the permeability. This suggests that the formation of supercoils is a specialized mechanism to provide a network stiff and strong enough to withstand the high hydrostatic pressures of filtration, yet porous enough that filtration is not hindered, which is a requirement in the GBM. The major chain collagen IV networks would not be able to replicate the contribution of the minor chain collagen IV networks, resulting in injury to the GBM and stretching of the cellular layers attached to it.

As the cells sense changes in their mechanical environment, they can respond by remodeling the GBM. Before investigating remodeling in the complicated environment of the GBM, it was important to compose an effective model of matrix remodeling by strain-sensitive cells. A theoretical model was developed of a cell in parallel with a network to study what factors of the remodeling process help the cell move toward mechanical stability. The study showed cells are able to respond to mechanical changes but there was a delicate balance between deposition and removal rates that could force the system out of control.

Applying the methods of the cell-network model to the podocyte-GBM system in the glomerular capillaries, it was possible to investigate how the supercoiled minor chain

networks provide protection during remodeling. The degradation rates of major and minor chain networks had greater impact on remodeling remodeling of the GBM than the differences in stiffness between the two types of collagen IV networks.

In conclusion, the modeling and experimental work presented here suggests that the minor chain collagen IV networks protect the GBM and podocytes from initial injury. Also, the higher resistivity of the minor chain networks to degradation is needed to prevent the system from entering a dangerous cycle due to autoregulation and remodeling.

6.2 Future work

There are certainly many aspects of this work that could be improved or expanded upon, but I will focus on some of the more significant points. Some of the models presented here have not been validated by experimental data, only through supporting (but not directly equivalent) observations. Limitations on experimental methods for mechanical testing of the small GBM were the cause of this omission. One possibility for improvement is the use a micropipette aspiration system designed for testing of microscopic samples. Such a system already exists in use in the lab, but it requires modifications for use with GBM samples.

Another part of the project that could be expanded is the model of remodeling in the GBM. The current model assumed that changes to the system occur globally, when in reality, injury to the GBM and podocytes usually occur locally and are repaired through

local controls. One way to address this is by perturbing only few elements in the system. Some examples are: (1) removing the cell layer over a single GBM element (podocyte detachment); (2) increasing the permeability of a single GBM element (acute injury to the GBM); (3) decreasing the permeability of a single GBM element (deposition of fibrotic tissue and scaring seen in later stages of Alport syndrome); and (4) making some GBM elements thinner and other thicker (also seen in later stages of Alport syndrome where the GBM thickness is very irregular). The above examples would allow us to explore not only the contribution of the minor chain networks, but the importance of different components in the glomerular filtration barrier. In addition, there is significant clinical evidence that reducing blood pressure in Alport syndrome patients is helpful in delaying the progression of the disease. The model could be modified to investigate how remodeling with the major chain networks at lowered pressures proceeds differently.